Photoionization dynamics of excited Ne, Ar, Kr and Xe atoms near threshold

Review Article

Author(s):
Sukhorukov, Victor L.; Petrov, I.D.; Schäfer, Martin; Merkt, Frédéric; Ruf, Matthias W.; Hotop, Hartmut

Publication date:
2012-05-14

Permanent link:
https://doi.org/10.3929/ethz-a-010780822

Originally published in:
Journal of Physics B: Atomic, Molecular and Optical Physics 45(9), https://doi.org/10.1088/0953-4075/45/9/092001

Funding acknowledgement:
135342 - Rydberg states, VUV laser spectroscopy and photoionization dynamics (SNF)

The following article appeared in *J. Phys. B: At. Mol. Opt. Phys.* **45**, 092001 (2012) and may be found at http://dx.doi.org/10.1088/0953-4075/45/9/092001.

TOPICAL REVIEW: Photoionization dynamics of excited Ne, Ar, Kr, and Xe atoms near threshold

V L Sukhorukov[1,2], I D Petrov[1,2], M Schäfer[3], F Merkt[3], M-W Ruf[2], H Hotop[2]

[1] Rostov State Transport University, 344038 Rostov-on-Don, Russia

[2] Department of Physics, University of Kaiserslautern, D-67653 Kaiserslautern, Germany

[3] ETH Zürich, Laboratorium für Physikalische Chemie, CH-8093 Zürich, Switzerland

E-mail: hotop@rhrk.uni-kl.de

Abstract. A review of experimental and theoretical studies of the threshold photoionization of the heavier rare-gas atoms is presented, with particular emphasis on the autoionization resonances in the spectral region between the lowest two ionization thresholds (mp^5 ^{2}P$_{3/2}$ and mp^5 ^{2}P$_{1/2}$, with m = 2, 3, 4, and 5 for Ne, Ar, Kr, and Xe, respectively). Observed trends in the positions, widths, and shapes of the autoionization resonances in dependence of the atomic number, the principal quantum number n, the orbital angular momentum quantum number ℓ and further quantum numbers such as K, J and F specifying the fine- and hyperfine-structure levels, are summarized and discussed in the light of ab initio and multichannel quantum defect theory calculations. The dependence of the photoionization spectra on the initially prepared neutral state, e.g. the ^{1}S$_0$ ground state, the mp^5 $(m+1)$s ^{3}P$_2$ and mp^5 $(m+1)$s$'$ ^{3}P$_0$ metastable levels and other states prepared from the ground or metastable levels in single- and multiphoton processes, are also discussed, including results on the photoionization of aligned and oriented samples and on photoelectron angular distributions. The effects of various approximations in the theoretical treatment of photoionization in these systems are analysed. The very large and at first sight discouraging diversity of observed phenomena and the numerous anomalies in spectral structures associated with the threshold ionization of the rare-gas atoms can be described in terms of a limited set of interactions and dynamical processes. Examples are provided illustrating characteristic aspects of the photoionization, and sets of recommended parameters describing the energy-level structure and photoionization dynamics of the rare-gas atoms are presented which were extracted in a critical analysis of the very large body of experimental and theoretical data available on these systems in the literature.

(Version of 6 November 2011)

1. Introduction

Studies of the Rydberg states of the rare-gas atoms have played an essential role in the development of photoabsorption spectroscopy and in the understanding of the process of photoionization [1, 2]. The spectra of the bound and autoionizing Rydberg states (ARS) of the heavier rare-gas atoms Rg = Ne, Ar, Kr, and Xe are known today with an exceptional degree of detail. They have served for many decades, and still serve today, as ideal systems with which to test theories of photoionization and to characterize the properties of new light sources (e.g., bandwidth, coherence, polarization) and spectroscopic methods (sensitivity, accuracy). The body of knowledge on the Rydberg states and in particular on the ARS of the rare-gas atoms available in the literature is enormous, but fragmented and not free of inconsistencies so that the search for specific data can be time-consuming. In view of all the comprehensive experimental and theoretical work dedicated to the characterization of the autoionization spectra of Rg = Ne–Xe over the last 30 years, we consider it timely to provide a survey on these achievements and to present a set of recommended values for the data required to describe the photoionization dynamics of these systems.

In an important early paper, Beutler [3] detected sharp asymmetric peaks in the photoabsorption cross sections of Rg = Ar, Kr, and Xe at energies between the two lowest ionization thresholds corresponding to the spin–orbit split ground state $m\mathrm{p}^5\ {}^2\mathrm{P}_{J^+}$ ($J^+ = 3/2, 1/2$; $m = 3 - 5$) of the singly-charged ions. These features were attributed to autoionizing Rydberg states (ARS) of the type $\mathrm{Rg}\,(m\mathrm{p}^5({}^2\mathrm{P}_{1/2})\,n\ell')$, which are bound with respect to the $^2\mathrm{P}_{1/2}$ threshold, but—mediated by the Coulomb interaction among the involved electrons—decay to the $^2\mathrm{P}_{3/2} + \mathrm{e}^-$ continuum. Within a few months, Fano [4] provided a theoretical interpretation of the asymmetric resonance lineshapes in terms of interference between the direct ionization process (DI)

$$\mathrm{Rg}\,(m\mathrm{p}^6\ {}^1\mathrm{S}_0) + \gamma \xrightarrow{\mathrm{DI}} \mathrm{Rg}^+({}^2\mathrm{P}_{3/2}) + \mathrm{e}^- \tag{1}$$

and the indirect process (excitation E + autoionization AI)

$$\mathrm{Rg}\,(m\mathrm{p}^6\ {}^1\mathrm{S}_0) + \gamma \xrightarrow{\mathrm{E}} \mathrm{Rg}\,(m\mathrm{p}^5({}^2\mathrm{P}_{1/2})\,n\ell'[K']_{J=1}) \xrightarrow{\mathrm{AI}} \mathrm{Rg}^+({}^2\mathrm{P}_{3/2}) + \mathrm{e}^-. \tag{2}$$

Here the ARS are described in Racah coupling [5], where $\vec{\ell}$ denotes the orbital angular momentum of the Rydberg electron; the quantum number K results from coupling the total angular momentum $\vec{J}^+$ of the ionic core with $\vec{\ell}$ ($\vec{K} = \vec{J}^+ + \vec{\ell}$) and the total

angular momentum $\vec{J}$ is obtained by coupling the spin $\vec{s}$ of the Rydberg electron to $\vec{K}$ ($\vec{J} = \vec{K} + \vec{s}$). The prime denotes Rydberg states for which $J^+ = 1/2$ while bound Rydberg levels with $J^+ = 3/2$ are denoted by $m\mathrm{p}^5(^2\mathrm{P}_{3/2})\, n\ell[K]_J$. In the following text, the ARS will be denoted $n\ell'[K']_J$.

About 50 years ago, new interest arose in atomic photoionization and ARS when widely tunable light sources became available at synchrotron radiation facilities. In 1961, Fano [6] refined his earlier ideas on atomic autoionization and presented his well-known formula describing the excitation cross section for an isolated resonance embedded in a continuum of interacting levels. When a cross section σ_b for excitation to noninteracting continuum states is included, the formula is written as [7]

$$\sigma(\epsilon) = \sigma_\mathrm{a}\frac{(q+\epsilon)^2}{1+\epsilon^2} + \sigma_\mathrm{b}. \tag{3}$$

In equation (3), ϵ is a reduced energy variable $\epsilon = 2(E - E_0)/\Gamma$ (E_0: resonance energy; Γ: resonance width), q denotes the shape parameter or profile index, and σ_a represents a cross section for the excitation to interacting continua. The shape parameter q determines the lineshape (or profile) of the resonance and may take values between $-\infty$ and $+\infty$. For large $|q|$ values ($\gtrsim 30$), the profile is nearly Lorentzian and the cross section close to the resonance exceeds that of the surrounding continuum. For $q = 0$, the cross section at the position of the resonance reaches a minimum and one speaks of a Lorentzian-type window resonance. For $q = \pm 1$, symmetric dispersion profiles are obtained. All other q values result in asymmetric lineshapes with the minimum (maximum) occuring at $E < E_0$ ($E > E_0$) for $q > 0$ and at $E > E_0$ ($E < E_0$) for $q < 0$. As an alternative to equation (3), Shore profiles [8, 9]

$$\sigma(\epsilon) = \frac{a\epsilon + b}{1+\epsilon^2} + C(\epsilon) \tag{4}$$

are also used to describe autoionization line shapes; here $C(\epsilon)$ denotes a slowly-varying background (see also section 3.3.2 and equation (43)). Equations (3) and (4) are equivalent, but (4) is mathematically simpler, as noted in [10], since it represents a Lorentzian profile for $a = 0$ whereas (3) attains a Lorentzian form only in the limit $|q| \to \infty$, $\sigma_\mathrm{a} \to 0$.

Improvements in (synchrotron) radiation sources and monochromator technology in the 1960s and later allowed great progress in photoabsorption and photoionization spectroscopy [1]. The work of Madden and Codling [11–13] revealed sharp resonances in the rare-gas atoms originating from doubly excited states, e.g., He ($n\ell n'\ell'$; $n, n' \geq 2$) [13]. Much better resolved ARS lineshape data for the rare gases Ar, Kr, and Xe [1, 14, 15] were obtained and later complemented by coherent VUV excitation spectra [16–22].

The development of excimer lasers containing rare-gas atoms [23] further stimulated experimental and theoretical work to characterize in detail the photoionization process involving rare-gas atoms, in particular from excited levels.

In the 1970s, tunable lasers in conjunction with frequency-doubling techniques became available and enabled studies of even-parity ARS of the heavier rare-gas atoms, exploiting single-photon excitation of metastable rare-gas levels Rg $(m\mathrm{p}^5(m{+}1)\mathrm{s}$, $J = 2, 0)$ [24–26] (for more recent work, see [27–34]). Starting in the early 1980s, resonant two-photon excitation experiments of the metastable rare-gas atoms yielded spectra of the odd-parity ARS of Ne, Ar, Kr, and Xe for $J = 0 - 4$ [35–50]. With single-mode lasers, the very sharp $n\mathrm{s}'$ and $n\mathrm{d}'$ resonances in neon could be resolved for the first time [37, 38, 42]. Nonresonant three- and four-photon excitation from the ground state were also used to access $n\ell'[K']_J$ ARS of odd ($\ell' = 0, 2, 4$; $J = 0, 2, 4$) [51–53] and even parity ($\ell' = 1, 3$; $J = 1, 3$) [54, 55].

From the 1990s on, time-synchronized resonant two-step photoexcitation from the ground state enabled studies of even-parity ARS ($\ell' = 1, 3$) of the heavier rare-gas atoms. In these experiments, highly monochromatized synchrotron radiation [34, 56–61] or laser-produced coherent VUV radiation [62–64] was used to access low- or higher-lying odd-parity intermediate levels with $J = 1$, and narrow-band pulsed tunable lasers were employed to record spectra of the ARS.

On the theory side, the calculations of Johnson and coworkers within the framework of the random-phase approximation with exchange yielded detailed information on the $n\mathrm{s}'$, $n\mathrm{d}'$ $J = 1$ ARS in Ne [65] and Ar, Kr, and Xe [66] (see also [40, 67, 68]). In the mid 1990s, an effort was started to provide a detailed characterization of the near-threshold photoionization dynamics of *excited* rare-gas atoms, using the configuration-interaction Pauli–Fock method (CIPF) [69–71], subsequently improved by including core polarization (CIPFCP) [72]. *Absolute* total and partial photoionization cross sections were computed for a broad variety of excited states with emphasis on the lineshapes of the ARS [33, 34, 62, 64, 73–75]. Systematic trends for the resonance widths of the $n\ell'$ ARS with $\ell' = 0 - 5$ were elucidated [76, 77].

Recently, laser cooling and trapping of metastable rare-gas atoms in magneto-optical traps (MOT) [78–81] and the achievement of Bose–Einstein condensation (BEC) in spin-polarized He $(2\,^3\mathrm{S})$ gas [82, 83] has led to renewed interest in collisions of excited rare-gas atoms with photons [84], electrons [85], atoms [86–89], and molecules [90]. MOT experiments enabled precise measurement of the lifetimes of the metastable levels of Ne, Ar, Kr, and Xe [79, 80, 91–93]. Although the natural lifetime of the

metastable $m\mathrm{p}^5(m+1)\mathrm{s}$, $J=2$ levels ($\gtrsim$15 s) is sufficiently long, it now appears to be a settled issue [87,94] that BEC in spin-polarized samples of these species cannot be achieved because—in contrast to the He ($2\,^3\mathrm{S}$) case—ionization processes between the spin-polarized atoms (although suppressed) occur at too high rates.

The review is organized as follows: In Section 2, experimental methods for the study of ARS of the rare-gas atoms including data analysis are summarized. In Section 3, we discuss theoretical approaches to describe near-threshold photoionization, namely, multichannel quantum defect theory (MQDT) and *ab initio* calculations. In Section 4, we present experimental and theoretical results on the (reduced) widths of the ARS in the rare-gas atoms Ne–Xe and discuss general trends. The energy-dependent photoionization cross sections near threshold are treated in Section 5 with emphasis on the lineshapes of the ARS, as accessed from different intermediate levels. The review ends in Section 6 with a summary and a brief outlook.

2. Experimental methods

2.1. Strategies for accessing autoionizing Rydberg states

The ionization energy $E(^2\mathrm{P}_{3/2})$ of ground state rare-gas atoms $\mathrm{Rg}(m\mathrm{p}^6)$ to the lowest ion level $m\mathrm{p}^5\ ^2\mathrm{P}_{3/2}$ ranges from 12.13 eV (Xe) to 21.56 eV (Ne) (see table 1) and the lowest excited level $m\mathrm{p}^5(m{+}1)\mathrm{s}$ $J=2$ is located between 8.31 eV (Xe) and 16.62 eV (Ne) above the respective ground state (see table 2). Correspondingly, single-photon access of odd-parity ($n\mathrm{s}', n\mathrm{d}'$ $J=1$) ARS from ground-state Ne–Xe atoms requires vacuum-ultraviolet (VUV) light (wavelength $\lambda < 200$ nm)—light which is strongly absorbed by the oxygen and nitrogen in the air. In contrast, light in the UV and visible ranges ($\lambda > 200$ nm) suffices to access both even-parity ($n\mathrm{p}', n\mathrm{f}'$) ARS and odd-parity ($n\mathrm{s}', n\mathrm{d}', n\mathrm{g}'$) ARS by one-photon or by resonant two-color two-photon excitation from levels of the first excited $m\mathrm{p}^5(m+1)\mathrm{s}$ or higher-lying configurations.

Two strategies, illustrated in figure 1, have proven particularly useful for studies of the even-parity ($n\mathrm{p}', n\mathrm{f}'$) ARS: (a) Single-photon excitation from the $J=2,0$ levels of the metastable $m\mathrm{p}^5(m+1)\mathrm{s}$ configuration (for their lifetimes, see table 2), allowing access to the $n\mathrm{p}'[1/2,3/2]_1$, $n\mathrm{p}'[3/2]_2$ ARS and—via electron correlation effects—to the $n\mathrm{f}'[5/2]_{2,3}$ ARS. (b) Resonant two-step photoexcitation from the ground state via odd-parity intermediate levels $m\mathrm{p}^5(m+k)\mathrm{s}$ $J=1$ ($k\geq 1$) or $m\mathrm{p}^5(m+k)\mathrm{d}$ $J=1$ ($k\geq 1$ for Ne, $k\geq 0$ for Ar, Kr, Xe), using monochromatized synchrotron radiation or narrowband coherent VUV radiation for the first step. In this way the four $n\mathrm{p}'$ ARS ($[1/2]_{0,1}$, $[3/2]_{1,2}$)

and the $n\mathrm{f}'[5/2]_2$ ARS can be reached.

In addition to numerous studies of the $n\mathrm{s}'[1/2]_1$ and $n\mathrm{d}'[3/2]_1$ series from the ground state, many investigations of the odd-parity $n\mathrm{s}', n\mathrm{d}', n\mathrm{g}'$ resonances have been carried out by two-step laser excitation from both metastable levels via $J = 1, 2, 3$ levels of the $m\mathrm{p}^5(m+1)\mathrm{p}$ configuration, as illustrated in figure 2. In this way, ARS with $J = 0 - 4$ can be accessed, including the $n\mathrm{g}'[7/2]_{3,4}$ ARS the observation of which is mediated by electron correlation effects.

Details of excitation strategies are discussed with reference to propensity rules for electric-dipole transition matrix elements on the basis of the relevant atomic energy levels, shown in figure 3 for the case of Ne. Here, the ten levels of the $2\mathrm{p}^5 3\mathrm{p}$ configuration (which are labelled $2\mathrm{p}_x$ ($x = 1 - 10$ with decreasing energy) in Paschen notation) are denoted by their usual quantum numbers in Racah coupling, i.e., $3\mathrm{p}[K]_J$ for levels with predominant $J^+ = 3/2$ core and $3\mathrm{p}'[K']_J$ for levels with predominantly $J^+ = 1/2$ core.

2.1.1. Single-photon excitation from the ground state. Early studies of Rydberg states of Ne–Xe by photoabsorption and photoionization spectroscopy used gas discharge lamps (in particular the helium continuum $\lambda = 58$–110 nm) as sources of VUV radiation [1, 95, 96]. With the development of the synchrotron, a broadly tunable and intense source of VUV radiation became available [1, 97–99]. For both types of sources, the resolution is limited by the monochromators used to disperse the radiation; a resolving power $\nu/\Delta\nu \approx 2 \cdot 10^5$ can be obtained for grating instruments [97, 99, 100] and up to 10^6 for Fourier-transform spectrometers [101–104]. A still higher spectral resolution can be obtained with coherent VUV radiation generated using pulsed lasers and nonlinear optical techniques.

Tunable narrow-band VUV laser radiation is conveniently generated by nonlinear optical frequency conversion of visible or ultraviolet radiation in gases [105–108]. Because there are no transparent media for light with wavelength $\lambda < 105$ nm (lithium fluoride (LiF) cut-off), the frequency conversion (nonresonant frequency tripling or sum-frequency mixing) has to occur in a free gas jet [109, 110]. VUV radiation up to 20 eV [111] is produced efficiently by resonant four-wave mixing in a rare gas: $\nu_{\mathrm{VUV}} = 2\nu_1 \pm \nu_2$, where $2\nu_1$ corresponds to a two-photon transition of the rare gas. Examples of two-photon resonances with which high VUV intensities can be reached and the wavenumber ranges of the VUV radiation that can be produced with these transitions are summarized in table 3. The generated VUV radiation is separated from the fundamental laser radiation (ν_1 and ν_2) by using a toroidal dispersion grating,

which can be used to collimate the diverging VUV radiation or even focus it into the photoexcitation region [112]. Using pulsed dye lasers with intracavity étalon, VUV radiation with a spectral bandwidth of 0.1 cm^{-1} (12 μeV) and maximal intensities of about $10^9 - 10^{10}$ photons/pulse after the monochromator can be produced, sufficient to resolve adjacent Rydberg states up to $n \approx 120$ [112, 113].

Replacing the pulsed dye lasers by continuous-wave (cw) single-mode ring dye lasers, which have spectral bandwidths of less than 1 MHz, and amplifying the laser radiation in dye cells pumped by an injection-seeded Nd:YAG laser, Fourier-transform-limited VUV radiation with a spectral bandwidth of 250 MHz or 0.008 cm^{-1} can be obtained, with which Rydberg series can be resolved up to $n \approx 200$ [20, 114–118]. A smaller bandwidth requires longer pulses, which can be generated by using Ti^{3+}-doped sapphire (Ti:Sa) crystals instead of dye cells. The much longer lifetime of the population inversion in the crystal compared to the dye solution permits the generation of longer laser pulses, but the amplification factor is by many orders of magnitude smaller. Therefore, many more amplification steps are required; this can be achieved by guiding the laser beam to be amplified many times through the Ti:Sa crystals [119]. A solid-state VUV laser system with a 55 MHz (0.0018 cm^{-1}) bandwidth delivering about 10^8 photons/pulse (at a repetition rate of 25 Hz) is described in Refs. [120, 121] and has been used to study the hyperfine structure of autoionizing Rydberg series of krypton [22]. The bandwidth of this laser system enables the resolution of adjacent members of a series up to $n > 300$.

When carrying out spectroscopic measurements with narrow-bandwidth VUV lasers, the resolution is limited by the Doppler broadening caused by residual velocity components in the transverse direction of the skimmed supersonic beam [121]. Because the Doppler broadening is proportional to the frequency of the radiation, a higher resolution can be attained by using a multiphoton excitation scheme where the rare-gas atoms are first excited by VUV radiation to high Rydberg states and then probed by narrow-bandwidth low-frequency radiation [113, 122–124].

2.1.2. Multiphoton-excitation schemes. While one-photon VUV excitation of ground-state rare gases allows to excite only odd-parity Rydberg states with $J = 1$ ($\ell^{(\prime)} = 0, 2$), a broader variety of ARS can be accessed from the ground state by nonresonant two-, three-, or four-photon excitation with a single tunable laser [51–55, 125]. More selective excitation of ARS is achieved by resonant excitation schemes via low-lying intermediate Rydberg states, using narrow-band synchrotron radiation [56, 60, 126] or coherent VUV light [62] or a two-photon transition [127] to reach the intermediate level.

In such two-step schemes, final states with different total angular momentum quantum numbers J may be addressed with variable probability, depending on the relative polarization direction of the different radiation fields (see, e.g., [40,59,60,62,64]). To illustrate this with a simple, but important situation, we consider the resonant two-step excitation from an initial level with $J = 0$ by two linearly polarized light fields. The alignment in the intermediate level with $J = 1$ is transferred to the final channels J (in general, $J = 0, 1, 2$; for ARS with $\ell' = 0$ only $J = 0, 1$) in a way which depends on the angle α between the two electric-field vectors. The α-dependent total cross section is given by [62] (see also [128])

$$\sigma(\alpha) = [1 + 2P_2(\cos\alpha)]\sigma_0 + [1 - P_2(\cos\alpha)]\sigma_1 + [1 + \tfrac{1}{5}P_2(\cos\alpha)]\sigma_2, \qquad (5)$$

where σ_J are the J-specific cross sections for photoionization from the intermediate level in the absence of alignment (equal population of all magnetic sublevels) and $P_2(\cos\alpha) = \frac{3}{2}\cos^2\alpha - \frac{1}{2}$. For $\alpha = 0°$ and $\alpha = 90°$, one obtains $\sigma(0°) = 3\sigma_0 + \frac{6}{5}\sigma_2$ and $\sigma(90°) = \frac{3}{2}\sigma_1 + \frac{9}{10}\sigma_2$, i.e., the $J = 1$ ($J = 0$) final state is selectively 'switched off' for $\alpha = 0°$ (90°). In terms of $\sigma(0°)$ and $\sigma(90°)$, the total cross section for the unpolarized intermediate level ($\sigma_{\rm tot} = \sigma_0 + \sigma_1 + \sigma_2$) is given by

$$\sigma_{\rm tot} = \frac{1}{3}\sigma(0°) + \frac{2}{3}\sigma(90°). \qquad (6)$$

It can be measured directly at the 'magic' angle $\alpha_{\rm M} = 54.7°$ ($P_2(\alpha_{\rm M}) = 0$).

Polarization-dependent measurements can be exploited to determine the J-specific cross sections, as achieved, for instance, for two-step photoionization of ground state Xe atoms via the $7s[3/2]_1$ intermediate level in the energy range of the $8p'$ $J = 0, 1, 2$ resonances [59, 126], see section 5.2.1.

2.1.3. Photoexcitation from metastable levels. A large variety of bound and autoionizing Rydberg states with even or odd parity can also be reached by one- or two-photon laser excitation of rare-gas atoms in the metastable $mp^5(m+1)s\ ^3P_0$ and $^3P_2$ levels ($1s_3$ and $1s_5$ in Paschen notation). These levels cannot decay to the $mp^6\ ^1S_0$ ground state through an electric-dipole transition and have long lifetimes (see table 2) [129]. In contrast, the $mp^5(m+1)s, J = 1$ levels ($^1P_1$ ($1s_2$) and $^3P_1$ ($1s_4$) states mixed by spin–orbit interaction) have lifetimes of a few nanoseconds (see [130, 131] and references therein).

Investigations of (autoionizing) Rydberg states from metastable levels can be carried out in discharges by optogalvanic spectroscopy (see, e.g., [43, 44] and section 2.2.2) or by using beams of metastable rare-gas atoms (see, e.g., [25, 36] and section

2.2.3). Resonant two-colour excitation spectra from the metastable levels can be simplified (thus helping to assign ARS) by proper choice of the polarizations of the two light fields [40, 132] (see also sections 2.1.2, 4.2, and 5.2).

The different methods for the production of beams of metastable rare-gas atoms have been reviewed by Gay [133] (see also [134–136] for more recent works). These methods include the extraction of thermal beams from differentially pumped DC or microwave discharges. Metastable rare-gas atoms may be also formed by electron impact on gas flowing from an effusive or a supersonic nozzle. Optimized metastable fluxes for Ne–Xe are in the range $10^{14} - 10^{15}\,\mathrm{s}^{-1}\mathrm{sr}^{-1}$ with most of the population in the $J = 2$ level [69–71, 133, 137]. In few cases, fast beams of metastable rare-gas atoms were used, created by passage of accelerated rare-gas ions through a gas-filled neutralizer cell [28, 138, 139].

2.2. Spectroscopy and detection of autoionizing Rydberg states

2.2.1. Absorption methods. Because the autoionizing Rydberg states normally decay relatively fast by Coulomb interaction, it is difficult to observe them in fluorescence spectra (as possible for the bound states below the first ionization threshold). Consequently, they have been first observed in absorption spectra from the ground state [3]. However, Thekaekara and Dieke have observed photon emission spectra from $n\mathrm{p}'$ and nf' autoionizing states of krypton and xenon [140]. In a typical absorption measurement, the VUV radiation from a gas discharge lamp or a synchrotron is dispersed using a monochromator (see section 2.1.1) and the absorption by the rare gas is detected with photographic plates or a photodetector [3, 15, 16, 141–153]. Care has to be taken to avoid lineshape broadening associated with saturated absorption, especially for strong series.

Absorption from lower excited states of rare-gas atoms to bound and autoionizing Rydberg states can be studied in discharges by long-pathlength experiments such as cavity-ring-down spectroscopy (see, e.g., [154] and references therein).

2.2.2. Optogalvanic spectroscopy. A sensitive method for the study of excited states is optogalvanic spectroscopy (OGS), where the change in the electric properties of the discharge upon laser irradiation is detected [155]. OGS allows one to study transitions from excited levels in the discharge, either metastable or even short lived. It is a practical technique, and it can be used with a small sample volume, which makes it interesting for studies of rare isotopes. For the study of autoionizing Rydberg states,

radio-frequency (RF) discharges [27, 43] and DC discharges [32, 44, 48–50, 156–159] have been used (the same discharge types were used for the study of bound Rydberg states below the first ionization threshold [156, 160–166]). Hollow-cathode lamps filled with neon or argon are usually used for laser frequency calibration. In cases where useful signals can only be produced by strongly driving the transitions, the measured linewidths may easily be broadened by saturation effects. For obtaining reliable natural widths, intensity-dependent measurements should be carried out and the results extrapolated to zero intensity (see also section 2.4). Normally, OGS spectra are subject to Doppler broadening; this aspect does not cause problems for many ARS because of their large natural widths. For high-resolution spectroscopy of narrow lines, different methods such as Doppler-free OGS have been developed [167–170].

2.2.3. Atomic beam methods. Spectroscopy of bound and autoionizing Rydberg states at very high resolution requires—apart from exciting light sources of very narrow bandwidth (such as tunable single-mode cw lasers)—an environment free of perturbations arising from atomic collisions and electromagnetic fields. Their influence leads to shifts and/or splittings of the atomic levels and thus broadening of the transitions [171, 172]. It is also desirable to suppress the broadening of the lines by the Doppler effect. Thus, collimated atomic beams propagating in high vacuum and an electromagnetically shielded volume, and excited transversely by narrowband radiation, are very well suited for high-resolution spectroscopy. Broadening associated with the finite transit time of the atoms through a laser beam and the second-order Doppler effect are normally negligible in ARS studies.

A typical beam apparatus for resonant two-step photoionization studies of (metastable) rare-gas atoms is sketched in figure 4. A well-collimated atomic beam, originating from a differentially-pumped thermal atom source or formed in a supersonic expansion, is crossed at right angles by two anticollinear laser beams. The first laser (or narrowband VUV light in the case of ground-state atoms) with wavelength λ_e excites the atoms from the initial to the intermediate level of interest, and the second laser (λ_i) induces ionization from the intermediate level. The resulting photoions are analyzed mass-spectrometrically and detected by an electron multiplier followed by suitable electronics for signal sampling. Alternatively, the photoelectrons may be analyzed with respect to their energy and emission angle to determine partial cross sections (when more than one final ion state is accessed) and photoelectron angular distributions.

As indicated in figure 4 and realized in most experiments so far, linear polarizations

for the two light beams are chosen. The respective electric vectors $\overrightarrow{E_e}$ and $\overrightarrow{E_i}$ (α denotes the angle between their directions) can be rotated around the propagation direction of the light beams. Thus photoelectron angular distributions (see sections 2.2.4 and 5.3) can be measured with a fixed direction (in the laboratory frame) for electron detection; the electron emission angle θ is understood to be the angle between $\overrightarrow{E_i}$ and the momentum direction of the detected electron.

To avoid Stark broadening of the investigated spectra (especially for Rydberg states with near-integer quantum defect), a scheme should be used involving pulsed excitation under field-free conditions followed by time-delayed charged-particle extraction. The Stark broadening of hydrogen-like Rydberg states with principal quantum number n amounts to $\Delta\nu/\mathrm{MHz} = 3.84n^2\left(F/(\mathrm{V\,cm^{-1}})\right)$ ($3Fn^2$ in atomic units) where F denotes the electric field strength [124].

Bound Rydberg states (of special interest for MQDT) can be transformed to ion–electron pairs by state-selective ionization in a pulsed electric field [172]. A continuous detection process for long-lived Rydberg atoms is electron transfer to electron-attaching molecules such as SF_6 [173, 174]; this method works over a broad range of principal quantum numbers. When a supersonic beam of SF_6 molecules is used, the long-lived SF_6^- ions formed by electron transfer can be detected with high efficiency even without the need for an extracting electric field. Residual electric fields down to 10 mV/m have been achieved in this way [175]. Schemes for minimizing residual electric fields to very low levels have been described in [176, 177].

2.2.4. Photoelectron angular distribution. Atomic beam methods are also useful in studies of photoelectron energy spectra and photoelectron angular distributions (PAD) which provide more detailed information on the photoionization dynamics than total cross sections. A wealth of information exists on PAD following nonresonant single-photon ionization of ground-state rare-gas atoms [178]. For electric-dipole photoionization of isotropic (unpolarized) atoms, the PAD is characterized by the anisotropy (or asymmetry) parameter β ($-1 \le \beta \le +2$). For linearly-polarized light the PAD has cylindrical symmetry around the electric vector, and the angle-differential cross section is given by [179]

$$\mathrm{d}\sigma/\mathrm{d}\Omega(\theta) = (\sigma_{\mathrm{tot}}/4\pi)[1 + \beta P_2(\cos\theta)], \tag{7}$$

where σ_{tot} is the angle-integrated cross section, θ denotes the angle between the electric vector of the light and the momentum of the photoelectron, and $P_2(\cos\theta) \equiv (3\cos^2\theta - 1)/2$.

Rather few measurements of the variation of the PAD parameter β with energy across the ARS of Ne–Xe have been carried out [14,18,31,51,52,180–182]. PAD studies involving selected excited states of the rare-gas atoms are also scarce [31, 57, 69–71, 183–186]. The introduction of angle- and energy-resolved imaging of the photoelectrons [187,188] has enabled efficient sampling of PADs from multiphoton ionization [187,189] or from photoionization of excited rare-gas atoms at low density [185,186].

2.3. Measurements of absolute photoionization cross sections for excited states

Normally, excited-state densities are too small for the measurement of photoionization cross sections by photoabsorption, even at the peak of a strong ARS with cross sections around 1 Gb (1 b (barn) = 10^{-28} m^2). Therefore, methods have to be used which sample the ion or electron signal or detect the depletion of the excited-state density caused by the photoionization process. Such methods were mainly developed for, and applied so far in, photoionization studies of excited alkali- and alkaline-earth-metal atoms formed by selective one- or two-step laser excitation of ground-state atoms in atomic beams (see, e.g., [190,191]).

A powerful method which does not require knowledge of the excited-state density nor a calibration of the charged-particle detector takes advantage of saturating the ionization step with a sufficiently intense (pulsed) laser [190, 192, 193]. A fit of the intensity-dependent ionization signal up to high intensities (where the signal saturates) yields the ionization cross section. Beautiful illustrations of the saturation method are presented in [190]. Excited states with $J \geq 1$ ($J \geq 1/2$), created by absorption of linearly (circularly) polarized light are normally aligned (oriented) when applying the saturation method, and thus the measured cross section is that for an aligned (oriented) atomic sample. The cross section for such polarized excited samples is generally different from the photoionization cross section for excited states with equal population of all magnetic sublevels. For excited states of rare-gas atoms, the saturation method has been applied by Gisselbrecht *et al* [194] and by Baig and coworkers [158,159,195].

Photoionization-induced depletion of excited states is another method to measure photoionization cross sections without the explicit knowledge of the excited state density and the ion collection efficiency. Bonin *et al* [196] have utilized the reduction in the excited-state fluorescence, as induced by pulsed-laser ionization, to determine the photoionization cross section of the $7d_{3/2}$ state of Cs. The competition with spontaneous decay requires rapid photoionization and a time-resolved measurement. Stationary targets of excited atomic states such as those present in magneto-optical traps can also be

used to determine photoionization cross sections for these (normally polarized) excited states [197]. The photoionization-induced losses are usually significantly larger than other trap losses. The photon fluence, the excited-state fraction, and the overlap factor of the trapped excited states with the photon beam have to be determined carefully when using this method, which has been applied to photoionization of Ne (3p, $J = 3$) atoms at two ionizing wavelengths [84] (see also [73]).

Other methods of determining photoionization cross sections normally require the nontrivial tasks of determining the excited-state density and of calibrating the charged-particle detector. For Rydberg states of sufficiently high n and correspondingly long lifetimes, (pulsed) ionization by an electric field is a straightforward way to measure the number of excited atoms present in the volume of interest [172]. The situation is more complicated for low-lying excited states which have shorter lifetimes and require very large pulsed fields. In a photoionization experiment on the excited Cs (7s) level with an intense continuous laser, Gilbert *et al* [198] measured the excited-state density resulting from pulsed laser pumping by determining the time-integrated and solid-angle-corrected fluorescence yield with an uncertainty of only 5%. These authors also proposed a technique for the absolute measurement of photoionization cross sections for excited states based on modulated fluorescence.

For rare-gas atoms, rather few absolute measurements of photoionization cross sections for excited states have been carried out to date. In part, this situation can be explained by the rather low excited-state densities which can be achieved in atomic beams. The quantification of excited-state densities, produced by VUV excitation from the ground state or present in discharges, is difficult, and thus the saturation method has been applied in these cases [158, 159, 194, 195]. Likewise, measurements of the absolute flux of rare-gas atoms in metastable levels is demanding [199]. Dunning *et al* [200] used pulsed lasers and Schohl *et al* [137] employed continuous lasers to measure the electron emission coefficient for impact of metastable rare-gas atoms on (gas-covered) surfaces by means of a photoionization depletion technique and thereby determined the flux of the metastable atoms (see also [199]). Time-of-flight analysis or Doppler-shifted fluorescence yield the atom velocities, and the selective laser-induced removal of one of the two metastable levels can be used to determine the relative densities of the metastable levels. Combining these methods, the state-resolved density of the two metastable states can be obtained. In this way, Kau *et al* determined the photoionization cross sections of the metastable levels of Ne [69], Ar, Kr [71], and Xe [70] to either ion state ($^2P_{3/2}$ and $^2P_{1/2}$) at a few wavelengths with a calibrated electron spectrometer.

Saturated excitation of the closed transition from the metastable $(m{+}1)$s $J = 2$ level to the $(m{+}1)$p $J = 3$ level [183] with a linearly (or circularly) polarized laser results in a quasi-stationary population of aligned (or oriented) $(m{+}1)$p $J = 3$ atoms with known density. This has been exploited to measure absolute photoionization cross sections of the $(m{+}1)$p $J = 3$ level of Ne [183], Ar [132, 201], and Kr [201].

2.4. Analysis of lineshapes of autoionizing Rydberg states

In the majority of the experimental work on autoionizing resonances $n\ell'[K']_J$, the measured lineshapes have been compared with fitted Fano profiles to deduce the parameters E_0, Γ, and q in (3). Fano profiles provide a useful description of ARS in cases where the width $\Gamma(n)$ is significantly smaller than the energy spacing ΔE_n between adjacent ARS of the same series so that the resonances can be considered as "isolated". Overlapping ARS of different J value do not interact, and their composite lineshape can be described by a superposition of independent Fano profiles. A proper description for the general case is provided by multichannel quantum defect theory (MQDT) (see section 3.1).

The values for the resonance energy E_0 and the width Γ depend more or less strongly on the quantum numbers n, ℓ', K', and J. At sufficiently high n values, the n dependence of E_0 is well described by the Rydberg formula

$$E_0(n) = E_{1/2} - \frac{R_M hc}{(n-\mu_{\ell'})^2}. \tag{8}$$

Here $E_{1/2}$ is the energy of the $m\mathrm{p}^5\,{}^2\mathrm{P}_{1/2}$ threshold, R_M is the mass-dependent Rydberg constant for the isotope in question, and $\mu_{\ell'}$ is the quantum defect of the ARS series which mainly depends on ℓ', but also weakly on K' and J.

The uncertainty ΔE_0 of a measured resonance energy and the uncertainty $\Delta\mu$ of the determined quantum defect μ are connected through

$$\Delta\mu = \frac{(n-\mu)^3}{2hcR_M}\,\Delta E_0. \tag{9}$$

The uncertainty ΔE_0 is influenced by the uncertainty ΔE_p of the photon energy, by the uncertainty $\Delta E_{1/2}$ of the ionization energy $E_{1/2}$, and by the uncertainty ΔE_p with which the resonance energy E_0 can be extracted from a fit of equation (3) to the resonance profile. Clearly ΔE_p depends on the width Γ and is smaller for narrow resonances (as long as shifts and/or line broadening by ac or dc electromagnetic fields can be neglected). For small quantum defects ($\mu \ll 1$), as typically observed for

$\ell' \geq 3$, high accuracy ($\Delta\mu/\mu \ll 1$) can only be achieved at low n values with narrow-bandwidth photon sources ($\Delta E_{\rm p}$ small), using either cw lasers or Fourier-transform-limited pulsed lasers with Gaussian temporal profile and duration $\gtrsim 5\,$ns (frequency width $\Delta\nu \lesssim 100\,$MHz $\widehat{=}\ 0.0033\,{\rm cm}^{-1}$) in conjunction with accurate wavemeters. For narrow resonances with $n - \mu = 10$, an overall error $\Delta E_0 = 0.01\,{\rm cm}^{-1}$ translates to $\Delta\mu = 5 \times 10^{-5}$, as achieved, e.g., in pulsed laser excitation of Ar $(n{\rm f}')$ resonances ($\mu_{\rm f} = 0.01144(3)$ [34]). However, the energy dependence of the quantum defects has stronger effects on the value of μ at low n values.

The autoionization width Γ rapidly decreases with rising n and ℓ', and—for given n, ℓ'—depends rather weakly on K' and J, as will be discussed in more detail in Section 4. At sufficiently high n values, $\Gamma(n) \propto (n^*)^{-3}$ ($n^* \equiv n - \mu$ denotes the effective principal quantum number) [1, 76, 202], and a reduced width $\Gamma_{\rm r}$

$$\Gamma_{\rm r} = (n^*)^3 \Gamma(n) \tag{10}$$

is introduced to characterize the natural width of a resonance series $n\ell'[K']_J$. At lower n, both the quantum defect $\mu_{\ell'}$ and the reduced width exhibit a residual dependence on n, i.e., on the energy, as mentioned above and discussed in detail, e.g., for the $n\ell'$ ($\ell' = 0, 2$) series in Xe [48]. The relative uncertainties of the experimentally determined reduced widths may be as small as one percent [26,31], but more typically lie in the range 5–50%. They are normally not limited by the uncertainty in establishing the (relative) energy scale. Other effects such as the energy width of the photon source, noisy signals and/or saturation broadening (when pulsed lasers are used) often dominate the error budget.

If the energy width of the photoionizing light (spectral distribution $F(E)$) is not small compared to the natural resonance width Γ, the measured resonance profile $M(E)$ should be compared with a calculated lineshape $C(E)$, obtained by convolution of the resonance cross section $\sigma(E)$ with $F(E)$, i.e.,

$$C(E) = \int F(E') \cdot \sigma(E - E')\,{\rm d}E' \tag{11}$$

in order to determine the natural width Γ. As a test and means to check for systematic errors, it can also be helpful to measure resonance profiles at different values of n and compare with the corresponding calculated profiles $C(E)$ using equation (10) to scale the widths.

In order to outline the problems associated with saturation broadening of measured resonance profiles, we assume a Lorentzian lineshape of the ARS $\sigma(\epsilon) = \sigma_0/(1 + \epsilon^2)$

($\sigma_0 \equiv \sigma(\epsilon=0)$, $\epsilon = 2(E - E_0)/\Gamma$), excited by a (pulsed) laser with (average) photon fluence ϕ [photons/area] and a bandwidth small compared to the natural width Γ. The ionization probability is given by

$$P(\epsilon, \phi) = 1 - \exp[-\phi(\epsilon)\sigma(\epsilon)]. \tag{12}$$

If $\phi\sigma_0 \ll 1$, $P(\epsilon, \phi) \ll 1$ at all ϵ, and the energy dependence of the ionization probability function $P(\epsilon, \phi)$ matches that of the ionization cross section $\sigma(\epsilon)$. The full width at half maximum (FWHM) of the resonance is $\Delta\epsilon = 2$ and corresponds to the energy width $\Delta E_{\mathrm{FWHM}} = \Gamma$. This situation is normally encountered when cw lasers are used. With pulsed lasers, however, saturation conditions ($\phi\sigma_0 \gtrsim 1$) are easily fulfilled, even at moderate fluences $\phi \lesssim 10^{16}\,\mathrm{cm}^{-2}$ because for strong ARS, the peak cross section σ_0 often reaches values above 10^{-16} cm^2 (100 Mb).

Saturation results in a significant broadening of the normalized ionization probability function $N(\epsilon, \phi) = P(\epsilon, \phi)/P(\epsilon{=}0, \phi)$, as normally evaluated at $N(|\epsilon|, \phi) = 0.5$. For the case $\phi\sigma_0 = 3$, the condition $N(\epsilon, \phi) = 0.5$ is fulfilled for $\epsilon \approx \pm 2$, hence the saturation broadening amounts to a factor of about 2. In order to make sure that saturation broadening does not influence the extracted resonance width Γ, measurements at different photon fluences have to be carried out (see, e.g., the studies of Ar $(n\mathrm{f}')$ resonances in [34]).

The lineshape of the ARS is determined by the profile index q. The uncertainty in determining q is highest for high $|q|$ values for which also the sign of q is difficult to determine. For lineshapes with $|q| \lesssim 5$, the relative error $\Delta q/|q|$ is lower. The background cross section σ_b in (3) is part of the fitting procedure and also has some influence on the error budget for q.

3. Theoretical description

The theoretical description of the outer-shell photoionization of the rare-gas atoms is based on different modifications of either the central-field (CF) approach or multichannel quantum defect theory (MQDT). CF approaches use calculated atomic orbitals as a starting point to compute matrix elements of the energy operator and the transition moments in a perturbation-theory treatment. MQDT is based on scattering theory and is able to describe the energy-level structure and many spectral features with a relatively small set of parameters, such as transition dipole amplitudes and eigen-quantum defects. *Ab initio* CF approaches can also be used to compute the MQDT parameters [65, 66] and to describe the photoionization process.

We begin this section with a brief description of the MQDT treatment of atomic spectra and then describe semi-empirical and *ab initio* CF approaches, omitting, however, the fully *ab initio* large-scale many-configurational approaches (see, e.g., [203–208] and references therein). We conclude the section by describing the *ab initio* CIPFCP approach which was used recently for the calculation of the outer-shell photoionization of Ne, Ar, Kr, and Xe [70, 72, 74, 77].

3.1. MQDT analysis

Many of the features of complex atomic spectra and single-electron ionization can be described in terms of a few important dynamical parameters using scattering theory in the form of multichannel quantum defect theory (MQDT) [209–212]. MQDT treats the Rydberg states and photoionization from the perspective of a collision between an ion core and a Rydberg electron with an attractive electrostatic potential. The word "channel" indicates a set of states that consist of an electron of arbitrary energy and a target ion in a specific quantum state; specification of the angular momenta of the electron and cationic core, and of their coupling, completes the identification of a channel [210,213]. If the energy of the electron lies below the ionization limit, the state belongs to the series of discrete bound states (Rydberg series) and the channel is said to be "closed"; if the energy of the electron is higher than the limit, the state belongs to the adjoining continuum and the channel is said to be "open". Perturbations between Rydberg series and configuration interaction (resulting from correlations between Rydberg electron and core electrons) are treated as channel mixing. Autoionization is described in MQDT as inelastic scattering of an electron in a closed channel into an open channel by collision with the ionic core [213]. A remarkable feature of MQDT is its ability to represent the effects of all interactions by means of a small set of physically meaningful parameters: eigen-quantum defects μ_α representing short-range electron–core interactions, dipole matrix elements D_α, the energy levels of the ion $E_i = E_{\rm ion}(J^+F^+)$, and the frame transformation $U_{i\alpha}$ between the angular momenta coupling schemes of the close-coupling eigenchannels α and of the dissociation or ionization channels i [210, 213, 214].

To analyze the Rydberg spectra of rare gases, we follow the formalism introduced by Fano and coworkers [215–220] on the basis of Seaton's MQDT theory [209, 221–223]. This approach has been extended to include relativistic effects [66, 68, 224, 225], was successfully applied to study the bound and autoionizing Rydberg states of rare gases [36–38, 40, 45, 139, 150, 151, 162, 226–234], and could be easily adapted to analyze the hyperfine structure of bound and autoionizing Rydberg states of rare

gases [21, 22, 235–237]. Some authors adopted slightly different formulations (phase-shifted MQDT [238–241] or complex quantum defects [242]) in their studies of rare gases [42, 44, 46, 49, 164–166, 243]. An extension of the MQDT method [244, 245] has been used to treat the Stark effect in bound and autoionizing Rydberg states of argon and neon [63, 246–248].

For the MQDT analysis of rare gases, two different angular momentum coupling schemes are used. In the close-coupling region of the electron–ion collision, the electrostatic interaction between the electron and the ion core is larger than the spin–orbit and much larger than the hyperfine interaction [217]. Therefore, the following (LS) angular momentum coupling scheme is adequate to describe the close-coupling eigenchannels:

$$\vec{L}^+ + \vec{\ell} = \vec{L}, \quad \vec{S}^+ + \vec{s} = \vec{S}, \quad \vec{L} + \vec{S} = \vec{J}, \quad \vec{J} + \vec{I} = \vec{F}, \tag{13}$$

where $\vec{L}^+$ and $\vec{S}^+$ represent the orbital and spin angular momenta of the ionic core, $\vec{\ell}$ and $\vec{s}$ the corresponding angular momenta of the Rydberg electron, and $\vec{I}$ the nuclear spin. In the long-range part of the electron–ion collision, however, the energy-level structure of the Rydberg states corresponds primarily to the energy levels of the ionic core. Thus the following (F^+j) coupling scheme (or J^+j for isotopes with zero nuclear spin) is used for the dissociation (or fragmentation) channels:

$$\vec{L}^+ + \vec{S}^+ = \vec{J}^+, \quad \vec{J}^+ + \vec{I} = \vec{F}^+, \quad \vec{\ell} + \vec{s} = \vec{j}, \quad \vec{F}^+ + \vec{j} = \vec{F}. \tag{14}$$

In the discrete part of the spectrum, i.e., at energies lower than the lowest ionization threshold, the equation

$$\sum_\alpha U_{i\alpha} \sin[\pi(\mu_\alpha + \nu_i)] A_\alpha = 0, \tag{15}$$

which requires the wavefunction of the bound levels to vanish at infinity, is used to determine the positions of the bound Rydberg states. ν_i is an effective principal quantum number $\nu_{J^+F^+}$ defined by

$$E = E_{\rm ion}(J^+F^+) - \frac{hcR_M}{(\nu_{J^+F^+})^2} \tag{16}$$

with the mass-dependent Rydberg constant R_M and the ion energy level $E_{\rm ion}(J^+F^+)$ associated with the dissociation channel i. The elements $U_{i\alpha}$ of the transformation matrix $\boldsymbol{U}$ differ slightly from the elements $\bar{U}_{i\bar{\alpha}} = \langle LSJF|J^+F^+jF\rangle$ (as given in Refs. [236, 237]) of the $F^+j - LS$ frame transformation matrix $\bar{\boldsymbol{U}}$ because of the spin–orbit interaction and the deviation of the electrostatic potential from a pure Coulomb

potential. For example, $\bar{\boldsymbol{U}}$ is diagonal in ℓ, F, and (for $I = 0$) J, whereas $\boldsymbol{U}$ can have matrix elements connecting eigenchannels differing in ℓ by 2. The coefficients A_α enable the expansion of the dissociation channels in the basis of the close-coupling eigenchannels. Equation (15) has nontrivial solutions when

$$\det |U_{i\alpha} \sin[\pi(\mu_\alpha + \nu_i)]| = 0, \tag{17}$$

and the values of ν_i satisfying this relation correspond to the bound Rydberg levels.

If the total energy lies between the lowest and the highest ionic level included in the MQDT model, some dissociation channels are closed (forming an ensemble denoted Q) and some are open (forming an ensemble labeled P). In addition to the boundary condition represented by (15) for the closed channels, the open-channel wavefunctions should behave at large r as collision eigenfunctions of the open channels, labeled ρ, with a phase shift $\pi\tau_\rho$; this boundary condition is represented by the following equation:

$$\sum_\alpha U_{i\alpha} \sin[\pi(-\tau_\rho + \mu_\alpha)] A_\alpha = 0. \tag{18}$$

For each value of the total energy in the autoionizing region, there are as many solutions τ_ρ and associated vectors of expansion coefficients $\boldsymbol{A}^\rho$ as open channels. These coefficients are obtained in a single step by solving the equation [210]

$$\boldsymbol{\Gamma A}^\rho = \tan(\pi\tau_\rho) \boldsymbol{\Lambda A}^\rho, \tag{19}$$

where

$$\Gamma_{i\alpha} = \begin{cases} U_{i\alpha} \sin[\pi(\mu_\alpha + \nu_i)] & \text{for } i \in Q, \\ U_{i\alpha} \sin(\pi\mu_\alpha) & \text{for } i \in P, \end{cases} \tag{20}$$

$$\Lambda_{i\alpha} = \begin{cases} 0 & \text{for } i \in Q, \\ U_{i\alpha} \cos(\pi\mu_\alpha) & \text{for } i \in P. \end{cases} \tag{21}$$

The total photoionization cross section is

$$\sigma(\omega) \propto \omega \sum_F \frac{2F+1}{2F_0+1} \sum_\rho \frac{1}{N_\rho} \left(\sum_{\alpha'} \sum_\alpha D_{\alpha'\alpha} A_{\alpha'} A_\alpha^\rho \right)^2, \tag{22}$$

where ω is the photon energy, F_0 the total angular momentum quantum number of the initial state, $D_{\alpha'\alpha}$ is the reduced dipole matrix element for a transition between eigenchannel α' of the initial state and eigenchannel α of the final state, and the normalization factor N_ρ is given by

$$N_\rho^2 = \sum_{i \in P} \left(\sum_\alpha U_{i\alpha} \cos[\pi(-\tau_\rho + \mu_\alpha)] A_\alpha^\rho \right)^2. \tag{23}$$

The theory has been extended to describe the photoelectron angular distribution [66, 218, 220, 228, 229, 232].

Because the electrostatic interaction in the close-coupling region is much larger than the hyperfine interaction, the same sets of eigen-quantum defects μ_α and dipole transition amplitudes $D_{\alpha'\alpha}$ can be used for all isotopes and all F values. In this approximation, the parameter set for $^{A=\mathrm{odd}}$Rg ($I \neq 0$) differs from that of $^{A=\mathrm{even}}$Rg ($I = 0$) only by the additional parameters describing the hyperfine structure of the ion $E_{\mathrm{ion}}(J^+F^+)$ and a small isotope shift of the ion energy level with respect to the ground state of the neutral atom [21, 22, 236, 237].

The eigen-quantum defects μ_α, the eigen-dipole amplitudes $D_{\alpha'\alpha}$, and the frame transformation matrices $U_{i\alpha}$ are slowly varying functions of energy near the ionization thresholds (see figures 1 and 2 in [66] and [217, 219]). In most treatments, the energy dependence was restricted to the eigen-quantum defects [46, 139, 162, 227, 229, 231, 232, 243]. Even for the description of high-n Rydberg states of krypton and xenon studied with very high resolution, it was sufficient to use a linear energy-dependence of the eigen-quantum defects [22, 235–237]. In the energy range of the strongly bound low-n Rydberg states, the energy-depence of the μ quantum defect parameters becomes pronounced and the calculations may yield unphysical solutions; methods that avoid such artefacts have been proposed [249].

3.2. Central-field approach with core polarization

The basic assumption of the central-field (CF) approximation is that the movement of each electron takes place in the spherical field of the nucleus and the average field of the other electrons [250–252]. With this assumption, the structure of the single-electron wave function (including spin) is the same as for the hydrogen atom, i.e., $\phi_{n\ell s m_\ell m_s}(r,\theta,\varphi) = \frac{1}{r}P_{n\ell}(r)Y_{\ell m_\ell}(\theta,\varphi)\chi_{m_s}(s)$, but the nonhydrogenic radial part $P_{n\ell}(r)$, denoted as atomic orbital (AO), is determined within the nonrelativistic approximation by solving the equation

$$\left(-\frac{\mathrm{d}^2}{\mathrm{d}r^2}+\frac{\ell(\ell+1)}{r^2}+V_{n\ell}^{\mathrm{CF}}(r)\right)P_{n\ell}(r) = \varepsilon_{n\ell}P_{n\ell}(r). \tag{24}$$

Atomic units are used in sections 3.2 and 3.3 except for the energies, for which we adopt Rydberg units (1 Ry = 13.6057 eV) unless specified otherwise; ℓ is the orbital angular momentum quantum number; $\varepsilon_{n\ell}$ is a variational parameter corresponding to the single-electron energy. The central field potential $V_{n\ell}^{\mathrm{CF}}(r)$, depending on the approximation,

consists of several parts:

$$V_{n\ell}^{\mathrm{CF}}(r) = V_{n\ell}(r) - X_{n\ell}(r) + V^{\mathrm{CP}}(r). \tag{25}$$

The potential term $V_{n\ell}(r)$ includes the potential $-2Z/r$ and the local part of the electron–electron interaction; the nonlocal potential $X_{n\ell}(r)$ describes the exchange part of the electron–electron interaction; $V^{\mathrm{CP}}(r)$ is the core-polarization (CP) potential accounting for the influence of the excited configurations on $P_{n\ell}(r)$. The relativistic corrections can be included in equation (24) using the Breit–Pauli operator [250]. The major relativistic terms to be added to $V_{n\ell}^{\mathrm{CF}}(r)$ are the mass–velocity $H_{n\ell}^{\mathrm{m}}(r)$, the one-electron Darwin $H_{n\ell}^{\mathrm{D}}(r)$, and the spin–orbit $H_{n\ell}^{\mathrm{SO}}(r)$ corrections. The expressions for these corrections can be obtained by transforming the system of two first-order Dirac–Fock integro-differential equations for the 'large' and 'small' components of the fully relativistic single-electron wave function to a single second-order equation for $P_{n\ell}(r)$ [252]:

$$H_{n\ell}^{\mathrm{m}}(r) = -\frac{\alpha^2}{4}\left(\varepsilon_{n\ell} - V_{n\ell}(r)\right)^2, \tag{26}$$

$$H_{n\ell}^{\mathrm{D}}(r) = -\delta_{\ell,0}\frac{\alpha^2}{4}\left[1 + \frac{\alpha^2}{4}\left(\varepsilon_{n\ell} - V_{n\ell}(r)\right)\right]^{-1} \cdot \frac{\mathrm{d}V_{n\ell}(r)}{\mathrm{d}r}\left[P_{n\ell}(r)/r\right]^{-1}\frac{\mathrm{d}\left[P_{n\ell}(r)/r\right]}{\mathrm{d}r}, \tag{27}$$

$$H_{n\ell j}^{\mathrm{SO}}(r) = \frac{j(j+1) - \ell(\ell+1) - s(s+1)}{2} \cdot \frac{\alpha^2}{2}\left[1 + \frac{\alpha^2}{2}(\varepsilon_{n\ell} - V_{n\ell}(r))\right]^{-1}\frac{1}{r}\frac{\mathrm{d}V_{n\ell}(r)}{\mathrm{d}r}. \tag{28}$$

In these equations, $\alpha = 1/137.036$ is the fine-structure constant, and $V_{n\ell}(r)$ denotes the local part of the Hartree–Fock (HF) potential. Inserting (26)–(28) into (24) yields the 'Pauli–Fock' radial functions $P_{n\ell j}(r)$ where j is the total angular momentum quantum number of the electron ($\vec{j} = \vec{\ell} + \vec{s}$).

3.2.1. Local-density approximation. In early *ab initio* calculations, the core-polarization and relativistic effects were neglected and the nonlocal exchange potential $X_{n\ell}(r)$ was replaced by its local version introduced by Slater [253]. $P_{n\ell}(r)$ functions computed within the local-density approximation (LDA) have been tabulated by Herman and Skillman [254] for the ground states of atoms with $2 \le Z \le 102$ and used in many subsequent calculations. As an example of such calculations related to the present review, we mention [255] where LDA $P_{n\ell}(r)$ [254] were used without any additional corrections for computing the photoionization cross sections of the excited $n\ell\,(\ell = 0 - 3)$ electrons in Cs. As an alternative to the LDA, semi-empirical core–electron potentials were employed [256] with parameters chosen to provide the best

fit to the available experimental data (e.g., excitation energies). The core–electron potential of [256] has been used in [257] to compute the photoionization cross sections of the excited states of Li, Na, and K.

3.2.2. Hartree–Fock approximation. A better approximation, involving the nonlocal exchange potential $X_{n\ell}(r)$, is the Hartree–Fock (HF) method which generates the most accurate single-electron nonrelativistic AOs. For atoms and some ions with $2 \leq Z \leq 54$, HF AOs have been tabulated by Clementi and Roetti [258]. These AOs were often used for computing the core potential in extended calculations with inclusion of CP and other many-electron correlations [259–262]. The HF approach allows one to take into account many-electron correlations by inclusion of the term dependence of the AO in equation (24), which can substantially change the shape of the radial function $P_{n\ell}(r)$ [263–266] and reduce the residual part of the electron–electron interaction in a subsequent application of many-body perturbation theory (MBPT). Use of term-dependent Hartree–Fock AOs in MBPT calculations marked the starting point for the development of the random-phase approximation with exchange (RPAE) approach [267]. The RPAE approach has been successfully applied in studies of the photoionization dynamics in atoms [268] including autoionization [40,269]. Accounting for the intershell and intrashell correlations in RPAE shed light on the origin of many observed features of atomic photoionization cross sections and photoelectron angular distributions [267,268]. However, this approximation failed to quantitatively describe photoionization from the outer shells of the heavier alkali atoms (see, e.g., figure 5 where the cross sections for the 6s shell of Cs σ_{6s} are displayed). This failure is caused by the neglect of the relativistic compression of the atomic core in RPAE [70].

3.2.3. Dirac–Fock approximation. For atoms with $Z \gtrsim 30$, the relativistic effects should be taken into account in computing AOs. The most rigorous way of doing this is by using the Dirac–Fock (DF) method [270, 271] or its modification using the local exchange potential [272]. By inclusion of relativistic effects (in the LDA version of the DF approach), Walker and Waber [273] explained many features of the photoionization of valence and subvalence shells of the rare gases, but much better agreement between theory and experiment could be reached by including intershell correlations [274]. The most rigorous approach takes both relativistic (in the DF approximation) and many-electron (in the RPA approximation) effects into account and has been developed by Johnson *et al* in studies of the photoionization of the ground state of the rare-gas

atoms [224,275]. This approach is known as the relativistic random-phase approximation (RRPA), and was applied in the first fully *ab initio* calculations of the resonance structure in the photoionization cross sections of the mp^6 valence shell of the rare gases [65, 66]. Figure 5(a) illustrates that relativistic effects shift the Seaton–Cooper minimum (see section 5.1 for a discussion of such minima) in σ_{6s} of Cs by ~ 1.5 eV towards higher photoelectron energies [276], while many-electron effects essentially bring the minimum back to its nonrelativistic position (see figure 5(b)). However, the inclusion of both effects increases the photoionization cross section at high photoelectron energies by almost a factor of two in comparison with the HF calculation (see figure 5).

3.2.4. Pauli–Fock approximation. The number of AOs in the DF approach is larger than in HF because orbitals with $\ell \neq 0$ possess $j = \ell \pm 1/2$ and have 'large' and 'small' components. This leads to a substantial increase in the number of Coulomb (Slater–Condon) integrals and makes the atomic structure calculations cumbersome. Therefore, it is practical to include relativistic effects using the Breit–Pauli operator [250,252]. The computer code with nonlocal exchange has been created by Cowan and Griffin [277] (HFR approach) and by Selvaraj and Gopinathan [278] in LDA version (RΞ approach). It was found that the HFR and RΞ approaches describe the single-electron energies (compared with the DF calculation) with accuracies around 5% and mean radii of AOs with accuracies of 0.3% for atoms with $Z \leq 92$. The small-r deficiencies of the orbitals in the HFR approach were attributed to the neglect of the finite size of the nucleus [277]. This finite-size effect was taken into account in the Pauli–Fock (PF) approach in [70] along the lines of work in [271]. Photoionization cross sections σ_{6s} of Cs computed in the PF approach are compared with the DF calculation [276] in figure 5(a). One can see that these cross sections agree to within a few percent, demonstrating the adequacy of the PF approach for inclusion of the main relativistic effects in atomic calculations. One of the advantages of the PF approach is its ability to perform calculations with step-by-step inclusion of atomic interactions. In particular, omission of the $H^{\rm m}_{n\ell}(r)$ and $H^{\rm D}_{n\ell}(r)$ corrections from the core AO calculation clearly showed that the relativistic shift in σ_{6s} of Cs results mainly from the relativistic compression of the atomic core. Figure 5(b) illustrates that the remaining difference between the measured σ_{6s} of Cs and that computed within the CIPF approach [70] has been removed in [72] by taking into account many-electron correlations beyond intershell correlations by means of an *ab initio* core polarization potential (CP) technique (the CIPFCP approach, described in more detail below).

3.2.5. Core polarization. The idea of the core-polarization potential $V^{\rm CP}(r)$ has been suggested by Born and Heisenberg [279] before the introduction of quantum mechanics. From classical considerations they concluded that at large distances the optical electron should move in a $-\frac{1}{2}\alpha_{\rm d}/r^{-4}$ potential resulting from its interaction with the electric dipole induced in the core. Application of quantum mechanics to the derivation of the $V^{\rm CP}(r)$ potential in 1933 [280,281] confirmed the asymptotic behaviour of this potential, but encountered a divergence problem at small radii. Therefore, Bates suggested to use a 'cut-off' radius $r_{\rm c}$ such that $V^{\rm CP}(r) \stackrel{r\to 0}{=} 0$ [282]. Subsequently, a variety of different 'cut-off' radii were introduced, as reviewed by Meyer *et al* [283,284]. One of the widely used forms of $V^{\rm CP}(r)$ is the potential with the leading term [260, 285–288]

$$V^{\rm CP}(r) = -\frac{\alpha_{\rm d}}{2r^4}\left(1-\exp[-(r/r_{\rm c})^6]\right), \tag{29}$$

where $r_{\rm c}$ is the effective cut-off core radius chosen to reproduce experimental ionization potentials of the outer electrons.

The electric dipole induced by the optical electron in the core changes also the electric-dipole-transition operator. This correction to the transition operator was introduced by Bersuker [289] and later justified by Hameed *et al* [290] in the framework of perturbation theory. The modified electric-dipole-moment operator is given by

$$D(r) = r\left(1-\frac{\alpha_{\rm d}}{r^3}\exp[-(r/r_{\rm d})^3]\right), \tag{30}$$

where $r_{\rm d}$ is an effective cutoff core radius chosen to reproduce experimental quantities, e.g., oscillator strengths.

The potential (29) with the modified transition operator (30) was used, for example, in [285] to compute oscillator strengths and photoionization cross sections of the ground state of alkali-metal atoms. In [285], the core–electron potential was computed from Clementi's data for Na and K [291], and from Hartree's data for Rb and Cs [292, 293]. In the photoionization of Rb(5s) the use of the modified dipole operator resulted in a shift of the Seaton–Cooper minimum by about 1.5 eV towards lower photoelectron energies, i.e., it has a similar effect as the inclusion of inter-shell correlations (see figure 5 for the Cs atom).

The potential (29) and the electric-dipole-moment operator (30) have also been adopted in another calculation [286] of the photoionization cross section of Cs, based on a Thomas–Fermi core–electron potential, but including the spin–orbit interaction in computing the AOs of the $\varepsilon {\rm p}_j$ photoelectrons. With properly adjusted potential parameters, the total cross section (see figure 5) as well as the photoelectron angular

distribution (as discussed by Yin *et al* [294]) agree well with the experimental data [294,295]. As two further examples for the application of the core polarization potential (29) and the transition operator (30) in conjunction with semi-empirical potentials [256, 284], we mention the work on photoionization of the excited $n\ell(n \leq 20; \ell \leq 4)$ states of Rb and Sr^+ [288] and the recent calculation on photoexcitation and -ionization of $Na(3p_{3/2})$ [284]. The latter authors estimate an uncertainty of their cross sections in the range of only a few percent.

Instead of using the modified electric-dipole-moment operator (30), many-electron correlations can be included directly in calculations of the dipole transition moment (see, e.g., [259, 260, 287, 296]). In order to solve this problem and to avoid some divergences in the application of perturbation theory, correlational functions were used (denoted in [259] as 'effective' and in [287] as 'correlationally perturbed' functions). Within this model, Chang computed photoionization cross sections of the Na and K ground states [259] and of the first excited np states of rare gases [296], and Laughlin computed one- and two-photon ionization of the 3s and 3p states of Na I [260]. The AOs [258] were used for computing the core–electron potential in [259, 260, 296]. Aymar used the semiempirical core–electron potential of Klapisch [256] in computing photoionization cross sections of the ground level and excited ns levels of neutral sodium [287].

Using the core polarization potential $V^{\mathrm{CP}}(r)$, equation (29) allows one to correct inaccuracies caused by the approximate calculation of the core–electron potential (e.g., using Thomas–Fermi potential as in [286], LDA [254] as in [255], Hartree–Fock [258] as in [259–261,285,296], or even again semi-empirical [256,284] as in [284,288]). Using such approximations in combination with semi-empirically corrected transition operator $D(r)$ (30) allows one to achieve calculations accurate to within few percent without, however, clarifying the nature of the $V^{\mathrm{CP}}(r)$ potential. In particular for heavy atoms, the single-electron effect of the relativistic compression of the atomic core is attributed to the core polarization. Using corrected transition operators does not allow the determination of the major correlations contributing the photoionization process. It seems that the only way to clarify the role of single- and many-electron effects in photoionization is *ab initio* calculations of the photoeffect as in [72, 224, 267, 268, 275]. The CIPFCP approach used in [72] is described in more detail in the following section.

3.3. Configuration-interaction Pauli–Fock approximation with core polarization

In the configuration-interaction Pauli–Fock approximation with inclusion of core polarization (CIPFCP), the AOs of the occupied and virtual states (including both

discrete and continuum states) are computed, and these orbitals are then used in calculations including many-electron correlations.

3.3.1. Pauli–Fock approach with core polarization in atomic-orbital calculation. In computing the AOs, we take into account relativistic effects with the Pauli–Fock approximation [70]. In this approach the mass-velocity term $H^{\rm m}_{n\ell}$ (26) and Darwin term $H^{\rm D}_{n\ell}$ (27) are included in the self-consistent solution of the Hartree–Fock equations. These terms have spherical symmetry and therefore do not change the usual nonrelativistic configuration, but allow us to take into account the relativistic compression of the atomic core which is found to be considerable for atoms with $Z \gtrsim 30$ [70, 72]. The nucleus is considered as a homogeneously charged sphere with radius $R_{\rm n} = 2.2677 \times 10^{-5}\, A^{1/3}\, a_0$, where A is the mass number (nucleon number) of the atom [271]. The spin–orbit correction (28) for the core shells is usually omitted because it has no substantial influence on the potential of the outer electrons. For the same reason, the Hartree–Fock field (averaged over the configurations and containing in the integral kernel the nonlocal exchange potential) is used at this stage of calculation.

Computed core AOs are used for building the core–electron potential with a vacancy in one of the atomic shells; this potential is frozen for the calculation of the complete set of virtual AOs (including discrete and continuum states). This set of AOs is used to determine the core polarization potential $V^{\rm CP}_\ell(r)$. The potential $V^{\rm CP}_\ell(r)$ has been derived in [72] by applying the variational principle for the total energy of the atom, the second-order correlational corrections being treated as outlined in [297, 298]. As a result the potential $V^{\rm cp}_{n\ell}(r) \otimes P_{n\ell}(r)$ (with integral kernel) for the lowest virtual AO is computed. To compare our core polarization potential with the potentials used in earlier work (see above), we construct the local form of this potential $V^{\rm CP}_{n\ell}(r)$ by simply dividing the product $V^{\rm cp}_{n\ell}(r) \otimes P_{n\ell}(r)$ by the AO $P_{n\ell}(r)$:

$$V^{\rm CP}_\ell(r) = \frac{V^{\rm cp}_{n\ell}(r) \otimes P_{n\ell}(r)}{P_{n\ell}(r)}. \tag{31}$$

The potential $V^{\rm CP}_\ell(r)$ is almost independent of the principal quantum number n, while it contains a significant ℓ dependence. The singularities of $V^{\rm CP}_\ell(r)$ associated with the nodes of $P_{n\ell}(r)$ are not critical in view of the fact that the nodes in $P_{n\ell}(r)$ and in $V^{\rm cp}_{n\ell}(r) \otimes P_{n\ell}(r)$ appear at essentially the same distance r [72]. The core polarization potential (31) has the same asymptotic behaviour as the semi-empirical potential (29), but it is constant at small radii while the potential (29) approaches zero at small r. The complete set of virtual AOs is used for computing the reduction of the most important

Slater integrals entering the potential (31) by applying second-order perturbation theory as described in [77, 297, 298]. The averaged reduction coefficient is used for refining the potential (31) used in the further calculation.

The AOs of the excited and the continuum electron are computed with inclusion of the term dependence, the refined potential $V_\ell^{\rm CP}(r)$ and the spin–orbit correction term $H_{n\ell}^{\rm SO}(r)$ (28).

3.3.2. Reduced widths, photoionization cross sections and resonance lineshapes. In order to include the residual part of the electron–electron interaction in the calculation of photoionization cross sections several techniques have been used. These techniques are illustrated for the case of the $2p^5(^2P_{1/2})n(s/d)'$ resonances of Ne, excited from the $2p^53p$ levels [74]:

$$2p^53p[K]_J\ (2p_x) \ \rightarrow\ 2p^5\,(n/\varepsilon)\,\ell\ \ (\ell = s/d)\ . \tag{32}$$

The $2p^53p$ levels are labeled in Paschen notation as $2p_x$ ($x = 1-10$) and by $[K]_J$ quantum numbers in Racah coupling [5] (see introduction and figure 3). The Racah coupling scheme is better for the strongly interacting levels with $J = 1, 2$ whereas the LS coupling scheme is better for the $2p_1$, $2p_3$ and $2p_{10}$ levels which are practically pure $^1S_0$, $^3P_0$ and $^3S_1$ terms, respectively. The level $2p_9$ ($^3D_3$ or $[5/2]_3$) is pure in both coupling schemes. For the notation of the autoionizing Rydberg states the Racah coupling scheme is better because the 2p spin–orbit interaction is much stronger than the $2p - n\ell$ Coulomb interaction at high n.

The following scheme is adopted for the calculation:

$$\begin{array}{ccc} 2p^53p & \rightarrow & 2p^5\,(n/\varepsilon)\,\ell\ \ (\ell = s/d) \\ \Updownarrow & & \Updownarrow \\ \left\{\begin{array}{ll} 2p^4\,(n/\varepsilon)\,\ell\,\{s/d\} & (a) \\ 2s^12p^6\varepsilon\ell & (b) \\ 2p^5\,\{p/f\} & (c) \end{array}\right\} & & \left\{\begin{array}{ll} 2p^43p\,\{s/d\} & (d) \\ 2s^12p^63p & (e) \\ 2p^5\{s/d\} & (f) \end{array}\right\} \\ \textbf{ISCI} & & \textbf{FISCI} \end{array}\ . \tag{33}$$

Here, the horizontal arrow denotes the electric-dipole interaction and the vertical double arrows denote the Coulomb interaction. The basic configurations which contribute to the transition amplitude resulting from both initial-state configuration interaction (ISCI) and final-state configuration interaction (FISCI) are shown in scheme (33). Electric-dipole interaction between the states in the braces is neglected. The correlations (33a) and (33d) describe the intershell interaction, and the correlation (33f) is responsible for

autoionization of the resonances. The total and intermediate momenta of all states are omitted in scheme (33) to simplify the notation.

The correlations (33a,b,d,e) were taken into account by second-order perturbation theory where a summation/integration over all states contained in the braces was performed (continuum states were taken into account in a quasi-discrete manner). The correlation (33c), when computed within perturbation theory, contains divergent continuum–continuum integrals, and it was, therefore, included by computing the correlational function [297] (following the procedure described in [259, 260, 287]). The reduction coefficients of the Slater integrals entering scheme (33) were not averaged as in the calculation of the core polarization potential (31), but computed for each integral (see, e.g., [73, 74]). We emphasize that the channels included in scheme (33) were excluded from the calculation of $V_\ell^{\rm CP}(r)$ (31). The correlation (33f) was taken into account by including the interaction between many resonances and many continua, as described below.

The total photoionization cross section for the initial state $|i_0(2\mathrm{p}_x)\rangle \equiv \left|2\mathrm{p}^5{}_{J_0^+}3\mathrm{p}[K_0]_{J_0}\right\rangle$, leading to $\mathrm{Rg}^+(^2\mathrm{P}_{J^+})$ ions, is given by

$$\sigma_{J^+}(i_0,\omega) = \sum_{\ell j J} \sigma_{J^+\ell j J}(i_0,\omega). \tag{34}$$

The partial cross sections $\sigma_{J^+\ell j J}(i_0,\omega)$ describing the contribution of the $|2\mathrm{p}^5{}_{J^+}\varepsilon\ell_j J\rangle \equiv |J^+\ell j J E\rangle$ channel to $\sigma_{J^+}(i_0,\omega)$ are

$$\sigma_{J^+\ell j J}(i_0,\omega) = \left| d_{J^+\ell j J}(i_0,\omega) + \sum_i \frac{\left\langle J^+\ell j J E \left|\mathbf{H}^{\rm ee}\right| \bar{i}\right\rangle}{E-E^{(i)}} D^{(i)}(i_0,\omega) \right|^2, \tag{35}$$

where $\left|\bar{i}\right\rangle$ is determined below (see equation (39)).

The transition amplitudes entering equation (35) are determined using the matrix elements of the electric-dipole operator $\mathbf{D}$:

$$d_{J^+\ell j J}(i_0,\omega) = \left[\frac{4\pi^2\alpha a_0^2\omega^{\pm1}}{3(2J_0+1)}\right]^{1/2} \left\langle J^+\ell j J E \left|\mathbf{D}\right| i_0\right\rangle, \tag{36}$$

$$D^{(i)}(i_0,\omega) = \left[\frac{4\pi^2\alpha a_0^2\omega^{\pm1}}{3(2J_0+1)}\right]^{1/2} \left(\left\langle \bar{i}^* \left|\mathbf{D}\right| i_0\right\rangle + \right. \tag{37}$$
$$\left. + \sum_{J^+\ell j J} \int \mathrm{d}E' \frac{\left\langle \bar{i}^* \left|\mathbf{H}^{\rm ee}\right| J^+\ell j J E'\right\rangle \left\langle J^+\ell j J E' \left|\mathbf{D}\right| i_0\right\rangle}{E-E'+\mathrm{i}\delta} \right),$$

where the signs (+) and (−) correspond to the length and velocity forms of operator $\mathbf{D}$, respectively; ω denotes the exciting photon energy in atomic units; $\alpha = 1/137.036$ is

the fine-structure constant; the square of the Bohr radius $a_0^2 = 28.0028$ Mb can be used to convert atomic units for cross sections to Mb. The exciting photon energy ω and the Rydberg electron/ photoelectron energy E, with respect to the $2p^5(^2P_{1/2})$ threshold $E_{1/2}$, are related via

$$E(2p_x) + \omega = E_{1/2} + E \tag{38}$$

where $E(2p_x)$ is the energy of the initial $2p^5 3p\,(2p_x)$ atomic level.

The continuum wave functions $|J^+ \ell j J E\rangle$ entering equations (35–37) satisfy the incoming-wave condition and were computed by applying the K-matrix technique [299]. The complex energies of the resonances $E^{(i)}$ and their functions

$$\left|\bar{i}\right\rangle = \sum_m b_m^{(i)} |m\rangle \equiv \left\langle \bar{i}^* \right| \tag{39}$$

were obtained as the solution of the secular equation with a complex symmetric (and therefore nonhermitian) matrix:

$$\sum_m \left[\left(E^{(i)} - E_m\right) \delta_{mm'} - \langle m \left|\mathbf{H}^{\rm ee}\right| m' \rangle - \sum_\beta \int \mathrm{d}E' \frac{\langle m \left|\mathbf{H}^{\rm ee}\right| \beta E' \rangle \langle \beta E' \left|\mathbf{H}^{\rm ee}\right| m' \rangle}{E - E' + \mathrm{i}\delta} \right] b_m^{(\mathrm{i})} = 0, \tag{40}$$

where $b_m^{(i)}$ are complex numbers, $|m\rangle$ is the single-configuration wave function of the discrete state in PF approximation (e.g., $2p^5{}_{1/2}12d'[3/2]_2$), and $|\beta E'\rangle \equiv |J^+ \ell j J E'\rangle$. The complex energy of each resonance determines its position E_i and width Γ_i via the relation

$$E^{(i)} = E_i - \frac{\mathrm{i}}{2}\Gamma_i. \tag{41}$$

E_i and Γ_i are related to the quantum defects μ and the reduced widths $\Gamma_{\rm r}$, which only weakly depend on the principal quantum number n, via equations (8) and (10). The transition amplitudes (37), evaluated at the resonance energy, allow us to compute the lineshape parameters q_i and $\sigma_0\rho_i^2$ for the resonance i:

$$q_i(i_0) = -\frac{\mathrm{Re}D^{(i)}(i_0)}{\mathrm{Im}D^{(i)}(i_0)}, \qquad \sigma_0\rho_i^2(i_0) = \frac{2[\mathrm{Im}D^{(i)}(i_0)]^2}{\pi\Gamma_i}, \tag{42}$$

where $q_i(i_0)$ is the usual Fano lineshape parameter or profile index [6,7]. The parameters q_i, $\sigma_0\rho_i^2$ and σ_0 determine the lineshape of the ARS via the equation

$$\sigma_{3/2}(i_0, \omega) = \sum_i \sigma_0\rho_i^2(i_0) \left[\frac{\left(q_i(i_0) + \epsilon_i\right)^2}{1 + \epsilon_i^2} - 1 \right] + \sigma_0 \tag{43}$$

which was recently used for the parameterization of computed lineshapes, e.g. in [34, 73, 300]. The background cross section σ_0 includes the tails of adjacent resonances and is obtained by removing the parameterized resonances from the range of interest. The parameter σ_0 in (43) is always positive as explained in [8, 9, 301].

4. General trends for the reduced widths and energies of the autoionizing Rg $(mp^5(^2P_{1/2})n\ell'[K']_J)$ resonances of the rare-gas atoms Rg = Ne–Xe

4.1. Qualitative behaviour and scaling laws

The spectra of ARS exhibit a regular structure and systematic trends similar to those of bound Rydberg states (see, e.g. [1, 202, 302]). Although there are no strict rules for the dependence of the spectra on the quantum numbers n, ℓ', K' and J, the observed scalings and propensities can be understood by analyzing the dynamical (integrals over the radial variables) and geometrical (integrals over the angular variables) contributions to the matrix elements of the photoexcitation and the Coulombic decay of the ARS (the radiative decay of ARS is generally much slower than autoionization).

4.1.1. Dependence of the ARS spectra on the principal quantum number n. A typical autoionization spectrum consists of well resolved lines in which the series members $n\ell'[K']_J$ with the same set of quantum numbers ℓ', K' and J have similar lineshapes and n-dependent linewidths Γ_n which scale as $(n^*)^{-3}$ ($n^* = n - \mu$). This behaviour is illustrated by the high-resolution photoabsorption spectrum of ground-state Xe atoms [15], which exhibits 'sharp' near-Lorentzian ns' $J = 1$ and 'diffuse' asymmetric nd' $J = 1$ resonances (see figure 6). For Lorentzian lines, the peak cross section σ_n^{P} is connected with the excitation oscillator strength f_n and the width by [303] (all quantum numbers apart from n are omitted for simplicity)

$$\sigma_n^{\mathrm{P}} = \frac{2}{\pi\Gamma_n} 2\pi^2 \alpha a_0^2 f_n \tag{44}$$

where α and a_0 denote the fine-structure constant and the Bohr radius, respectively; in (44) and subsequent equations of section 4.1, energies are given in atomic units E_{h} ($E_{\mathrm{h}} = 1$ Hartree $= 27.2114$ eV). The oscillator strengths for the $i_0 \to n\ell'[K']_J$ transition is given by [304]:

$$f_n \equiv f_{i_0}^{n\ell' K' J} = \frac{2\omega^{\pm 1}}{3g_0} \left| D^{(n\ell' K' J)}(i_0) \right|^2 \tag{45}$$

where g_0 is the statistical weight of the initial state i_0 and other designations are the same as in equation (37). Expressing the electric-dipole-transition moment in Racah

coupling [305] leads to propensity rules for the oscillator strengths with respect to the quantum numbers ℓ, K, and J of the involved states.

The width of the ARS is determined by:

$$\mathit{\Gamma}_n \equiv \mathit{\Gamma}\left(n\ell'[K']_J\right) = \sum_{\ell,K} \mathit{\Gamma}^{\varepsilon\ell K}_{n\ell'K'J} \ . \tag{46}$$

The partial widths are given by the matrix element of the Coulomb operator $\mathbf{H}^{\mathrm{ee}}$

$$\mathit{\Gamma}^{\varepsilon\ell K}_{n\ell'K'J} = 2\pi \left|\left\langle m\mathrm{p}^5_{3/2}\varepsilon\ell[K]_J \left|\mathbf{H}^{\mathrm{ee}}\right| m\mathrm{p}^5_{1/2}n\ell'[K']_J\right\rangle\right|^2 \tag{47}$$

and are represented by a sum which contains direct (F^k) and exchange (G^k) Slater integrals as follows:

$$\begin{aligned}&\left\langle m\mathrm{p}^5_{3/2}\varepsilon\ell[K]_J\right| \mathbf{H}^{\mathrm{ee}} \left|m\mathrm{p}^5_{1/2}n\ell'[K']_J\right\rangle = \\ &\sum_k \Big[\delta(K,K') f_k\left(\ell K,\ell'K'\right) F^k(m\mathrm{p}\varepsilon\ell, m\mathrm{p}n\ell') \ + g_k\left(\ell K,\ell'K'J\right) G^k(m\mathrm{p}\varepsilon\ell, n\ell' m\mathrm{p})\Big] .\end{aligned} \tag{48}$$

Unlike the geometrical factors $f_k\left(\ell K,\ell'K'\right)$ associated with the direct integrals, the factors $g_k\left(\ell K,\ell'K'J\right)$ of the exchange integrals depend on J.

The scalings of the width $\mathit{\Gamma}_n$ and the oscillator strength f_n with the principal quantum number n follow from the n dependence of the ARS orbitals at small distances r. In this region the orbital $P_{n\ell'}(r)$ for a hydrogen-like Rydberg state with nuclear charge Z can be approximated by [250]:

$$P_{n\ell'}(r) \approx 2\left(\frac{Z}{n}\right)^{\frac{3}{2}} \frac{(2Zr)^{\ell'}}{(2\ell'+1)!} r \left(1 - \frac{2Zr}{2\ell'+2} + \frac{(2Zr)^2}{(2\ell'+2)(2\ell'+3)\cdot 2!} - \ldots\right). \tag{49}$$

Because of the normalization factor $(Z/n)^{3/2}$, the width $\mathit{\Gamma}_n$ and the oscillator strength f_n, which are both proportional to the square of the ARS wavefunction, scale as n^{-3}. For Rydberg states with nonzero quantum defect, the factor $n^{-3/2}$ is replaced by $(n-\mu)^{-3/2} \equiv (n^*)^{-3/2}$ [214, 222]. Correspondingly, each ARS series $n\ell'[K']_J$ can be characterized by an n-independent reduced width $\mathit{\Gamma}_{\mathrm{r}} = (n^*)^3\mathit{\Gamma}_n$ (see equation (10)) so that the peak cross section σ^{P}_n is expected to be independent of n. At low n, a residual n dependence (i.e., energy dependence) of σ^{P}_n and $\mathit{\Gamma}_{\mathrm{r}}$ may occur (see below).

In experiments carried out with an energy bandwidth ΔE_{exp}, the observed spectra represent the convolution of the ARS lineshape function with the experimental function. An essentially flat continuum results as soon as the energy separation between neighbouring ARS $\mathrm{d}E_n/\mathrm{d}n = 1/\left(n-\mu\right)^3$ becomes smaller than ΔE_{exp}. This resulting

pseudo-continuum goes over smoothly into the ionization continuum (see figure 6) for which the cross section σ_c is given by [306]

$$\sigma_c = 2\pi^2 \alpha a_0^2 \, (\mathrm{d}f/\mathrm{d}E) \, . \tag{50}$$

In the discrete region, the corresponding expression for the averaged values of the cross section over the energy interval between adjacent Rydberg levels is

$$\sigma_n = 2\pi^2 \alpha a_0^2 f_n / \left(\mathrm{d}E_n/\mathrm{d}n\right) = 2\pi^2 \alpha a_0^2 f_n \cdot (n-\mu)^3 \, , \tag{51}$$

which is independent of n just as σ_n^{P} is (see equation (44)). With equations (10), (44), and (51) one obtains for the cross section ratio $\sigma_n^{\mathrm{P}}/\sigma_n$ the expression

$$\frac{\sigma_n^{\mathrm{P}}}{\sigma_n} = \frac{2}{\pi \Gamma_{\mathrm{r}}}, \tag{52}$$

which is normally much larger than unity. If one takes the experimental bandwidth into account, the peak intensity of the autoionizing lines, which should be constant for infinitely narrow bandwidth according to (51), starts decreasing with n as soon as the autoionization width becomes narrower than the experimental bandwidth. This effect is clearly seen in the autoionizing s series ($J = 1$) of Xe displayed in figure 6, the peak intensities of which decrease with increasing n value.

At lower n, the reduced widths Γ_{r} are often found to exhibit a residual variation with n, because the energy separation between adjacent n is substantial. For the rare gases Ne – Xe, these effects are most significant for Kr and Xe because of the large spin–orbit splitting of their ionic cores. Correspondingly, the kinetic energy of the continuum electron resulting in the autoionization process varies by several tenths of an eV from the lowest possible n up to the high-n region. The residual n dependence of Γ_{r} has been quantified for ARS of Xe by CIPFCP calculations [48], and variations of up to a factor of two have been found. These n dependencies of Γ_{r} have no simple explanation because they arise from several competing effects which may yield either increasing or decreasing reduced widths with rising n.

4.1.2. Dependence of the resonance width on the orbital quantum number ℓ'. The dependence of the autoionization width on the orbital quantum number ℓ' of the ARS is complex because the matrix element (48) contains direct and exchange integrals and equation (46) involves a summation over K and ℓ. Petrov *et al* [76] studied the ℓ' dependence of the width for the $m\mathrm{p}^5_{1/2} n\ell' - m\mathrm{p}^5_{3/2}\varepsilon\ell$ autoionization process within the PF approach. Because of the strong delocalization of the Rydberg electron, the exchange

integrals G^k are small compared with the direct integrals F^k. When the exchange integrals are neglected in (48), only the $F^{k=2}$ integrals contribute significantly (the series $ns'[1/2]_1$ represents an exception: the partial width $\Gamma^{\varepsilon s[3/2]}_{ns'[1/2]1}$, which provides an important contribution to the total width, especially for Ne, contains only the exchange integral). As a consequence only partial widths $\Gamma^{\varepsilon\ell K}_{n\ell' K' J}$ remain which are independent of J and obey $K = K'$:

$$\Gamma^{\varepsilon(\ell'-2)[\ell'-1/2]}_{n\ell'[\ell'-1/2]J} = 2\pi \frac{3\,(\ell'-1)}{25(2\ell'-1)} \left(F^2(m\mathrm{p}n\ell'; m\mathrm{p}\varepsilon(\ell'-2))\right)^2 \tag{53}$$

$$\Gamma^{\varepsilon\ell'[\ell'-1/2]}_{n\ell'[\ell'-1/2]J} = 2\pi \frac{\ell'+1}{25(2\ell'-1)} \left(F^2(m\mathrm{p}n\ell'; m\mathrm{p}\varepsilon\ell')\right)^2 \tag{54}$$

$$\Gamma^{\varepsilon\ell'[\ell'+1/2]}_{n\ell'[\ell'+1/2]J} = 2\pi \frac{\ell'}{25(2\ell'+3)} \left(F^2(m\mathrm{p}n\ell'; m\mathrm{p}\varepsilon\ell')\right)^2 \tag{55}$$

$$\Gamma^{\varepsilon(\ell'+2)[\ell'+1/2]}_{n\ell'[\ell'+1/2]J} = 2\pi \frac{3\,(\ell'+2)}{25(2\ell'+3)} \left(F^2(m\mathrm{p}n\ell'; m\mathrm{p}\varepsilon(\ell'+2))\right)^2 \tag{56}$$

The decay (53) associated with a decrease of the orbital angular momentum $\ell' \to \ell' - 2$ is always small compared with the ℓ'-conserving decays (54, 55). The latter decays also prevail over the $\ell' \to \ell' + 2$ process (56) for $\ell' \leq 6$ if the energy of the continuum electron is small. This is true for Ne and Ar; for Kr and Xe, however, the ℓ'-conserving decay dominates only for $\ell' \leq 3$.

When ℓ' is conserved, one can apply the Coulomb–Bethe approximation (see also [202])

$$F^k(m\mathrm{p}n\ell'; m\mathrm{p}n\ell') = \left\langle r^k_{m\mathrm{p}} \right\rangle \left\langle \frac{1}{r^{k+1}_{n\ell'}} \right\rangle \tag{57}$$

to estimate the $F^2(m\mathrm{p}n\ell'; m\mathrm{p}\varepsilon\ell')$ integral. Using the hydrogenic expression for $\left\langle r^{-3}_{n\ell'} \right\rangle$ [307] the integral scales as ℓ'^{-3} and the partial width as ℓ'^{-6}.

With increasing ℓ' and atomic number Z, the $\ell' \to \ell' + 2$ processes begin to play a significant role, and the ℓ' dependence of the width has to be evaluated numerically. Calculations performed for Ne – Xe within the PF approximation [76] yielded $\ell'^{-6} - \ell'^{-9}$ scalings of the width for $K' = \ell' - 1/2$ and $\ell'^{-4} - \ell'^{-5}$ scalings for $K' = \ell' + 1/2$. We note that in the decay processes (53)–(56) the core configuration does not change, only its total angular momentum. For the case of doubly excited ARS (such as $\mathrm{Ba}(6\mathrm{p}_{1/2}n\ell)$) autoionization is mediated by an ℓ change of the inner electron (here 6p to 6s or 5d), and the corresponding dependence of the width on ℓ was found to be very steep with scalings in the range ℓ^{-9} to ℓ^{-12} for $\ell = 4 - 8$ and $n = 11 - 13$ [308].

4.1.3. Dependence of the resonance width on the quantum numbers K' and J. The dependence of the reduced width $\Gamma_{\rm r}$ on the quantum number $K' = \ell' \pm 1/2$ is determined by (i) the ratio of the geometrical factors preceding the integrals F^2 in equations (53)–(56) and (ii) the interplay between the $n\ell' \rightarrow \varepsilon\ell'$ and $n\ell' \rightarrow \varepsilon(\ell'+2)$ channels. In Ne and Ar the energy of the continuum electron is small, and the ratio between the geometrical factors in the two dominant partial widths for $K' = \ell' - 1/2$ and $K' = \ell' + 1/2$ (equations (54) and (55)) amount to 10, 3.5, 2.4, and 2.0 for $\ell' = 1-4$, respectively, i. e. the reduced width is larger for $K' = \ell' - 1/2$ than for $K' = \ell' + 1/2$. These propensities are reflected in the experimental and theoretical reduced widths listed in tables 4(a,b) (especially for $J = \ell'$). For Kr and Xe, the energy of the continuum electron is significantly larger and the $n\ell' \rightarrow \varepsilon(\ell' + 2)$ decay becomes as rapid (at $\ell' \simeq 4$) or even more rapid ($\ell' \geq 5$) than the $n\ell' \rightarrow \varepsilon\ell'$ decay. As a consequence the reduced widths $\Gamma_{\rm r}[K' = \ell' + 1/2]$ become larger than $\Gamma_{\rm r}[K' = \ell' - 1/2]$ (see tables 4(c,d)). This prediction has yet to be confirmed experimentally.

The dependence of the reduced width on the total angular momentum J is determined by (i) the presence of the exchange integral in equation (48) and (ii) the term dependence of the AO describing the Rydberg electron. The influence of (i) is relatively small whereas the term dependence of the AOs can substantially change the reduced widths, especially for small orbital angular momentum ℓ', for which the Rydberg electron penetrates into the core. For AOs with $J = \ell' - 1$, the term dependence is usually larger than for those with $J = \ell'$. In tables 4(a–d), one observes that for $K' = \ell' - 1/2$ the reduced widths can differ by a factor of up to two.

The major factors determining the general trends in the behaviour of the autoionization widths can be summarized as follows: (i) the normalization of the Rydberg AOs results in the $(n^*)^{-3}$ dependence of Γ_n, allowing one to introduce the reduced widths $\Gamma_{\rm r}$ (10) which are (almost) independent of n; (ii) the strong delocalization of the Rydberg AOs results in steep ($\ell'^{-4} - \ell'^{-9}$) dependencies of $\Gamma_{\rm r}$ on the orbital quantum number where the power of ℓ' depends on the interplay between the $n\ell' \rightarrow \varepsilon\ell'$ and $n\ell' \rightarrow \varepsilon(\ell' + 2)$ decay channels; (iii) for small ℓ' ($\ell' \leq 2$), ARS with $K' = \ell' - 1/2$ are substantially broader than ARS with $K' = \ell' + 1/2$ because of the dominant role of the $n\ell' \rightarrow \varepsilon\ell'$ decay channel and the associated geometrical factors; for large ℓ' this trend is reversed for Kr and Xe because of the dominant role of the $n\ell' \rightarrow \varepsilon(\ell' + 2)$ decay channel for larger continuum electron energy; (iv) the term dependence of the Rydberg AOs results in a significant dependence of the reduced widths on the total angular momentum J for $K' = \ell' - 1/2$ ($J = \ell' - 1, \ell'$); the contribution of the exchange

integrals to the dependence of $\Gamma_{\rm r}$ on J is comparatively small, except for the Ne ns′ resonances.

The single-electron PF approximation provides an understanding of the general trends in the dependence of the reduced width on the ARS quantum numbers n, ℓ', K', and J. In order to obtain a quantitative description of the autoionization dynamics, many-electron effects have be taken into account. The most general effects influencing the autoionization rate are core polarization, which can change (usually increase) $\Gamma_{\rm r}$ by up to a factor of three [33, 34, 48, 77], and the correlational decrease of the effective Coulomb interaction which usually compensates to some extent the influence of the core polarization [48, 77]. Another many-electron effect influencing the reduced widths is the mixing of autoionizing resonances of the same parity and total angular momentum. Mixing of ARS series can be substantial if the quantum defects (modulo one) for different channels have similar values (as for the ns′$[1/2]_1$ and nd′$[3/2]_1$ resonances in Ar [77]), or when the widths of ARS belonging to the same series are comparable with their separation (as in the case of the nd′$[3/2]_1$ resonances in Xe [48]).

4.2. Experimental observations and comparison with theory

In this section, we discuss the trends observed experimentally and present selected ARS spectra from which the recommended experimental resonance parameters in table 4 were obtained. We include only results obtained with a photon bandwidth smaller than the natural ARS width and not broadened by saturation effects. The recommended reduced widths and energies of the ARS are compared with the results of the CIPFCP calculations. To indicate the effects of electron correlations and core polarization, we also list the reduced widths and quantum defects calculated within the Pauli–Fock approximation for $n = 20$ [76].

4.2.1. Odd-parity resonances (ns′, nd′, ng′). The odd-parity ARS in Ne ($n \geq 12$) are very narrow (< 0.2 cm^{-1}), and until recently monochromatized synchrotron radiation (bandwidth down to 1.5 cm^{-1}) [99] was broader than the respective natural width. A comprehensive high-resolution study, using two-step two-color cw laser excitation of metastable Ne (3s $J = 2, 0$) atoms in a collimated atomic beam via several 3p $J = 1, 2$ levels provided benchmark data for the ns′ $J = 0, 1$ ARS [36–38, 40] and for the four nd′$[3/2]_{1,2}$ nd′$[5/2]_{2,3}$ ARS [36, 41, 42] of Ne. Similar results were obtained for the ns′ [40] and nd′ ARS [41, 45, 47, 48] of Ar, Kr, and Xe. We also mention the contributions provided by optogalvanic spectroscopy [47–50], including the high-resolution work on

Ar(ns') over the range $n = 11-25$ [43] which nicely demonstrated the $(n^*)^{-3}$ dependence of the widths.

The observations for the ns' $J = 0, 1$ resonances are summarized in figure 7, using a reduced energy scale (multiplication with $(n^*)^3$ to allow a direct comparison of resonances with different n^*). The reduced width of the Rg $(ns'[1/2]_0)$ ARS provides accurate information on s–d mixing since this resonance can only decay to the $Rg^+(^2P_{3/2}) + e^-(\varepsilon d_{3/2})$ continuum [38, 40, 230]. The $ns'[1/2]_1$ ARS can also decay to εs continuum states. To first order in the Coulomb interaction, this coupling is mediated by electron exchange which is found to provide the dominant contribution to the width [40] for Ne. This explains why the Ne $(ns'J = 1)$ ARS are three times broader than the Ne $(ns'J = 0)$ ARS. In contrast, the ns' $J = 1$ resonances in Ar, Kr, and Xe are *narrower* than the ns' $J = 0$ ARS [40, 43]. This finding was explained by a combination of several effects [40]: (i) the exchange matrix element describing the decay to the εs continuum rises by a factor of only 1.5 from Ne to Xe; (ii) the direct Coulomb matrix element corresponding to the s–d decay strongly increases by factors between 4 and 7 from Ne to (Ar, Kr, Xe) for both $J = 0$ and 1; (iii) in the coupling of the $ns'J = 1$ ARS to the εd continua, the contributions from the direct matrix element, the two exchange matrix elements and higher order terms interfere destructively. The qualitative trends in the variation of the ns' resonance widths with J and with atomic number (also the respective maximum for Kr, see table 4) are already reproduced in the first-order Pauli–Fock calculations involving a relaxed ion core.

For Ne, the nd/εd wave functions do not have a significant overlap with the $2p^5$ core, and therefore the nd' resonances in Ne are narrow. Their widths are well reproduced in the Pauli–Fock approximation if a relaxed ion core is used. Early *ab initio* calculations on the ns', nd' $J = 1$ widths of Ne [65, 68] involved a nonrelaxed core, which prevented a close agreement with experimental results. The nd' resonances of Ar, Kr, and Xe are much broader than those of Ne. It is difficult to obtain accurate theoretical predictions for their widths, especially for the $nd'[3/2]_1$ series, because the d wave functions in Ar, Kr, and Xe are particularly sensitive to details of the interactions in the proximity of the d-orbital collapse [252]; moreover, the $nd'[3/2]_1$ ARS interact with the $ns'[1/2]_1$ series.

Spectra of the four narrow Ne (nd') resonances have been measured following single-mode cw-laser excitation from several intermediate Ne $(3p$ $J = 1, 2)$ levels, accessed from the metastable Ne $(3s\ ^2P_2)$ level [42], see also figure 3. In figures 8 and 9, we summarize the key results for the intermediate levels (a) $3p'[1/2]_1$ (Paschen notation $2p_2$), (b) $3p'[3/2]_1$ ($2p_5$), and (c) $3p[5/2]_2$ ($2p_8$) which yield information on (a) the

nd′[3/2]$_{1,2}$, (b) the nd′[5/2]$_2$, and (c) the nd′[5/2]$_3$ ARS. The measured spectra are fitted by superpositions of Shore profiles, as described in [74] (see also the results of [42] and the recent CIPFCP analyses of the Ne (nd′) spectra for more detailed information [74]). In agreement with MQDT analyses [42] and *ab initio* calculations, the nd′[3/2]$_2$ ARS has the largest reduced width among the four Ne (nd′) series. In contrast, the nd′[3/2]$_1$ series has the largest reduced width in Ar and especially in Kr and Xe. The nd′[3/2]$_1$ resonances are in fact the broadest of all ARS (see table 4) and have been studied for a long time by VUV excitation from the ground state [1, 14, 15, 19, 20]. Similar to the situation encountered in Ne, the nd′ $J = 2, 3$ resonances of Ar, Kr, and Xe overlap energetically, and the determination of their widths requires special care. By selecting (similar to the procedure adopted for Ne) an excitation path via a suitable intermediate $(m+1)$p$[K]_J$ level in combination with an appropriate choice of the polarizations of the two light fields, it is possible to strongly enhance the intensity of the nd′$[K']_J$ resonance of interest [45, 47–50, 132]. Propensity rules for the excitation strengths in Racah coupling [305] are helpful for the selection of the intermediate level.

Experimental information on the ng′ resonances is sparse. Three-photon excitation experiments of ground state atoms provided upper limits for the reduced widths of the ng′ $J = 1, 3$ resonances [53]. Up to now, the only accurate data were obtained for the 11g′[7/2]$_3$ [41] and the 9g′[7/2]$_4$ resonance [46] of Ar which possess reduced widths of 26.9(6) cm^{-1} and 27.7(14) cm^{-1}, respectively. The latter resonance, recorded using the excitation sequence Ar (4s[3/2]$_2 \rightarrow$ 4p[5/2]$_3 \rightarrow$ 9g′[7/2]$_4$), is shown in figure 10; the smooth curve is the result of a fit to the experimental data with a Fano profile (resonance width 0.038(2) cm^{-1}).

4.2.2. Even-parity resonances (np′, nf′). Information on the np′,nf′ ARS of Ne–Xe was obtained by (i) one-photon excitation of the metastable levels [25, 26, 30, 32–34], (ii) two-step two-photon excitation from the ground state via odd-parity $J = 1$ intermediate levels [34, 56, 58, 60, 62, 64, 309, 310], and (iii) four-photon excitation from the ground state [55].

The np′[1/2]$_{0,1}$ resonances are special in the sense that their reduced widths are similar (around 3000 cm^{-1} to within a factor of two) for all the heavier rare gases, including Ne. In contrast, the np′[3/2]$_{1,2}$ ARS have smaller reduced widths which increase from around 300 cm^{-1} for Ne to around 1000 cm^{-1} for Xe. The combined evaluation of np′ spectra, excited from each of the two metastable levels in Ne [33] and Ar [300], allowed the characterization of their overlapping np′[1/2]$_1$, [3/2]$_1$, [3/2]$_2$

resonances. In both cases, CIPFCP calculations were helpful in the analysis and interpretation of the experimental results. As examples, we compare in figures 11 and 12 the experimental and theoretical results obtained by [33] for the Ne (13p′) resonances, excited from the two metastable levels. As predicted by theory, the broad $13p'[1/2]_1$ resonance is essentially absent in the spectrum excited from the Ne ($3s'\ ^3P_0$) level whereas the narrow $13p'[3/2]_1$ is weak when excited from Ne ($3s\ ^3P_2$). The absolute cross-section scale is provided by the calculations and has an uncertainty of about 20%. To assign and simplify the np' spectra accessed from the ground state via low-lying odd-parity $J = 1$ levels, their polarization dependence (see equation (5)) was exploited in Ne [62], Ar [60,64], and Xe [59]. As illustration, we present in figure 13 the (13,14)p′, 12f′ spectra, obtained via (a) the intermediate Ne ($3s[3/2]_1$) level and (b) via the Ne ($3s'[1/2]_1$) level with parallel electric-field vectors of the two light fields, thus excluding excitation of $J = 1$ resonances. The spectra yielded accurate widths and quantum defects for the $np'[1/2]_0$ and $np'[3/2]_2$ series. The very sharp $nf'[5/2]_2$ resonances (predicted reduced width 20.3 cm^{-1}), however, have natural widths much narrower than the experimental bandwidth (see below). The shapes and intensities of the resonances are found to strongly depend on the intermediate level, as discussed in [62]; see also section 5.2.

The nf' resonances are strong in spectra excited from intermediate levels with an outer d electron. The propensity rules clearly favour nf' excitation over np' excitation, see e.g. [58,60,64]. As an example, we show in figure 14 the Xe $4f'[5/2]_2$ ARS spectrum, obtained by laser excitation of the Xe ($5d[3/2]_1$) level, populated from the ground state by monochromatized synchrotron radiation [56, 58]. The absolute cross-section scale is provided by the CIPFCP calculation within an uncertainty of about 20% [58]. The experimental and calculated lineshape parameters and the resonance widths are found to agree to within 10% and 20%, respectively [58]. The reduced widths of the $nf'[5/2]_2$ ARS in Ar [64] and Kr [34] have also been determined by excitation from an intermediate $J = 1$ level with odd parity. The widths of the $nf'[5/2]_3$ ARS in Ar [34] and Xe [26, 34] were obtained from spectra excited from the respective metastable $J = 2$ level. Some of the very sharp nf' resonances in Ne (predicted width of the $12f'[5/2]_{2,3}$ resonances 0.0135 cm^{-1}, see table 4) have been observed [62,309,311], see also diagram (a) in figure 13, but a measurement of their widths requires a photon bandwidth well below 0.01 cm^{-1} (300 MHz) and so far has not been carried out. Likewise, experimental information on the widths of the $nf'[7/2]_{3,4}$ ARS (except for Xe) and of the nh' ARS is not available up to now. Using optogalvanic spectroscopy involving the collisionally excited $nd[5/2]_2$ and $nd[7/2]_3$ levels of Xe, Hanif *et al* [32] were able to study the low-lying Xe ($nf'[7/2]_3$)

and Xe $(n\mathrm{f}'[7/2]_4)$ resonances ($n = 4, 5$). Their results for the Xe $(4\mathrm{f}'[7/2]_{3,4})$ resonances (reduced width 250(30) cm^{-1} in both cases) are presented in figure 15.

A comparison of the experimentally and theoretically (obtained with the CIPFCP method) determined reduced widths shows that, in the majority of cases, the theoretical predictions agree with the experimental values to within about 20%. In some cases, the deviations are substantially larger (especially for Ar $(n\mathrm{d}'[3/2]_1)$). The calculated quantum defects are in semi-quantitative agreement with the measured values; in most cases, calculations predict the correct energy ordering for the various $n\ell'[K']_J$ resonances with the same ℓ' value, and are helpful to assign the experimental spectra.

5. Photoionization dynamics of excited rare-gas atoms near threshold

5.1. Alkali-atom-like behaviour of the continuum photoionization cross sections for excited Rg (mp^5(m+1)s, (m+1)p) atoms (Rg = Ne–Xe; $m = 2 - 5$)

The binding energies and atomic orbitals of the outer $(m+1)\ell$ electrons in the excited rare-gas atoms Ne–Xe are similar to those of the outer $(m+1)\ell$ electrons in the corresponding alkali-metal atoms Ak (mp^6 (m+1)ℓ) (Ak = Na–Cs, $m = 2-5$) [312]. Thus one expects that—apart from effects associated with the reduced nuclear charge and the open-shell core of the respective rare-gas atoms—the near-threshold photoionization cross sections of the $(m+1)\ell$ electrons in the rare-gas atoms should be similar in size and energy dependence to those of the $(m+1)\ell$ electrons in the alkali-metal atoms. In this section, we only discuss results which do not consider the autoionizing resonances occurring between the $^2\mathrm{P}_{3/2}$ and $^2\mathrm{P}_{1/2}$ ionization thresholds of the rare gases.

Photoionization cross sections of one-electron atoms and ions decrease monotonically above threshold for all $n\ell$ states [250]. This behaviour also holds for the photoionization cross sections of excited orbitals in many-electron systems as long as they do not overlap with the ion core (typically for $\ell > 3$). For excited heavier alkali-like atoms and ions with $\ell = 1 - 3$, the photoionization cross sections of the outer electron near threshold normally decrease with rising energy, but they exhibit more or less nonhydrogenic behaviour, including minima in partial cross sections [313–316] the n and ℓ dependence of which has been discussed, e.g., in [257, 287, 288, 317–320].

The deviation from hydrogenic behaviour is most striking for ns states which exhibit a zero in the s→p dipole matrix element near threshold and thus a zero in the cross section [313, 314], which is referred to as a Seaton–Cooper minimum. When the effects of spin–orbit interaction on the p wave are included [306, 314], the slightly

different energies at which the zero of the electric-dipole-transition matrix elements to the outgoing $p_{3/2}$ and $p_{1/2}$ waves occur prevent the cross section from exactly returning to zero at the positions of the minima. Calculated cross sections for the alkali-metal atom $(m+1)$s ground state ($m = 2-5$) and the associated photoelectron angular distribution parameters β are summarized in figure 16. They were obtained in CIPF and CIPFCP calculations [72] and are compared with selected experimental data [294, 321–323]. The position and depth of the Seaton–Cooper minimum as well as the deviation of the β parameter from 2 result from relativistic effects on the outgoing p-wave and from electron correlation effects and they strongly depend on the approximations made in the theoretical treatments (see [72, 324, 325] for more details and further references).

The expected similarity between the photoionization cross sections for the outer $(m+1)\ell$ electrons in excited rare-gas atoms with those in the respective alkali atoms has been reproduced in calculations of excited states with $\ell = 0$ [261, 262, 326–330], $\ell = 1$ [261, 296, 326, 331–333], and $\ell = 2$ [261]. In many of these calculations, however, electron correlation, relativistic effects and the open-shell structure of the rare gas ion core were ignored.

In a single configuration description, photoionization from the metastable $(m+1)$s $J = 2$ level ($J^+ = 3/2$ core) and from the $(m+1)$s $J = 0$ level ($J^+ = 1/2$) only involve the respective core-conserving "major" transitions, i.e., those leading to the formation of only $Rg^+\,(^2P_{3/2})$ ions from $J = 2$ and only $Rg^+\,(^2P_{1/2})$ ions from $J = 0$. Correlation effects in the initial and final states, however, modify this simple picture considerably and result in the observation of the core-changing "minor" transitions. For the metastable $J = 0$ level, for example, mixing of the $mp^5(^2P_{1/2})\,(m+1)$s configuration with nearby $mp^5(^2P_{3/2})\,md$ $J = 0$ configurations leads to a substantial or even dominant population of the $Rg^+(^2P_{3/2})$ ion channel [69–71], the clearest example being observed in the photoionization from the Xe (6s′ $J=0$) level [70] (see below).

The first initial- and final-state specific photoionization cross sections for all the metastable $Rg\,(mp^5(m+1)s\,J = 2, 0)$ atoms with correlated wave functions were computed by Petrov *et al* [69–72] with the CIPF and the CIPFCP method. In figures 17, 18, 19, and 20, we show the (partial) cross sections and associated β parameters for photoionization from the metastable $J = 2/J = 0$ levels to the $^2P_{3/2}$ (figures 17, 20) and the $^2P_{1/2}$ (figures 19, 18) ion states. The experimental data were obtained by angle-resolved photoelectron spectrometry using a continuous atomic beam in conjunction with intense cw lasers at a few fixed photon energies and a double-hemispherical condensor [69–71]. Good overall agreement between the computed and measured data

is observed. The 'major' cross sections (figures 17, 18) essentially exhibit alkali-like behaviour with near-threshold values below $0.1 - 0.3$ Mb. The energy dependence of the minor cross sections (figures 19, 20) is very different (mainly decreasing with increasing photoelectron energy) and reflects electron correlation effects in the initial and final states. For $J = 2$, the minor cross sections remain small (below about 0.1 Mb) whereas for $J = 0$ they increase very strongly with increasing atomic number (by a factor of about 400) and reach values around 10 Mb near threshold for Xe $(6s'$ $J = 0)$. This increase can be attributed to the growing importance of initial-state s–d mixing [71] which is illustrated in figure 21. For Xe $(J = 0)$, the wave function can be written to first order as a superposition of similarly strong amplitudes involving the $5p^5(^2P_{1/2})\,6s_{1/2}\,J = 0$ and $5p^5(^2P_{3/2})\,5d_{3/2}\,J = 0$ configurations [31, 70]. The large size of the minor cross section for Xe $(6s\ J = 0)$ mainly results from the d→f amplitude from the latter configuration, which also accounts for the observation that the computed and measured PAD parameters β are close to 0.8, the value predicted for photoionization of a nd electron to the εf continuum (when p wave emission can be neglected) [179]. The εf continuum channel is not accessible in photoionization from the metastable $^3P_0$ level to the $^2P_{1/2}$ ion state because of angular momentum restrictions. Correspondingly, this partial cross section shows a behaviour which is most akin to that observed for the ground state alkali atoms.

In going from the CIPF to the CIPFCP approach, an overall rise of the cross sections is observed. This effect can be attributed to an increased influence of intershell correlations, resulting from the changes in the AOs when core polarization is included. All partial cross sections show a general rise with increasing atomic number due to the substantial increase of the dipole polarizabilities α_d of the atomic cores. Another observation is the shift of the near-threshold features to larger photoelectron energies in a way similar to the case of the alkali atoms. This change originates from the fact that the core polarization potential causes more attraction for the s wave than for the p wave because the s wave has more electron density inside the ionic core. Consequently the effective influence of the core polarization on the cross sections and β parameters corresponds to a net repulsion. Measurements over extended energy ranges are desirable to further test these theoretical predictions.

For excited states with $\ell \geq 1$, the near-threshold cross sections are generally closer to hydrogenic. Here, we only dwell on photoionization from the lowest-lying $(m+1)$p-levels, i.e., the spin–orbit-split doublet states $^2P_{3/2,1/2}$ of alkali-metal atoms and the ten levels of the $mp^5(m+1)p$ configuration ($2p_{1-10}$ in Paschen notation) of the heavier rare-

gas atoms. Most of the previous experimental and theoretical work for photoionization of the $(m+1)$p levels of the alkali-metal atoms has been summarized by Petrov *et al* [334] (and references therein), who compared CIPF and CIPFCP calculations of the total and of the partial s and d wave cross sections. For Na, Rb, and Cs, the $(m+1)$p cross sections decrease monotonically with increasing energy while for K, a local maximum near 0.5 eV photoelectron energy is predicted. For Na, correlation and core polarization are relatively unimportant; for their recent cross sections Miculis and Meyer [284] estimate low uncertainties in the few % range. For K, Rb, and Cs atoms, the inclusion of core polarization leads to a substantial rise in the near-threshold cross sections.

The general behaviour of the photoionization cross sections for the $(m+1)$p orbitals of Ne–Xe in the continuum region above the $^2P_{1/2}$ thresholds follows that of the corresponding $(m+1)$p orbitals in Na–Cs. Earlier calculations [261, 296, 331–333] did not provide information on the cross sections for the two final rare-gas ion states and on the state dependence among the ten-state manifold of the $mp^5(m+1)p$ configuration. A thorough investigation of photoionization from all $2p_{1-10}$ levels of Ne [73,74] and Ar, Kr, and Xe [75] within the CIPFCP approach was recently carried out, both for the energy range of the odd-parity $n\ell'[K']_J$ ($\ell' = 0, 2, 4$) ARS and for the continua located above the $^2P_{1/2}$ threshold. The energy dependence of the total cross sections was found to be compatible with that reported in previous single-electron treatments. Many-electron effects have an important influence on the cross sections for the $mp^5(m+1)p\,2p_{1,5}$ $J = 0$ levels resulting from their interaction with the mp^6 configuration of the ground state. The partial cross sections to the continua associated with the $^2P_{3/2}$ ($\sigma_{3/2}$) and $^2P_{1/2}$ ($\sigma_{1/2}$) levels mainly reflect the admixture of the respective ion core to the composite wave function of the intermediate $2p_x$ level. For the special case of the $mp^5_{3/2}(m+1)p_{3/2}$ $J = 3$ intermediate level, the effects of initial state mixing (only possible through the admixture of *other* higher-lying configurations with even parity) are small, and the partial cross section $\sigma_{1/2}$ mainly reflects electron correlation effects in the *final* state. The probability for the core-changing transition is very low for Ne (3p, $J = 3$) (branching ratio $\sigma_{1/2} : \sigma_{3/2} \leq 0.001$), see [73, 335]. This branching ratio increases substantially towards larger atomic number Z, and its dependence on Z is found to be similar to the Z variation of the reduced autoionization width of the $nd'[5/2]_3$ resonance series [75]. Both predictions agree with experimental observations. For the higher-lying $2p_{1-4}$ levels in Ar, Kr, and Xe (with mainly $J^+ = 1/2$ core) the ionization spectra between the $^2P_{3/2}$ and $^2P_{1/2}$ ionization thresholds are dominated by the $n\ell'$ ($\ell' = 0, 2$) ARS whereas for the

lower-lying levels $2p_{5-10}$ the continuum cross sections are comparable to the resonance contributions [75], as will be discussed in section 5.2.

5.2. Photoionization cross sections in the energy range of the autoionizing rare-gas resonances Rg ($mp^5(^2P_{1/2})n\ell'[K']_J$)

Between the $Rg^+(^2P_{3/2},^2P_{1/2})$ ionization thresholds, the photoabsorption spectra of the rare-gas atoms, both from the ground state (see section 4.1, figure 6) and excited levels (see section 4.2), show prominent structure associated with the $Rg\,(n\ell'[K']_J)$ ARS. In this section, we discuss the main trends observed in these spectra with emphasis on the lineshapes of the ARS which are characterized by the profile index q [6], see equation (3). Here we only include single-photon processes from excited intermediate levels which are either long-lived or have been prepared by resonant one-photon excitation from lower levels (see figures 1 and 2). We omit multiphoton excitation of ARS in strong laser fields with a single tunable laser [51–55, 125]. ARS spectra of Kr and Xe, excited by nonresonant two- and three-photon excitation have been analyzed by MQDT [232]. A theoretical *ab initio* treatment of such experiments requires integration over many continua and is demanding. Another topic which we only mention for completeness concerns the behaviour of ARS in static electric and magnetic fields (for a general discussion see [172, 252]). The influence of the Stark effect on ARS of several rare-gas atoms was investigated in [17, 35, 63].

The ARS lineshapes depend on the oscillator strength of the transitions from the intermediate level $|i\rangle$ to the ARS ($\sim |\langle n\,|\mathbf{D}|\,i\rangle|^2$), on the cross section for direct ionization to the interfering $Rg^+(^2P_{3/2}) + e^-(\varepsilon)$ continuum ($\sim |\langle \varepsilon\,|\mathbf{D}|\,i\rangle|^2$), and on the coupling of the ARS to this continuum V_ε, as seen from the expression [6]

$$q = \frac{\langle n\,|\mathbf{D}|\,i\rangle}{\pi V_\varepsilon\,\langle \varepsilon\,|\mathbf{D}|\,i\rangle}, \tag{58}$$

which is equivalent to equation (42).

Whereas the coupling of the ARS to the continuum is independent of the intermediate level from which the ARS is excited, the oscillator strength and the continuum cross section depend on the character of the intermediate level (especially on its core composition). Thus a particular ARS, accessed from different configurations or even from different levels of the same configuration, in general exhibits different q-parameters. This was demonstrated for the $Ne\,(14s'[1/2]_1)$ resonance, accessed from four different levels of the $Ne\,(2p^5\ 3p)$ configuration [37].

5.2.1. Dependence of the photoionization spectra on the character of the intermediate level. To illustrate the dependence of photoionization spectra on the intermediate level, the computed photoionization spectra for the eight $3p^5 4p[K]_{1,2,3}$ levels of Ar are shown in figure 22. The cross sections for the core-conserving transitions to the continuum $3p^5_{3/2}4p[K]_{1,2,3}(2p_{6-10}) \rightarrow 3p^5_{3/2}\varepsilon\ell(\ell = 0, 2, 4)$ vary in the range 8–15 Mb, whereas the core-changing transitions $3p^5_{1/2}4p'[K']_{1,2}(2p_{2-4}) \rightarrow 3p^5_{3/2}\varepsilon\ell(\ell = 0, 2)$ exhibit smaller values of 2–3 Mb, resulting mainly from the small admixture of the $J^+ = 1/2$ core to the $2p_{2-4}$ levels. The ARS excited from the $2p_{2-4}$ levels have large oscillator strengths, because the core angular momentum is conserved in the process $3p^5_{1/2}4p'[K']_{1,2}(2p_{2-4}) \rightarrow 3p^5_{1/2}n\ell'(\ell = 0, 2)$. The small continuum background associated with core-changing transitions and the large oscillator strengths for core-conserving resonant transitions result in nearly Lorentzian ARS lineshapes in the spectra excited from the $2p_{2-4}$ levels. The oscillator strengths of these resonances follow expectations from propensity rules [305], i.e., the most intense lines in the spectra correspond to transitions in which both K and J rise by one unit, which explains, for instance, the dominance of the $10d'[3/2]_2$, $10d'[5/2]_2$, and $10d'[5/2]_3$ ARS in the photoionization cross sections from the $2p_2$, $2p_3$, and $2p_4$ levels, respectively.

Spectra excited from the $2p_{6-10}$ levels exhibit prominent interference phenomena between strong core-conserving continua and comparatively weak core-changing resonant contributions $3p^5_{3/2}4p[K]_{1,2}(2p_{6-10}) \rightarrow 3p^5_{1/2}n\ell'(\ell = 0, 2)$. These interferences result in lineshapes with q parameters varying over a wide range (Lorentzian-like ($|q| \gtrsim 10$), 'dispersion' ($0.2 \lesssim |q| \lesssim 10$), or 'window' ($|q| \lesssim 0.2$) resonances, see figure 22).

The influence of the spin–orbit splitting of the mp^5 core on the ns', nd' $J = 1$ ARS lineshapes, excited from the $(m+1)p'[1/2]_0$ ($2p_1$) and $(m+1)p[1/2]_0$ ($2p_5$) levels of Ar, Kr, and Xe, is demonstrated in figure 23. The spectra involving the $2p_1$ level have similar Lorentzian-like shapes for Ar, Kr, and Xe. The spectrum for the $2p_5$ level of Ar is similar to that for the $2p_1$ level because of a substantial admixture of the $J^+ = 1/2$ core to the $2p_5$ level. This admixture is much smaller for Kr and Xe, leading to reduced oscillator strength $f^{d',s'}_{(m+1)p}$ and lineshapes with low $|q|$ values. These predictions were confirmed for Xe by measurements of spectra of the ns', nd' $J = 1$ ARS from the $6p[1/2]_0$ and $6p'[1/2]_0$ levels, which were accessed by nonresonant two-photon excitation from the ground state [127].

The spectra depicted in figures 22 and 23 and equivalent spectra for Ne [74], Kr and Xe [75] contain contributions from several ionization channels with partial

cross sections $\sigma_{J^+\ell jJ}(i_0,\omega)$ (35), and it is of interest to decompose the total cross section $\sigma_{J^+}(i_0,\omega) = \sum_J \sigma_{J^+J}(i_0,\omega)$ (34) into J-specific partial cross sections (see, e.g. [34, 59, 73, 75, 132]):

$$\sigma_{J^+J}(i_0,\omega) = \sum_{\ell j} \sigma_{J^+\ell jJ}(i_0,\omega). \tag{59}$$

Computed total and J-specific partial cross sections for $Kr^+(^2P_{3/2})$ formation from the unpolarized $2p_3$ $5p'[1/2]_1$ and $2p_4$ $5p'[3/2]_1$ intermediate levels [75] are compared to experimental results in figure 24. Apart from small deviations in the resonance widths and positions, the computed (a,c) and measured (b,d) total cross sections exhibit good overall agreement.

When the intermediate levels are polarized by photoexcitation from a lower level, the corresponding alignment/orientation has to be taken into account in the calculation [59, 74, 132]. The measured and computed spectra for photoionization of aligned $2p_2$ $5p'[3/2]_2$ and $2p_8$ $5p[5/2]_2$ intermediate states of ^{84}Kr, excited via linearly polarized laser radiation from the metastable $5s[3/2]_2$ level and ionized by a tunable laser with linear polarization parallel to that of the exciting laser, are compared in figure 25 and are in good agreement. With regard to the propensities for the resonance and the continuum cross sections and to the q parameters (large $|q|$ for the ARS excited from the $5p'$ levels and low $|q|$ for the ARS accessed from the 5p levels) the total and J-specific cross sections in figures 24 and 25 confirm the trends discussed above in connection with figure 22.

Two-step photoionization of the $(m+1)s[3/2]_2$ metastable level of Ne–Xe via the $(m+1)p[5/2]_3$ level is of special interest for the determination of densities of these metastable species in atomic beams or magneto-optical traps. Multiple optical pumping cycles of the closed $(m+1)s[3/2]_2 \rightarrow (m+1)p[5/2]_3$ transition by a linearly polarized continuous-wave laser leads to a saturated alignment of the excited state. The cross section ($J^+ = 3/2$ ion formation) for photoionization of the aligned $J = 3$ state with a linearly polarized laser having the electric vector either parallel ($\alpha = 0°$) or perpendicular σ ($\alpha = 90°$) to that of the exciting laser is given in terms of J-specific cross sections σ_J by [132]

$$\sigma(\alpha = 0°) = \frac{5}{3}\sigma_2 + \frac{1}{6}\sigma_3 + \frac{23}{18}\sigma_4\ , \tag{60}$$

$$\sigma(\alpha = 90°) = \frac{2}{3}\sigma_2 + \frac{17}{12}\sigma_3 + \frac{31}{36}\sigma_4\ . \tag{61}$$

The $J = 3$ contribution to the measured cross section shows a strong enhancement at $\alpha = 90°$ (rise by a factor 8.5 as compared to $\alpha = 0°$). This is clearly revealed by the measured and calculated cross sections for photoionization of aligned Kr $(5p[5/2]_3)$ for $\alpha = 0°$ and $\alpha = 90°$ (see figure 26), which demonstrate very good agreement in the lineshapes between experiment and theory [75].

Analogous results have been reported for photoionization of aligned Ar $(4p[5/2]_3)$ [75, 132], with J-specific cross sections reported in [132]. The measured absolute cross sections for the $(m + 1)p[5/2]_3$ levels of Ar and Kr [201] are somewhat smaller than those predicted in [75].

Aloïse *et al* [59] were able to determine the J-specific cross sections for two-step ionization of ground state Xe atoms via the $7s[3/2]_1$ intermediate level to the $J = 0$, 1, 2 final states in the region of the four $8p'$ resonances. They carried out measurements with linearly-polarized ($\alpha = 0°$ and 90°) as well as circularly-polarized light (parallel and antiparallel spins). The analyses included the effects of nonpure light polarizations and the depolarization of the intermediate level, caused by the hyperfine interaction (for ^{129}Xe and ^{131}Xe) and by collisions in the gas jet (for details, see [59, 126]).

5.2.2. 'Vanishing' resonance series. In some cases, ARS series are weak and thus hard to observe. An example is documented in figure 13 where the Ne $(13p'[K']_{0,2})$ resonances accessed from the Ne $(3s[3/2]_1, 3s'[1/2]_1)$ levels are shown. The $np'[K']_0$ resonances have low intensity when accessed from the $3s[3/2]_1$ level whereas they dominate when addressed from the $3s'[1/2]_1$ level. The simple explanation for the low probability of the $3s[3/2]_1 \rightarrow np'[1/2]_0$ transition as being caused by a core-changing process is not suitable because the levels $3s[3/2]_1$ and $3s'[1/2]_1$ levels both have substantial fractions of $J^+ = 1/2$ core, 42% and 58%, respectively [62]. The theoretical investigation of the $(m + 1)s', s[K]_1 \rightarrow np'[1/2]_0$ transitions within the CIPFCP approximation revealed that the low probability of the $3s[3/2]_1 \rightarrow np'[1/2]_0$ transition is mainly caused by the interference between two amplitudes which can be schematically represented as $\langle 3s\,|\mathbf{D}|\,np\rangle = \mathbf{a}$ and $\langle 3s\,|\mathbf{D}|\,3p\rangle\,\langle 2p3p\,|\mathbf{H}^{ee}|\,2pnp\rangle = \mathbf{b}$. The small value of the Coulomb matrix element $\langle 2p3p\,|\mathbf{H}^{ee}|\,2pnp\rangle$ is compensated by the large value of the transition moment $\langle 3s\,|\mathbf{D}|\,3p\rangle$, leading to similar values of the amplitudes **a** and **b**. The interference between **a** and **b** is destructive for the $3s[3/2]_1 \rightarrow np'[1/2]_0$ transition and constructive for the $3s'[1/2]_1 \rightarrow np'[1/2]_0$ transition, which explains the experimental observation [62]. A quantitative description of the experimental spectrum can be only obtained if all processes shown in scheme (33) are taken into account. If, for instance,

the configuration Ne $(2p^6)$, which basically describes the Ne ground state, is not included in the calculation of the $np'[1/2]_0$ wave functions, the computed widths of the $np'[1/2]_0$ resonances are three times smaller than observed.

Such interferences also play an important role in other spectra, e.g. in the case of the $4s', s[K]_1 \rightarrow 14p'[1/2]_0$ transitions in Ar. The $4s[3/2]_1 \rightarrow np'[1/2]_0$ transitions of Ar are expected to be suppressed by the interference [34], but no experimental data are available so far. The attempt to check this prediction using the $8s[3/2]_1 \rightarrow np'[1/2]_0$ transitions in Ar [60] is problematic because of additional interference between these transitions and the $7s'[1/2]_1 \rightarrow np'[1/2]_0$ transitions, caused by the strong mixing of the nearby $8s[3/2]_1$ and $7s'[1/2]_1$ levels [64], see also section 5.2.4.

Another example of 'vanishing' series is provided by the photoionization spectrum of Xe $(6d[3/2]_1)$. As expected, the experimental data clearly exhibit the $nf'[5/2]_2$ ARS, but the np' ARS appear to be missing, see figure 27. The reasons for this observation are [58] that (i) the oscillator strengths for the $6d \rightarrow np'$ transitions are much smaller than for the $6d \rightarrow nf'$ transitions; (ii) the strong interaction of the np' resonances with the $5p^5_{3/2}\varepsilon\ell$ continua yields widths of these resonances which are an order of magnitude larger than the widths of the nf' resonances (see also table 4(d)); (iii) the combined effects of (i) and (ii) yield weak dispersion-like profiles of the np' resonances (insert in figure 27) the detection of which requires very high signal-to-noise ratio and low photon bandwidth. In this context, the introduction of a generalized oscillator strength $f_g = f \cdot (q^2 - 1)/(q^2 + 1)$ can be useful for low $|q|$ [302]. Indeed, for Lorentzians $f_g = f$ while for dispersion profiles ($q = \pm 1$) $f_g = 0$. For $q = 0$ one obtains $f_g = -f$, expressing the fact that the ARS appears as an absorption window.

5.2.3. 'Vanishing' resonances. In the spectra of the Ar (np') ARS, excited from the $4s'[1/2]_1$ intermediate level, the expected $15p'[1/2]_1$, $15p'[3/2]_1$, and $15p'[3/2]_2$ resonances were found to be missing [64]. To illustrate the observations and the dependence on the intermediate level, figure 28 presents a comparison of the experimental np' spectra for the three unpolarized intermediate levels $4s'[1/2]_1$, $5s[3/2]_1$, and $5s'[1/2]_1$ with the results of CIPFCP calculations [64]. The experimental data were derived from spectra measured for parallel and perpendicular linear polarizations of the two light fields involved in the two-step excitation from the Ar ground state [60, 64]. The cross sections are displayed as a function of the common variable $-\mu$, a negative quantum defect used as scaled energy variable in order to compare spectra measured at different principal quantum numbers.

The $np'[1/2]_0$ ARS excited from the $5s'[1/2]_1$ level has a large oscillator strength $f^{np'[1/2]_0}_{5s'[1/2]_1}$ and exhibits a near-Lorentzian lineshape whereas in the spectra excited from the $5s[3/2]_1$ level the $np'[1/2]_0$ ARS has a dispersion lineshape because of the small oscillator strength $f^{np'[1/2]_0}_{5s[3/2]_1}$. The ratio between the $f^{np'[1/2]_0}_{5s'[1/2]_1}$ and $f^{np'[1/2]_0}_{5s[3/2]_1}$ oscillator strengths is governed by the interference discussed above for the Ne $(np'[1/2]_0)$ ARS. The narrow $np'[3/2]_2$ resonance has an oscillator strength larger than the $np'[3/2]_1$ resonance in line with the propensity rules [305]; the broad and weak $np'[1/2]_1$ resonance, lying between the $np'[3/2]_1$ and $np'[3/2]_2$ ARS, contributes to the background and is not observed as a separate resonance.

The observation of the $nf'[5/2]_2$ resonance can be attributed to electron correlation effects. Destructive interference between $3p^5 4s' \Longrightarrow 3p^5\{d\} \rightarrow 3p^5 nf'$ and $3p^5 4s' \rightarrow 3p^5\{p\} \Longrightarrow 3p^5 nf'$ excitation channels (double- and single-arrows denote Coulomb and electric-dipole interactions, respectively, as in scheme (33)) strongly reduces the $f^{nf'[5/2]_2}_{4s'[1/2]_1}$ oscillator strength, and the $nf'[5/2]_2$ ARS is only weakly excited from the $4s'[1/2]_1$ level (see figure 28(a)). In the spectra excited from the $5s[3/2]_1$ and $5s'[1/2]_1$ levels the $nf'[5/2]_2$ resonance is strong because the interference mentioned above is constructive.

The absence of the np' resonances in the spectrum excited from the $4s'[1/2]_1$ level reflects a (near-)zero excitation strength analogous to the Seaton–Cooper minima in near-threshold photoionization of the outer s electron of alkali-metal atoms (see section 5.1). This is demonstrated in figure 29(a) where the cross sections for the $3p^5 4s' \rightarrow 3p^5(n/\varepsilon)p'[K']_J$ transitions are depicted (the oscillator strengths are presented as a smooth curve; see equation (51)). All cross sections exhibit Seaton–Cooper minima at np binding energies in the range -0.15 eV $\leq \varepsilon_{np} \leq -0.05$ eV, resulting in 'vanishing' resonances. The predicted lineshapes of selected np resonances are shown in figure 29(b–e). They clearly demonstrate that the strong variation of the resonance spectra at, or very close to, specific n values can serve as a sensitive probe for the energy location of such a minimum in a particular channel and enable a rigorous test of the theoretical approaches.

5.2.4. Interaction between discrete levels in the initial and final states. Interaction between discrete levels, both in the initial and final states, may result in strong changes in the ARS spectra. One such example involves the $8s[3/2]_1 \rightarrow np'[1/2]_0$ and $7s'[1/2]_1 \rightarrow np'[1/2]_0$ transitions in Ar [60]. Because of the large mixing of the 'noninteracting' $8s_{ni}[3/2]_1$ and $7s'_{ni}[1/2]_1$ basis states (e.g., the observed $8s[3/2]_1$ level consists of 72% of $8s_{ni}[3/2]_1$ and 28% of $7s'_{ni}[1/2]_1$), both observed spectra primarily

reveal the $7s'_{ni}[1/2]_1$ character. Indeed, the oscillator strengths $f^{np'[K']_J}_{7s'_{ni}[1/2]_1}$ are much larger than $f^{np'[K']_J}_{8s_{ni}[3/2]_1}$ [64].

The Xe($nf'[5/2]_2$) resonances, excited from the $6s[3/2]_1$ and $4d[3/2]_1$ initial levels, provide another example which documents the effects of substantial initial state mixing on ARS spectra [34]. In this case the mixing of the $6s_{ni}[3/2]_1$ and $4d_{ni}[3/2]_1$ basis states (65% : 35%) and the large oscillator strengths $f^{nf'[5/2]_2}_{4d_{ni}[3/2]_1}$ lead to the observation of the transition $4d_{ni}[3/2]_1 \rightarrow nf'[5/2]_2$ in both spectra. Figure 30 shows comparisons between spectra computed with and without inclusion of the interaction between the $6s_{ni}[3/2]_1$ and $4d_{ni}[3/2]_1$ levels and the measurements and represents a further example of the importance of s–d interaction in the photoionization of rare-gas atoms.

The interactions between different channels manifest themselves over the entire series. The perturbations can be strong if different resonances with the same parity and J value overlap energetically, i.e., if either (i) different resonance series have similar quantum defects (modulo 1), or (ii) if adjacent members of the same series overlap significantly because of their large widths. Examples are: (i) the mixing of the $ns'[1/2]_1$ and $nd'[3/2]_1$ resonances for Ar, Kr, and Xe; (ii) mixing between the broad, partially overlapping, $nd'_{ni}[3/2]_1$ resonances for these atoms.

In Ar, for instance, the experimental quantum defects of the $ns'[1/2]_1$ and $nd'[3/2]_1$ resonances are 2.148(2) and 0.207(3), respectively (see table 4(b)). As a result the $ns'[1/2]_1$ and $nd'[3/2]_1$ series are substantially mixed, and the diffuse $nd'[3/2]_1$ resonances strongly influence the sharp $ns'[1/2]_1$ resonances, resulting in a decrease of the reduced width of the latter ARS by factor of about 2.5 due to destructive interference [77].

Inclusion of the interaction between the $nd'_{ni}[3/2]_1$ resonances via autoionization continua results in mixing of these resonances. The wave function of a particular $nd'[3/2]_1$ resonance acquires approximately equal contributions from the $(n-k)$ $d'_{ni}[3/2]_1$ and $(n+k)$ $d'_{ni}[3/2]_1$ resonances (but with opposite sign) which decrease with rising k value ($k = 1, 2, \ldots$) (see, e.g., equation (6) in [48]). Since the width of the lower-lying $(n-k)$ $d'_{ni}[3/2]_1$ resonance is always larger than the width of the higher-lying $(n+k)$ $d'_{ni}[3/2]_1$ resonance, a considerable destructive contribution to the Coulomb matrix element responsible for autoinization of the 'central' $nd'_{ni}[3/2]_1$ resonance results. For the Xe $8d'[3/2]_1$ ARS this destructive interference reduces the width of the 'noninteracting' resonance by a factor of 1.5.

5.3. Photoelectron spectrometry of excited Ne, Ar, Kr, and Xe atoms

So far, we were mainly concerned with the energy-dependent total photoionization cross sections of excited rare-gas atoms. Additional information on the partial cross sections to different ion states and on the underlying dipole matrix elements and phase shifts of the emitted electron is obtained by studying the kinetic energy, the angular distribution and the spin-polarization of the photoelectrons [178]. The rich phenomena observed in the angular-resolved photoelectron spectra of laser-excited alkali- and alkaline-earth-metal atoms have been nicely summarized by Leuchs and Walther [336] and can be used as a guide and motivation for photoelectron angular distribution (PAD) studies involving excited states of the rare-gas atoms. To date, however, PAD experiments on excited states of Ne–Xe are scarce. They include ionization from the metastable levels of Ne [69], Ar [71], Kr [71], and Xe [31,70], from the polarized $(m{+}1)$p $J = 3$ levels of Ne [183] and Ar [184], excited from the respective metastable $J = 2$ level by a cw laser, and from excited states of Ne ($3d[3/2]_1$, $3d'[3/2]_1$) [186] and Ar ($3d[1/2]_1$, $5s'[1/2]_1$, $3d'[3/2]_1$) [57], accessed from the respective ground state with monochromatized synchrotron radiation.

The PADs measured at selected photon energies from the metastable levels have already been presented in section 5.1. Experimental PADs across the $7p'[1/2,3/2]_1$ ARS of Xe, addressed from the metastable $J = 0$ level, were reported by Kau *et al.* [31]. The measured PAD parameters β exhibit a sharp and deep dip at the position of the $7p'[3/2]_1$ resonance which is well reproduced by a calculation using the RCN/RCG code of Cowan [337], see figure 31. A PAD study across ARS including spin-analysis of photoelectrons was carried out by Spieweck *et al* [18]. They measured the energy dependence of the total cross section, of the PAD parameter β, and of the electron spin parameter A [178] across the $9s'[1/2]_1$ and $7d'[3/2]_1$ ARS of Xe, excited by coherent VUV radiation (bandwidth about 1.2 cm^{-1}) from the Xe ground state. The RRPA calculations of Johnson *et al* [66] show qualitative agreement with the experimental data. Corresponding spin-analyzed measurements from excited states of rare-gas atoms have yet to be performed.

In the PAD work involving short-lived *excited* rare-gas atoms the polarization introduced by the photoexcitation process has to be taken into account in the data analysis [132, 183, 184, 186, 336, 338, 339]. In the following, we restrict the discussion to excitation-ionization by linearly-polarized light in the electric-dipole approximation. In pulsed single-photon excitation, the excited state acquires quadrupole alignment along the direction of the electric vector. Photoionization of this aligned state by another

linearly-polarized light field with electric vector parallel to that of the other light field results in a PAD which can be described by the expression [340]

$$\mathrm{d}\sigma/\mathrm{d}\Omega(\theta) = (\sigma_{\mathrm{tot}}/4\pi)[1 + \beta_2(P_2(\cos\theta) + \beta_4 P_4(\cos\theta)], \tag{62}$$

where θ denotes the angle between the momentum vector of the photoelectron and the direction of the parallel electric vectors of the two light fields, and $P_4(\cos\theta) = (35\cos^4\theta - 30\cos^2\theta + 3)/8$. The PAD parameters β_2 and β_4 are extracted from fits to the measured angular distributions (see, e.g., [186]).

When cw lasers are used for pumping closed transitions (such as the transitions $(m+1)$s $J = 2 \rightarrow (m+1)$p $J = 3$ from the $J = 2$ metastable levels of Ne–Xe), many cycles of induced absorption and spontaneous emission occur during the transit of the atoms through the driving light field. Consequently, both the lower and upper level acquire a polarization which is not only described by a quadrupole moment, but higher multipole moments with order up to $2J$, and the analysis of the PADs are more complicated [132, 184].

To simplify the analysis of their measurements on laser-aligned Ne (3p, $J = 3$) atoms, Siegel *et al* [183] only included the quadrupole alignment of the outer p electron and assumed that (i) the photoionization process does not depend on the total angular momentum J_{f} ($J_{\mathrm{f}} = J, J+1, J-1$) of the final [$\mathrm{Ne}^+ + \mathrm{e}^-(\varepsilon\mathrm{s}, \varepsilon\mathrm{d})$] states and that (ii) the spin–orbit interaction in the continuum can be neglected. Under these conditions, the measured PADs can be described by expressions equivalent to (62), and their analysis yielded the (reduced) dipole matrix elements d_{s} and d_{d} for emission of the s wave and d wave and the phase difference $\Delta = \delta_{\mathrm{d}} - \delta_{\mathrm{s}}$ between these waves. If the absolute cross section is not determined, one can only extract the ratio $\nu \equiv d_{\mathrm{d}}/d_{\mathrm{s}}$ and Δ [183]. For completeness, we mention here that—within these approximations—measurements of the polarization dependence of the total cross section $\sigma_{\mathrm{tot}}(\alpha)$ as a function of the angle α between the electric vectors of the linearly-polarized exciting and ionizing light fields yield the squares of the two relevant radial matrix elements, as exploited for Ne (3p, $J = 3$) [183]. In the following, we discuss two cases in more detail.

O'Keeffe *et al* [186] used velocity-map imaging of the photoelectrons to measure PADs for the core-conserving photoionization of aligned Ne $(3\mathrm{d}[3/2]_1)$ and Ne $(3\mathrm{d}'[3/2]_1)$ atoms to the final ion states $^2\mathrm{P}_{3/2}$ and $^2\mathrm{P}_{1/2}$, respectively, at photoelectron energies ε in the range $13 - 72$ meV. For Ne(3d), the energies were chosen such that the results are not influenced by autoionizing $n\mathrm{p}'$ or $n\mathrm{f}'$ resonances. The experimental results were analyzed with equation (62), and the fitted PAD parameters β_2 (open squares) and

β_4 (open circles) are summarized in figure 32 for (a) Ne (3d′) and (b) Ne (3d). The polar diagrams illustrate the shape of the PADs at $\varepsilon = 33$ meV (Ne 3d′) and $\varepsilon = 45$ meV (Ne 3d), respectively. Transitions to the ϵf ionization continua dominate. The curves represent the theoretical predictions for β_2 (full line) and β_4 (dashed line), as obtained in a quantum-defect treatment in which the spin–orbit interaction in the εp and εf electron continua was neglected but the J_f dependence of the matrix elements taken into account. When the J_f dependence is ignored, significantly poorer agreement between the predicted and the measured PAD parameters is observed; in particular, the parameter β_4 becomes zero for Ne $(3\mathrm{d}'[3/2]_1)$ in this approximation [186].

For photoionization of Ar (4p $J = 3$) atoms (prepared by excitation with a linearly-polarized cw-laser), the polarization dependence of the photoionization signal in the region of the 10d′ resonances [132] and of the PADs [184] at selected photoelectron energies demonstrated that both the spin–orbit interaction in the emitted d waves and the J_f dependence of the dipole matrix elements had to be included in the theoretical description. The corresponding calculations included the term dependence, some important electron correlations, and the effects of core–polarization on the radial wave functions of the excited and the continuum orbitals. The energy dependences of the five relevant ratios $\nu_{ik} = d_{ik}/d_{12}$ between the reduced dipole matrix elements d_{ik} for the d-wave ($k \equiv J_\mathrm{f}$; $i = 2j_\mathrm{f}$ with j_f = total angular momentum of continuum wave) and the reduced dipole matrix element d_{12} for the s-wave (right panel) are displayed in figure 33, which also shows the associated phase differences Δ_{ik} (left panel). In figure 34 we present the PADs (open circles), measured at four photoelectron energies (0.023, 0.144, 0.316, 0.846 eV) with parallel ($\alpha = 0°$) and perpendicular ($\alpha = 90°$) linear polarizations of the exciting and ionizing lasers (θ denotes the angle between the electron detection direction and the electric-field vector of the ionizing laser), and compare them with the results of three different calculations: (i) core polarization omitted (dotted curves); (ii) core polarization included (broken curves); (iii) core polarization included and ratios ν_{ik} of dipole matrix elements multiplied by a common correction factor K which was found to be weakly dependent on the photoelectron energy ϵ ($K(\epsilon) = 1.4 - 0.35(\epsilon/\mathrm{eV})$) (full curves). The correction factor serves the purpose of compensating the remaining deficiencies of the theoretical description.

In view of the paucity of the data measured so far and because of the possibility of carrying out accurate calculations, PADs from excited states of the heavier rare-gas atoms offer an interesting opportunity for combined experimental and theoretical studies in the future.

5.4. Effects of the hyperfine structure on the photoionization spectra of rare gases

Only few studies have observed the hyperfine structure in the spectra of rare gases; studies of the hyperfine structure of bound or autoionizing high-n Rydberg states are particularly scarce ([21, 22, 235–237] and references therein). Argon has no naturally occurring isotope with nuclear spin $I \neq 0$ and neon only one (^{21}Ne, $I = 3/2$) with very low natural abundance (0.27%). On the other hand, krypton has one (^{83}Kr with $I = 9/2$, 11.5%) and xenon two (^{129}Xe with $I = 1/2$, 26.4%, and ^{131}Xe with $I = 3/2$, 21.2%) isotopes with appreciable natural abundance, and these two gases represent ideal systems to study the role of the nuclear spin in the photoionization of rare-gas atoms.

In rare-gas isotopes with $I = 0$, autoionization results in a change of the spin–orbit state of the ion core, whereas in $I \neq 0$ isotopes, the autoionization may also involve a change in the hyperfine state of the ion core either with or without a change of spin–orbit state (see figure 35); between the lowest and the highest hyperfine component of the $m\mathrm{p}^5\,{}^2\mathrm{P}_{3/2}$ ionic ground state, pure hyperfine autoionization occurs [21,22]. For the study of these dynamical processes, MQDT was extended to treat the effects of nuclear spins, to derive partial photoionization cross sections to selected hyperfine states of the ion [21,22] and to derive the hyperfine structures of the $m\mathrm{p}^5\,{}^2\mathrm{P}_{3/2}$ and $m\mathrm{p}^5\,{}^2\mathrm{P}_{1/2}$ states from the hyperfine structures of high-n Rydberg states [21,22,235–237]. The hyperfine structures of the ions can be expressed as functions of the magnetic-dipole and electric-quadrupole hyperfine coupling constants A_{J^+} and B_{J^+} ($B_{J^+} = 0$ for $I \leq 1/2$ or $J^+ = 1/2$) as

$$\frac{E(J^+, F^+)}{h} = \frac{E(J^+)}{h} + A_{J^+}\frac{C}{2} + B_{J^+}\frac{\frac{3}{4}C(C+1) - I(I+1)J^+(J^+ + 1)}{2I(2I-1)J^+(2J^+ - 1)}, \tag{63}$$

where $C = F^+(F^+ + 1) - I(I + 1) - J^+(J^+ + 1)$ and $E(J^+)$ is the energy of the center of gravity of the hyperfine structure. Experimentally determined values of A_{J^+} and B_{J^+} for ^{83}Kr, ^{129}Xe, and ^{131}Xe are summarized in table 5 together with the hyperfine parameters for the $m\mathrm{p}^5(m{+}1)\mathrm{s}$ states, from which the missing values for $^{21}\mathrm{Ne}^+$ may be estimated [341, 342].

By single-photon excitation from the $(m\mathrm{p})^6\,{}^1\mathrm{S}_0$ ground state, only ns and nd Rydberg states with $J = 1$ are accessible in isotopes with $I = 0$ as a consequence of the standard selection rules for electric-dipole transitions. For isotopes with nuclear spin $I \neq 0$, the ΔJ selection rule for electric dipole transitions has to be replaced by the corresponding rule for ΔF. Therefore, it is possible to access hyperfine levels of ns and nd Rydberg states of ^{83}Kr or $^{129/131}$Xe with $J \neq 1$ from the $^1\mathrm{S}_0$ ground state (see

figures 36(b,c) and 37). The autoionizing Rydberg series of even isotopes ($I = 0$) exhibit the typical Beutler–Fano lineshape pattern (with narrow ns′ and broad nd′ lines) (see figure 36(a)), whereas for ^{83}Kr and $^{129/131}$Xe, the ns′ series ($n > 40$) exhibit an obvious splitting resulting from ns′$[1/2]_0$ and ns′$[1/2]_1$ series converging to the two hyperfine levels of the $^2P_{1/2}$ state, separated by

$$\Delta E_{\rm hf}(^2{\rm P}_{1/2})/h = [E(F^+ = I+1/2) - E(F^+ = I-1/2)]/h = A_{1/2}(I + 1/2). \tag{64}$$

Moreover, nd′ series with $J = 2$ or 3 appear with increasing intensities and mix with the $J = 1$ series to form a doublet separated by the hyperfine splitting of the ion for $n > 65$ (see figure 37(c)).

At very high n values, where the different Rydberg series are no longer fully resolved, the hyperfine structure is visible as an interference pattern in the spectrum of the Rydberg series, which leads to the periodic disappearance of the observable hyperfine structure (see figure 38). These stroboscopic resonances occur whenever the energy difference between two states of a Rydberg series is equal to the hyperfine splitting of the ion

$$|\Delta E_{\rm hf}(^2{\rm P}_{1/2})| \approx E(n + k) - E(n) \quad \text{with } k = 1, 2, \ldots \tag{65}$$

or, expressed with the effective principal quantum numbers $\nu_{J^+F^+}$ (16), when the condition

$$\nu_{1/2,\rm lower} = \nu_{1/2,\rm upper} + k \quad \text{with } k = 1, 2, \ldots \tag{66}$$

is fulfilled. The positions of these resonances can be used to determine the hyperfine splitting $\Delta E_{\rm hf}(^2{\rm P}_{1/2})$ [21, 22].

Interactions between channels differing in ℓ by $0, \pm 2$, notably between ns and nd channels, are important in the autoionization process and determine the lineshapes of autoionizing Rydberg states (see, e.g., [38] and section 4.2.1). The corresponding mixing angles in the MQDT parameter sets can be determined from the observed lineshapes or the positions of interacting bound Rydberg levels belonging to s and d series converging on different ionization limits. For $I = 0$ isotopes, the two series limits are the $^2P_{3/2}$ and $^2P_{1/2}$ states; because the separation between these limits is large for the heavier rare gases, the number of positions offering information on the s–d interaction is limited. In isotopes with $I > 0$, however, the s–d interaction can be studied with high accuracy from the positions of several consecutive levels of Rydberg series converging on different hyperfine levels of the $^2P_{3/2}$ ion state [236, 237]. In figure 39, the effects of s–d mixing are visible as avoided crossings between hyperfine levels of s and d Rydberg series of ^{83}Kr.

One of those, the avoided crossing between the $F = 11/2$ levels of the $(n-2)$d$[3/2]_1$ and ns$[3/2]_2$ Rydberg series around $n \approx 72$, has first been observed in high-resolution laser spectra [235] and later been studied at sub-MHz resolution with millimeter wave spectroscopy (see inset of figure 39) [236]. In the latter study, a MQDT parameter set for Kr (ns/d) levels has been derived from all available positions of the bound Rydberg states, but the MQDT parameters can also be used to describe the ARS, as has been shown by Paul *et al* [22]. A complete parameter set, which also includes np/f even-parity levels, has been derived for Xe following the same procedure [237].

The MQDT analysis of the hyperfine structure in high Rydberg states of the rare-gas atoms shows that, although the different Rydberg states have very different hyperfine structures, they all have their origin in the hyperfine structure of the $^2\mathrm{P}_{3/2}$ and $^2\mathrm{P}_{3/2}$ ionic levels. Rather than reporting individual hyperfine coupling parameters for each Rydberg state, it is much more convenient and meaningful to parametrize the hyperfine structure of Rydberg states with the hyperfine coupling constants of these ionic levels.

6. Conclusions

Spectroscopic investigations of the photoionization spectra of rare-gas atoms is a mature field of research which has provided exceptionally detailed information on the process of photoionization and significantly contributed to its understanding. Upon removal of an electron from the outermost valence orbitals of the neutral atoms, either directly by single-photoionization, or indirectly via an intermediate state, an open-shell $^2\mathrm{P}_{J^+}$ ion is produced with two fine-structure components of total angular momentum quantum number $J^+ = 3/2$ and $1/2$. Compared to the outer-valence-shell ionization of the alkali-metal atoms, which results in the formation of a closed-shell $^1\mathrm{S}_0$ ion core and an isolated ionization threshold, two closely spaced ionization thresholds are observed in the rare-gas atoms, between which the photoionization cross section is dominated by extended series of autoionizing resonances. The shape and intensities of these resonances strongly depend on the principal (n) and orbital angular momentum (ℓ) quantum numbers, as well as on the other quantum numbers (such as K and J) necessary to specify the fine structure of the autoionizing Rydberg states. They are also sensitive to the alignment and orientation of the state from which the electron is ejected. Spectra of autoionizing Rydberg states of the rare-gas atoms represent extremely sensitive probes of their electronic structures and their photoionization dynamics and can be used as rigorous tests of theoretical models of photoionization. Comparing spectra of neon,

argon, krypton, and xenon enables one to quantify the effects arising from the different atomic numbers, i.e., of the different number of electrons and the different magnitude of the spin–orbit interaction.

The information available in the literature on the autoionizing Rydberg states of the rare-gas atoms Ne–Xe is very extensive, but also very fragmented, most studies being devoted to the behaviour of a restricted number of resonances or ionization channels of a single rare-gas atom. Experimental data reported on the widths of autoionizing resonances and on the corresponding photoionization cross sections are often inconsistent, primarily because the effects of limited experimental resolution and saturation are difficult to recognize and quantify. Although the first good-quality spectroscopic data on autoionizing Rydberg states of the rare-gas atoms, primarily on those accessible from the $^1S_0$ ground state following single-photon excitation, have been reported more than 50 years ago, it is only in recent years that photoionization spectra from a broad range of electronically excited states have been obtained at a resolution sufficient to obtain reliable information on the shapes of autoionizing resonances and on the photoionization dynamics. Systematic comparison of spectral structures associated with the different ionization channels of different rare-gas atoms, obtained from different electronic states, enables one to recognize systematic trends. These trends, however, are often not explainable by simple arguments based, for instance, on the expectation that the widths of autoionizing resonances should monotonically decrease with increasing values of the orbital angular momentum quantum number ℓ, or on simple single-configuration descriptions of electronically excited states. The shape and intensities of autoionizing resonances result from subtle interference and electron-correlation effects, the understanding and theoretical description of which necessitates high-level *ab-initio* quantum chemical calculations.

In the present article, we have tried to critically review the literature on the autoionization resonances of the rare-gas atoms between the lowest two ionization thresholds and to provide what we believe is a reliable set of spectroscopic parameters describing the electronic structure and photoionization dynamics of these atoms. We have also attempted to summarize trends in behaviour observed experimentally and to rationalize them, whenever possible, in terms of well-established phenomena by making systematic comparison with theoretical predictions. The current status of the comparison is that state-of-the-art theoretical predictions are in almost quantitative agreement with experimental observations. The comparison of calculations performed on the basis of different levels of approximation reveals in which cases, and why, selected

approximations are likely to fail. Finally, we have also chosen to present numerous examples to illustrate the astonishing variety of phenomena that can be observed in spectroscopic studies of autoionizing resonances in the rare-gas atoms, which include ultrafast electron ejection, interference phenomena, the almost complete suppression of photoionization cross sections near Seaton–Cooper minima, fine- and hyperfine-structure-dependent autoionization rates, stroboscopic resonances observed when the period of the electronic motion matches the periods associated with hyperfine splittings, and autoionization processes resulting from the transfer of hyperfine energy from the ion core to the Rydberg electron.

The interest in studies of the Rydberg spectrum and the photoionization dynamics of the rare-gas atoms has been stimulated recently by new experimental methods enabling very high spectral resolution [122–124], very high calibration accuracy [343–345], very high temporal resolution [346, 347], or permitting the direct measurement of photoelectron angular distributions such as velocity map imaging [188] and photoelectron microscopy [348]. New applications of Rydberg states in atom- and molecule-optics experiments [349, 350] and the possibility to trap laser-cooled samples of metastable rare-gas atoms [78–83] will certainly stimulate further studies. We are convinced that the current knowledge of the electronic structure and photoionization dynamics of the rare-gas atoms, as derived from experimental and theoretical studies of the autoionization resonances and summarized in this article, will be useful in future studies.

Two specific aspects of particular interest to us, but only incompletely treated in this review, concern the angular distributions of photoelectrons ejected by autoionization of aligned and oriented samples and the process of hyperfine autoionization, which has been predicted theoretically on the basis of precision measurements of the hyperfine structure of high Rydberg states but has so far not been observed. One of the most promising systems for the observation of this process are autoionizing Rydberg states converging to the $^2\mathrm{P}_{1/2}$ ($F^+ = 0$) hyperfine level of $^{129}\mathrm{Xe}^+$. The decay of such Rydberg states into the ionization continuum associated with the $^2\mathrm{P}_{1/2}$ ($F^+ = 1$) level of the ion is energetically allowed above $n = 520$ and should be observable experimentally, but still represents an experimental challenge.

Acknowledgments

This work has been supported by the Deutsche Forschungsgemeinschaft (HO427/30, HO427/31), by the Swiss National Science Foundation (project number 200020-135342), and by the European Research Council advanced grant programme (project number 228286). HH gratefully acknowledges M Ya Amusia, S Baier, A Baig, J Bömmels, W Bußert, N A Cherepkov, J Ganz, J Geiger, A Gopalan, T Halfmann, K Harth, N Herschbach, U Hollenstein, R Kau, D Klar, T Kraft, E Leber, T Peters, M Raab, S Schohl, A Schramm, A Siegel, K and V Tsemekhman, K Ueda, and J M Weber for fruitful cooperation and ETH Zürich for the hospitality when parts of this review were written. FM thanks M Grütter, Ch Haase, U Hollenstein, E Kleimenov, Th Paul, M Raunhardt, M Sommavilla, E Vliegen, H J Wörner, A Wüest, and O Zehnder for their contributions to the work summarized in this review article. IDP and VLS thank the Fachbereich Physik at the University of Kaiserslautern for their support and hospitality. We acknowledge A Baig, P O'Keeffe, Y Y Lee, and M Meyer for providing experimental data in numerical form and for comments on their work.

References

[1] Berkowitz J 1979 *Photoabsorption, photoionization and photoelectron spectroscopy* (New York: Academic Press)
[2] Samson J A R and Ederer D L (eds) 2000 *Vacuum Ultraviolet Spectroscopy* (San Diego: Academic Press)
[3] Beutler H 1935 *Z. Phys.* **93** 177
[4] Fano U 1935 *Nuovo Cimento* **12** 154
Fano U, Pupillo G, Zannoni A and Clark C W 2005 *J. Res. Natl. Inst. Stand. Techn.* **110** 583 (English translation)
[5] Racah G 1942 *Phys. Rev.* **61** 537
[6] Fano U 1961 *Phys. Rev.* **124** 1866
[7] Fano U and Cooper J W 1965 *Phys. Rev.* **137** A1364
[8] Shore B W 1967 *J. Opt. Soc. Am.* **57** 881
[9] Shore B W 1968 *Phys. Rev.* **171** 43
[10] Ederer D L 1969 *Appl. Opt.* **8** 2315
[11] Madden R P and Codling K 1963 *Phys. Rev. Lett.* **10** 516
[12] Madden R P and Codling K 1964 *J. Opt. Soc. Am.* **54** 268
[13] Madden R P and Codling K 1965 *Astrophys. J.* **141** 364
[14] Wu J Z, Whitfield S B, Caldwell C D, Krause M O, van der Meulen P and Fahlman A 1990 *Phys. Rev. A* **42** 1350
[15] Maeda K, Ueda K and Ito K 1993 *J. Phys. B: At. Mol. Opt. Phys.* **26** 1541
[16] Bonin K D, McIlrath T J and Yoshino K 1985 *J. Opt. Soc. Am. B* **2** 1275

[17] Ernst W E, Softley T P and Zare R N 1988 *Phys. Rev. A* **37** 4172

[18] Spieweck M, Drescher M, Gierschner F, Irrgang R and Heinzmann U 1998 *Phys. Rev. A* **58** 1589

[19] Kortyna A, Darrach M R, Howe P T and Chutjian A 2000 *J. Opt. Soc. Am. B* **17** 1934

[20] Hollenstein U, Palm H and Merkt F 2000 *Rev. Sci. Instr.* **71** 4023

[21] Wörner H J, Grütter M, Vliegen E and Merkt F 2005 *Phys. Rev. A* **71** 052504
Wörner H J, Grütter M, Vliegen E and Merkt F 2006 *Phys. Rev. A* **73**, 059904 (erratum)

[22] Paul Th A, Liu J and Merkt F 2009 *Phys. Rev. A* **79** 022505

[23] Rhodes Ch K (ed) 1984 *Excimer Lasers* 2nd edn (*Topics in Applied Physics* vol 30) (Berlin: Springer)

[24] Stebbings R F and Dunning F B 1973 *Phys. Rev. A* **8** 665

[25] Dunning F B and Stebbings R F 1974 *Phys. Rev. A* **9** 2378

[26] Rundel R D, Dunning F B, Goldwire, Jr H C and Stebbings R F 1975 *J. Opt. Soc. Am.* **65** 628

[27] Grandin J P and Husson X 1981 *J. Phys. B: At. Mol. Phys.* **14** 433

[28] King R F and Latimer C J 1982 *J. Opt. Soc. Am.* **72** 306

[29] Knight R D and Wang L G 1986 *J. Opt. Soc. Am. B* **3** 1673

[30] Muhlpfordt A and Even U 1995 *J. Chem. Phys.* **103** 4427

[31] Kau R, Klar D, Schohl S, Baier S and Hotop H 1996 *Z. Phys. D* **36** 23

[32] Hanif M, Aslam M, Riaz M, Bhatti S A and Baig M A 2005 *J. Phys. B: At. Mol. Opt. Phys.* **38** S65

[33] Peters T, Halfmann T, Even U, Wünnenberg A, Petrov I D, Sukhorukov V L and Hotop H 2005 *J. Phys. B: At. Mol. Opt. Phys.* **38** S51

[34] Petrov I D, Peters T, Halfmann T, Aloïse S, O'Keeffe P, Meyer M, Sukhorukov V L and Hotop H 2006 *Eur. Phys. J. D* **40** 181

[35] Delsart C and Keller J C 1983 *Phys. Rev. A* **28** 845

[36] Ganz J, Siegel A, Bußert W, Harth K, Ruf M W, Hotop H, Geiger J and Fink M 1983 *J. Phys. B: At. Mol. Phys.* **16** L569

[37] Ganz J, Raab M, Hotop H and Geiger J 1984 *Phys. Rev. Lett.* **53** 1547

[38] Harth K, Ganz J, Raab M, Lu K T, Geiger J and Hotop H 1985 *J. Phys. B: At. Mol. Phys.* **18** L825

[39] Wang L G and Knight R D 1986 *Phys. Rev. A* **34** 3902

[40] Klar D, Harth K, Ganz J, Kraft T, Ruf M W, Hotop H, Tsemekhman V, Tsemekhman K and Amusia M Ya 1992 *Z. Phys. D* **23** 101

[41] Hotop H, Klar D and Schohl S 1992 *Inst. Phys. Conf. Ser.* **128** 45

[42] Klar D, Ueda K, Ganz J, Harth K, Bußert W, Baier S, Weber J M, Ruf M W and Hotop H 1994 *J. Phys. B: At. Mol. Opt. Phys.* **27** 4897

[43] Landais J, Huet M, Kucal H and Dohnalik T 1995 *J. Phys. B: At. Mol. Opt. Phys.* **28** 2395

[44] Aslam M, Ali R, Nadeem A, Bhatti S A and Baig M A 1999 *Opt. Commun.* **172** 37

[45] Weber J M, Ueda K, Klar D, Kreil J, Ruf M W and Hotop H 1999 *J. Phys. B: At. Mol. Opt. Phys.* **32** 2381

[46] Bömmels J, Weber J M, Gopalan A, Herschbach N, Leber E, Schramm A, Ueda K, Ruf M W and Hotop H 1999 *J. Phys. B: At. Mol. Opt. Phys.* **32** 2399

[47] Klar D, Aslam M, Baig M A, Ueda K, Ruf M W and Hotop H 2001 *J. Phys. B: At. Mol. Opt. Phys.* **34** 1549

[48] Hanif M, Aslam M, Ali R, Bhatti S A, Baig M A, Klar D, Ruf M W, Petrov I D, Sukhorukov V L and Hotop H 2004 *J. Phys. B: At. Mol. Opt. Phys.* **37** 1987
[49] Baig M A, Hanif M, Aslam M and Bhatti S A 2006 *J. Phys. B: At. Mol. Opt. Phys.* **39** 4221
[50] Baig M A, Hanif M and Aslam M 2008 *J. Phys. B: At. Mol. Opt. Phys.* **41** 035004
[51] Dehmer J L, Pratt S T and Dehmer P M 1987 *Phys. Rev. A* **36** 4494
[52] Pratt S T, Dehmer P M and Dehmer J L 1987 *Phys. Rev. A* **35** 3793
[53] Koeckhoven S M, Buma W J and de Lange C A 1994 *Phys. Rev. A* **49** 3322
[54] Blazewicz P R, Stockdale J A D, Miller J C, Efthimiopoulos T and Fotakis C 1987 *Phys. Rev. A* **35** 1092
[55] Koeckhoven S M, Buma W J and de Lange C A 1995 *Phys. Rev. A* **51** 1097
[56] Gisselbrecht M, Marquette A and Meyer M 1998 *J. Phys. B: At. Mol. Opt. Phys.* **31** L977
[57] Mitsuke K, Hikosaka Y and Iwasaki K 2000 *J. Phys. B: At. Mol. Opt. Phys.* **33** 391
[58] Meyer M, Gisselbrecht M, Marquette A, Delisle C, Larzillière M, Petrov I D, Demekhina N V and Sukhorukov V L 2005 *J. Phys. B: At. Mol. Opt. Phys.* **38** 285
[59] Aloïse S, O'Keeffe P, Cubaynes D, Meyer M and Grum-Grzhimailo A N 2005 *Phys. Rev. Lett.* **94** 223002
[60] Lee Y Y, Dung T Y, Hsieh R M, Yuh J Y, Song Y F, Ho G H, Huang T P, Pan W C, Chen I C, Tu S Y, Kung A H and Lee L C 2008 *Phys. Rev. A* **78** 022509
[61] Meyer M, Costello J T, Düsterer S, Li W B and Radcliffe P 2010 *J. Phys. B: At. Mol. Opt. Phys.* **43** 194006
[62] Petrov I D, Sukhorukov V L, Peters T, Zehnder O, Wörner H J, Merkt F and Hotop H 2006 *J. Phys. B: At. Mol. Opt. Phys.* **39** 3159
[63] Grütter M, Zehnder O, Softley T P and Merkt F 2008 *J. Phys. B: At. Mol. Opt. Phys.* **41** 115001
[64] Petrov I D, Sukhorukov V L, Hollenstein U, Kaufmann L J, Merkt F and Hotop H 2011 *J. Phys. B: At. Mol. Opt. Phys.* **44** 025004
[65] Johnson W R and Le Dourneuf M 1980 *J. Phys. B: At. Mol. Phys.* **13** L13
[66] Johnson W R, Cheng K T, Huang K N and Le Dourneuf M 1980 *Phys. Rev. A* **22** 989
[67] Taylor K T and Scott N S 1981 *J. Phys. B: At. Mol. Phys.* **14** L237
[68] Radojević V and Talman J D 1990 *J. Phys. B: At. Mol. Opt. Phys.* **23** 2241
[69] Kau R, Petrov I D, Sukhorukov V L and Hotop H 1996 *J. Phys. B: At. Mol. Opt. Phys.* **29** 5673
Kau R, Petrov I D, Sukhorukov V L and Hotop H 1997 *J. Phys. B: At. Mol. Opt. Phys.* **30**, 2317 (erratum)
[70] Kau R, Petrov I, Sukhorukov V and Hotop H 1997 *Z. Phys. D* **39** 267
Kau R, Petrov I, Sukhorukov V and Hotop H 1997 *Z. Phys. D* **42**, 318 (erratum)
[71] Kau R, Petrov I D, Sukhorukov V L and Hotop H 1998 *J. Phys. B: At. Mol. Opt. Phys.* **31** 1011
[72] Petrov I D, Sukhorukov V L and Hotop H 1999 *J. Phys. B: At. Mol. Opt. Phys.* **32** 973
[73] Petrov I D, Sukhorukov V L and Hotop H 2008 *J. Phys. B: At. Mol. Opt. Phys.* **41** 065205
[74] Petrov I D, Sukhorukov V L, Ruf M W and Hotop H 2009 *Eur. Phys. J. D* **53** 289
[75] Petrov I D, Sukhorukov V L, Ruf M W, Klar D and Hotop H 2011 *Eur. Phys. J. D* **62** 347
[76] Petrov I D, Sukhorukov V L and Hotop H 2002 *J. Phys. B: At. Mol. Opt. Phys.* **35** 323
[77] Petrov I D, Sukhorukov V L and Hotop H 2003 *J. Phys. B: At. Mol. Opt. Phys.* **36** 119
[78] Shimizu F, Shimizu K and Takuma H 1989 *Phys. Rev. A* **39** 2758
[79] Katori H and Shimizu F 1993 *Phys. Rev. Lett.* **70** 3545

[80] Walhout M, Witte A and Rolston S L 1994 *Phys. Rev. Lett.* **72** 2843
[81] Kuppens S J M, Tempelaars J G C, Mogendorff V P, Claessens B J, Beijerinck H C W and Vredenbregt E J D 2002 *Phys. Rev. A* **65** 023410
[82] Robert A, Sirjean O, Browaeys A, Poupard J, Nowak S, Boiron D, Westbrook C I and Aspect A 2001 *Science* **292** 461
[83] Pereira Dos Santos F, Léonard J, Wang J, Barrelet C J, Perales F, Rasel E, Unnikrishnan C S, Leduc M and Cohen-Tannoudji C 2001 *Phys. Rev. Lett.* **86** 3459
[84] Claessens B J, Ashmore J P, Sang R T, MacGillivray W R, Beijerinck H C W and Vredenbregt E J D 2006 *Phys. Rev. A* **73** 012706
[85] Uhlmann L J, Dall R G, Truscott A G, Hoogerland M D, Baldwin K G H and Buckman S J 2005 *Phys. Rev. Lett.* **94** 173201
[86] Walhout M, Sterr U, Orzel C, Hoogerland M and Rolston S L 1995 *Phys. Rev. Lett.* **74** 506
[87] Spoden P, Zinner M, Herschbach N, van Drunen W J, Ertmer W and Birkl G 2005 *Phys. Rev. Lett.* **94** 223201
[88] Busch H C, Shaffer M K, Ahmed E M and Sukenik C I 2006 *Phys. Rev. A* **73** 023406
[89] Byron L J, Dall R G, Rugway W and Truscott A G 2010 *New J. Phys.* **12** 013004
[90] Matherson K J, Glover R D, Laban D E and Sang R T 2008 *Phys. Rev. A* **78** 042712
[91] Zinner M, Spoden P, Kraemer T, Birkl G and Ertmer W 2003 *Phys. Rev. A* **67** 010501(R)
[92] Lefers J, Miller N, Rupke D, Tong D and Walhout M 2002 *Phys. Rev. A* **66** 012507
[93] Walhout M, Sterr U, Witte A and Rolston S L 1995 *Opt. Lett.* **20** 1192
[94] Orzel C, Walhout M, Sterr U, Julienne P S and Rolston S L 1999 *Phys. Rev. A* **59** 1926
[95] Huffman R E, Larrabee J C and Chambers D 1965 *Appl. Opt.* **4** 1145
[96] Huffman R E, Larrabee J C and Tanaka Y 1965 *Appl. Opt.* **4** 1581
[97] Ito K, Namioka T, Morioka Y, Sasaki T, Noda H, Goto K, Katayama T and Koike M 1986 *Appl. Opt.* **25** 837
[98] Heimann P A, Koike M, Hsu C W, Blank D, Yang X M, Suits A G, Lee Y T, Evans M, Ng C Y, Flaim C and Padmore H A 1997 *Rev. Sci. Instr.* **68** 1945
[99] Nahon L, Alcaraz C, Marlats J L, Lagarde B, Polack F, Thissen R, Lepère D and Ito K 2001 *Rev. Sci. Instr.* **72** 1320
[100] Ito K, Maeda K, Morioka Y and Namioka T 1989 *Appl. Opt.* **28** 1813
[101] Thorne A P, Harris C J, Wynne-Jones I, Learner R C M and Cox G 1987 *J. Phys. E: Sci. Instrum.* **20** 54
[102] Thorne A 1996 *Phys. Scr.* **T65** 31
[103] de Oliveira N, Joyeux D, Phalippou D, Rodier J C, Polack F, Vervloet M and Nahon L 2009 *Rev. Sci. Instr.* **80** 043101
[104] Ivanov T I, Dickenson G D, Roudjane M, de Oliveira N, Joyeux D, Nahon L, Tchang-Brillet W Ü L and Ubachs W 2010 *Mol. Phys.* **108** 771
[105] Vidal C R 1980 *Appl. Opt.* **19** 3897
[106] Stoicheff B P, Herman P R, LaRocque P F and Lipson R H 1985 *Laser Spectroscopy VII*, eds T W Hänsch and Y R Shen (Berlin: Springer) pp 174–178
[107] Hilbig R, Hilber G, Lago A, Wolff B and Wallenstein R 1986 *Comments At. Mol. Phys.* **18** 157
[108] Vidal C R 1987 *Tunable Lasers* (*Topics in Applied Physics* vol 59) eds L F Mollenauer and J C White (Berlin: Springer) pp 57–113

[109] Kung A H 1983 *Opt. Lett.* **8** 24
[110] Rettner C T, Marinero E E, Zare R N and Kung A H 1984 *J. Phys. Chem.* **88** 4459
[111] Rupper P and Merkt F 2004 *Rev. Sci. Instr.* **75** 613
[112] Merkt F, Osterwalder A, Seiler R, Signorell R, Palm H, Schmutz H and Gunzinger R 1998 *J. Phys. B: At. Mol. Opt. Phys.* **31** 1705
[113] Merkt F and Schmutz H 1998 *J. Chem. Phys.* **108** 10033
[114] Cromwell E, Trickl T, Lee Y T and Kung A H 1989 *Rev. Sci. Instr.* **60** 2888
[115] Ubachs W, Eikema K S E, Hogervorst W and Cacciani P C 1997 *J. Opt. Soc. Am. B* **14** 2469
[116] Eikema K S E, Ubachs W, Vassen W and Hogervorst W 1997 *Phys. Rev. A* **55** 1866
[117] Hollenstein U, Seiler R, Schmutz H, Andrist M and Merkt F 2001 *J. Chem. Phys.* **115** 5461
[118] Trickl T, Kung A H and Lee Y T 2007 *Phys. Rev. A* **75** 022501
[119] Brandi F, Velchev I, Neshev D, Hogervorst W and Ubachs W 2003 *Rev. Sci. Instr.* **74** 32
[120] Seiler R, Paul Th, Andrist M and Merkt F 2005 *Rev. Sci. Instr.* **76** 103103
[121] Paul Th A and Merkt F 2005 *J. Phys. B: At. Mol. Opt. Phys.* **38** 4145
[122] Merkt F and Osterwalder A 2002 *Int. Rev. Phys. Chem.* **21** 385
[123] Schäfer M, Andrist M, Schmutz H, Lewen F, Winnewisser G and Merkt F 2006 *J. Phys. B: At. Mol. Opt. Phys.* **39** 831
[124] Schäfer M and Merkt F 2009 *Frontiers of Molecular Spectroscopy*, ed J Laane (Amsterdam: Elsevier) pp 35–61
[125] L'Huillier A, Lompre L A, Normand D, Morellec J, Ferray M, Lavancier J, Mainfray G and Manus C 1989 *J. Opt. Soc. Am. B* **6** 1644
[126] Meyer M 2009 *Nucl. Instr. and Meth. in Phys. Res. A* **601** 88
[127] Stellpflug M, Johnsson M, Petrov I and Halfmann T 2003 *Eur. Phys. J. D* **23** 35
[128] He L W, Burkhardt C E, Ciocca M, Leventhal J J and Manson S T 1991 *Phys. Rev. Lett.* **67** 2131
[129] Small-Warren N E and Chow Chiu L Y 1975 *Phys. Rev. A* **11** 1777
[130] Ligtenberg R C G, van der Burgt P J M, Renwick S P, Westerveld W B and Risley J S 1994 *Phys. Rev. A* **49** 2363
[131] Avgoustoglou E N and Beck D R 1998 *Phys. Rev. A* **57** 4286
[132] Schohl S, Klar D, Cherepkov N A, Petrov I D, Ueda K, Baier S, Kau R and Hotop H 1997 *J. Phys. B: At. Mol. Opt. Phys.* **30** 609
[133] Gay T J 1996 *Atomic, Molecular, and Optical Physics: Atoms and Molecules* (*Experimental Methods in the Physical Sciences* vol 29B) eds F B Dunning and R G Hulet (San Diego: Academic Press) pp 95–114
[134] Halfmann T, Koensgen J and Bergmann K 2000 *Meas. Sci. Technol.* **11** 1510
[135] DeKieviet M, Dürr M, Epp S, Lang F and Theis M 2004 *Rev. Sci. Instr.* **75** 345
[136] Ding Y, Bailey K, Davis A M, Hu S M, Lu Z T and O'Connor T P 2006 *Rev. Sci. Instr.* **77** 126105
[137] Schohl S, Klar D, Kraft T, Meijer H A J, Ruf M W, Schmitz U, Smith S J and Hotop H 1991 *Z. Phys. D* **21** 25
[138] Higgins M J and Latimer C J 1993 *Phys. Scr.* **48** 675
[139] Pellarin M, Vialle J L, Carré M, Lermé J and Aymar M 1988 *J. Phys. B: At. Mol. Opt. Phys.* **21** 3833

[140] Thekaekara M and Dieke G H 1958 *Phys. Rev.* **109** 2029

[141] Huffman R E, Tanaka Y and Larrabee J C 1963 *J. Chem. Phys.* **39** 902

[142] Huffman R E, Tanaka Y and Larrabee J C 1963 *Appl. Opt.* **2** 947

[143] Comes F J, Sälzer H G and Schumpe G 1968 *Z. Naturforsch. A* **23** 137

[144] Hudson R D and Carter V L 1968 *J. Opt. Soc. Am.* **58** 227

[145] Carter V L and Hudson R D 1973 *J. Opt. Soc. Am.* **63** 733

[146] Yoshino K 1970 *J. Opt. Soc. Am.* **60** 1220

[147] Yoshino K and Tanaka Y 1979 *J. Opt. Soc. Am.* **69** 159

[148] Yoshino K and Freeman D E 1985 *J. Opt. Soc. Am. B* **2** 1268

[149] Baig M A and Connerade J P 1984 *J. Phys. B: At. Mol. Phys.* **17** 1785

[150] Ito K, Ueda K, Namioka T, Yoshino K and Morioka Y 1988 *J. Opt. Soc. Am. B* **5** 2006

[151] Ueda K, Maeda K, Ito K and Namioka T 1989 *J. Phys. B: At. Mol. Opt. Phys.* **22** L481

[152] Maeda K, Ueda K, Ito K and Namioka T 1990 *Phys. Scr.* **41** 464

[153] Maeda K, Ueda K, Namioka T and Ito K 1992 *Phys. Rev. A* **45** 527

[154] van der Ende B M, Winslade C, Brooks R L, deLaat R H and Westwood N P C 2009 *Can. J. Phys.* **87** 575

[155] Barbieri B, Beverini N and Sasso A 1990 *Rev. Mod. Phys.* **62** 603

[156] Ahmed M, Zia M A, Baig M A and Suleman B 1997 *J. Phys. B: At. Mol. Opt. Phys.* **30** 2155

[157] Hanif M, Aslam M, Ali R, Nadeem A, Riaz M, Bhatti S A and Baig M A 2000 *J. Phys. B: At. Mol. Opt. Phys.* **33** 4647

[158] Mahmood S, Amin N, ul Haq S, Shaikh N M, Hussain S and Baig M A 2006 *J. Phys. B: At. Mol. Opt. Phys.* **39** 2299

[159] Baig M A, Mahmood S, Mumtaz R, Rafiq M, Kalyar M A, Hussain S and Ali R 2008 *Phys. Rev. A* **78** 032524

[160] Labastie P, Biraben F and Giacobino E 1982 *J. Phys. B: At. Mol. Phys.* **15** 2595

[161] Lemoigne J, Grandin J, Husson X and Kucal H 1984 *J. Physique (Paris)* **45** 249

[162] Bounakhla M, Lemoigne J P, Grandin J P, Husson X, Kucal H and Aymar M 1993 *J. Phys. B: At. Mol. Opt. Phys.* **26** 345

[163] Delsart C, Keller J C and Thomas C 1981 *J. Phys. B: At. Mol. Phys.* **14** 3355

[164] Piracha N K, Suleman B, Khan S H and Baig M A 1995 *J. Phys. B: At. Mol. Opt. Phys.* **28** 2525

[165] Piracha N K, Baig M A, Khan S H and Suleman B 1997 *J. Phys. B: At. Mol. Opt. Phys.* **30** 1151

[166] Ahmed M, Baig M A and Suleman B 1998 *J. Phys. B: At. Mol. Opt. Phys.* **31** 4017

[167] Lawler J E, Ferguson A I, Goldsmith J E M, Jackson D J and Schawlow A L 1979 *Phys. Rev. Lett.* **42** 1046

[168] Goldsmith J E M, Ferguson A I, Lawler J E and Schawlow A L 1979 *Opt. Lett.* **4** 230

[169] Hänsch T W, Lyons D R, Schawlow A L, Siegel A, Wang Z Y and Yan G Y 1981 *Opt. Commun.* **38** 47

[170] Lyons D R, Schawlow A L and Yan G Y 1981 *Opt. Commun.* **38** 35

[171] Demtröder W 1993 *Laserspektroskopie* (Berlin: Springer-Verlag)

[172] Gallagher T F 1994 *Rydberg Atoms* (Cambridge: Cambridge University Press)

[173] Hotop H and Niehaus A 1967 *J. Chem. Phys.* **47** 2506

[174] Harth K, Raab M, Ganz J, Siegel A, Ruf M W and Hotop H 1985 *Opt. Commun.* **54** 343

[175] Schramm A, Weber J M, Kreil J, Klar D, Ruf M W and Hotop H 1998 *Phys. Rev. Lett.* **81** 778

[176] Frey M T, Ling X, Lindsay B G, Smith K A and Dunning F B 1993 *Rev. Sci. Instr.* **64** 3649

[177] Osterwalder A and Merkt F 1999 *Phys. Rev. Lett.* **82** 1831

[178] Schmidt V 1992 *Rep. Prog. Phys.* **55** 1483

[179] Cooper J and Zare R N 1968 *J. Chem. Phys.* **48** 942
Cooper J and Zare R N 1968 *J. Chem. Phys.* **49**, 4252 (erratum)

[180] Samson J A R and Gardner J L 1973 *Phys. Rev. Lett.* **31** 1327

[181] Morioka Y, Watanabe M, Akahori T, Yagishita A and Nakamura M 1985 *J. Phys. B: At. Mol. Phys.* **18** 71

[182] Caldwell C D and Krause M O 1990 *J. Phys. B: At. Mol. Opt. Phys.* **23** 2233

[183] Siegel A, Ganz J, Bußert W and Hotop H 1983 *J. Phys. B: At. Mol. Phys.* **16** 2945

[184] Schohl S, Cherepkov N A, Petrov I D, Sukhorukov V L, Baier S and Hotop H 1998 *J. Phys. B: At. Mol. Opt. Phys.* **31** 3363

[185] Haber L H, Doughty B and Leone S R 2009 *Phys. Rev. A* **79** 031401(R)

[186] O'Keeffe P, Bolognesi P, Mihelič A, Moise A, Richter R, Cautero G, Stebel L, Sergo R, Pravica L, Ovcharenko E, Decleva P and Avaldi L 2010 *Phys. Rev. A* **82** 052522

[187] Helm H, Bjerre N, Dyer M J, Huestis D L and Saeed M 1993 *Phys. Rev. Lett.* **70** 3221

[188] Parker D H and Eppink A T J B 1997 *J. Chem. Phys.* **107** 2357

[189] Saeed M and Helm H 1994 *Chem. Phys.* **179** 115

[190] Smith A V, Goldsmith J E M, Nitz D E and Smith S J 1980 *Phys. Rev. A* **22** 577

[191] Burkhardt C E, Libbert J L, Xu J, Leventhal J J and Kelley J D 1988 *Phys. Rev. A* **38** 5949

[192] Ambartzumian R V, Furzikov N P, Letokhov V S and Puretsky A A 1976 *Appl. Phys.* **9** 335

[193] Heinzmann U, Schinkowski D and Zeman H D 1977 *Appl. Phys.* **12** 113

[194] Gisselbrecht M, Descamps D, Lyngå C, L'Huillier A, Wahlström C G and Meyer M 1999 *Phys. Rev. Lett.* **82** 4607

[195] Hussain S, Saleem M, Rafiq M and Baig M A 2006 *Phys. Rev. A* **74** 022715

[196] Bonin K D, Gatzke M, Collins C L and Kadar-Kallen M A 1989 *Phys. Rev. A* **39** 5624

[197] Dinneen T P, Wallace C D, Tan K Y N and Gould P L 1992 *Opt. Lett.* **17** 1706

[198] Gilbert S L, Noecker M C and Wieman C E 1984 *Phys. Rev. A* **29** 3150

[199] Hotop H 1996 *Atomic, Molecular, and Optical Physics: Atoms and Molecules* (*Experimental Methods in the Physical Sciences* vol 29B) eds F B Dunning and R G Hulet (San Diego: Academic Press) pp 191–215

[200] Dunning F B, Rundel R D and Stebbings R F 1975 *Rev. Sci. Instr.* **46** 697

[201] Kau R, Leber E, Schramm A, Klar D, Baier S and Hotop H 1995 *AIP Conf. Proc.* **329** 146

[202] Berkowitz J 1988 *Adv. Chem. Phys.* **72** 1

[203] Zatsarinny O and Bartschat K 2004 *J. Phys. B: At. Mol. Opt. Phys.* **37** 4693

[204] Zatsarinny O 2006 *Comput. Phys. Commun.* **174** 273

[205] Zatsarinny O and Bartschat K 2006 *J. Phys. B: At. Mol. Opt. Phys.* **39** 2145

[206] Bartschat K and Zatsarinny O 2007 *J. Phys. B: At. Mol. Opt. Phys.* **40** F43

[207] Brage T, Froese Fischer C and Jönsson P 1994 *Phys. Rev. A* **49** 2181

[208] Jönsson P, Ynnerman A, Froese Fischer C, Godefroid M R and Olsen J 1996 *Phys. Rev. A* **53** 4021

[209] Seaton M J 1983 *Rep. Prog. Phys.* **46** 167

[210] Greene C H and Jungen Ch 1985 *Adv. At. Mol. Phys.* **21** 51

[211] Jungen Ch (ed) 1996 *Molecular Applications of Quantum Defect Theory* (Bristol and Philadelphia: Institute of Physics Publishing)
[212] Aymar M, Greene C H and Luc-Koenig E 1996 *Rev. Mod. Phys.* **68** 1015
[213] Fano U 1975 *J. Opt. Soc. Am.* **65** 979
[214] Fano U 1970 *Phys. Rev. A* **2** 353
Fano U 1977 *Phys. Rev. A* **15**, 817 (erratum)
[215] Lu K T and Fano U 1970 *Phys. Rev. A* **2** 81
[216] Lu K T 1971 *Phys. Rev. A* **4** 579
[217] Lee C M and Lu K T 1973 *Phys. Rev. A* **8** 1241
[218] Dill D 1973 *Phys. Rev. A* **7** 1976
[219] Lee C M 1974 *Phys. Rev. A* **10** 584
[220] Lee C M 1974 *Phys. Rev. A* **10** 1598
[221] Seaton M J 1958 *Mon. Not. R. Astron. Soc.* **118** 504
[222] Seaton M J 1966 *Proc. Phys. Soc.* **88** 801
[223] Seaton M J 1969 *J. Phys. B: At. Mol. Phys.* **2** 5
[224] Johnson W R and Lin C D 1979 *Phys. Rev. A* **20** 964
[225] Lee C M and Johnson W R 1980 *Phys. Rev. A* **22** 979
[226] Starace A F 1973 *J. Phys. B: At. Mol. Phys.* **6** 72
[227] Aymar M 1975 *J. Physique (Paris)* **36** 299
[228] Geiger J 1976 *Z. Phys. A* **276** 219
[229] Geiger J 1977 *Z. Phys. A* **282** 129
[230] Harth K, Raab M and Hotop H 1987 *Z. Phys. D* **7** 213
[231] Aymar M, Robaux O and Thomas C 1981 *J. Phys. B: At. Mol. Phys.* **14** 4255
[232] L'Huillier A, Tang X and Lambropoulos P 1989 *Phys. Rev. A* **39** 1112
[233] Audouard E, Laporte P, Subtil J L, Damany N and Pellarin M 1990 *Phys. Rev. A* **41** 6032
[234] Ito K, Masuda H, Morioka Y and Ueda K 1993 *Phys. Rev. A* **47** 1187
[235] Wörner H J, Hollenstein U and Merkt F 2003 *Phys. Rev. A* **68** 032510
[236] Schäfer M and Merkt F 2006 *Phys. Rev. A* **74** 062506
[237] Schäfer M, Raunhardt M and Merkt F 2010 *Phys. Rev. A* **81** 032514
[238] Giusti-Suzor A and Fano U 1984 *J. Phys. B: At. Mol. Phys.* **17** 215
[239] Cooke W E and Cromer C L 1985 *Phys. Rev. A* **32** 2725
[240] Ueda K 1987 *Phys. Rev. A* **35** 2484
[241] Ueda K 1997 *AIP Conf. Proc.* **386** 237
[242] Ueda K 1987 *J. Opt. Soc. Am. B* **4** 424
[243] Knight R D 1986 *Phys. Rev. A* **34** 3809
[244] Sakimoto K 1986 *J. Phys. B: At. Mol. Phys.* **19** 3011
[245] Sakimoto K 1989 *J. Phys. B: At. Mol. Opt. Phys.* **22** 2727
[246] Fielding H H and Softley T P 1992 *J. Phys. B: At. Mol. Opt. Phys.* **25** 4125
[247] Softley T P, Hudson A J and Watson R 1997 *J. Chem. Phys.* **106** 1041
[248] Vliegen E 2006 PhD thesis ETH Zürich
[249] Guérout R, Jungen Ch, Oueslati H, Ross S C and Telmini M 2009 *Phys. Rev. A* **79** 042717
[250] Bethe H A and Salpeter E E 1957 *Quantum Mechanics of One- and Two-Electron Atoms* (Berlin: Springer)

[251] Slater J C 1960 *Quantum Theory of Atomic Structure* (New York: McGraw-Hill) vols. 1 and 2

[252] Cowan R D 1981 *The theory of atomic structure and spectra* (Berkeley: University of California Press)

[253] Slater J C 1951 *Phys. Rev.* **81** 385

[254] Herman F and Skillman S 1963 *Atomic Structure Calculations* (Englewood Cliffs, NJ: Prentice-Hall)

[255] Lahiri J and Manson S T 1986 *Phys. Rev. A* **33** 3151

[256] Klapisch M 1971 *Comput. Phys. Commun.* **2** 239

[257] Aymar M, Luc-Koenig E and Combet Farnoux F 1976 *J. Phys. B: At. Mol. Phys.* **9** 1279

[258] Clementi E and Roetti C 1974 *At. Data Nucl. Data Tables* **14** 177

[259] Chang T N 1975 *J. Phys. B: At. Mol. Phys.* **8** 743

[260] Laughlin C 1978 *J. Phys. B: At. Mol. Phys.* **11** 1399

[261] Duzy C and Hyman H A 1980 *Phys. Rev. A* **22** 1878

[262] Ojha P C and Burke P G 1983 *J. Phys. B: At. Mol. Phys.* **16** 3513

[263] Hansen J E 1972 *J. Phys. B: At. Mol. Phys.* **5** 1083

[264] Hansen J E 1973 *J. Phys. B: At. Mol. Phys.* **6** 1387

[265] Hansen J E 1973 *J. Phys. B: At. Mol. Phys.* **6** 1751

[266] Hansen J E 1973 *J. Phys. B: At. Mol. Phys.* **6** 1967

[267] Amusia M Ya and Cherepkov N A 1975 *Case Studies in Atomic Physics* vol 5 (Amsterdam: North-Holland) pp 49–179

[268] Amusia M Ya 1990 *Atomic Photoeffect* (New York: Plenum Press)

[269] Tsemekhman V, Tsemekhman K and Amusia M 1992 *Inst. Phys. Conf. Ser.* **128** 79

[270] Grant I P 1961 *Proc. R. Soc. Lond. A* **262** 555

[271] Desclaux J P 1975 *Comput. Phys. Commun.* **9** 31

[272] Liberman D A, Cromer D T and Waber J T 1971 *Comput. Phys. Commun.* **2** 107

[273] Walker T E H and Waber J T 1974 *J. Phys. B: At. Mol. Phys.* **7** 674

[274] Cherepkov N A 1978 *Phys. Lett. A* **66** 204

[275] Johnson W R and Cheng K T 1979 *Phys. Rev. A* **20** 978

[276] Johnson W R and Soff G 1983 *Phys. Rev. Lett.* **50** 1361

[277] Cowan R D and Griffin D C 1976 *J. Opt. Soc. Am.* **66** 1010

[278] Selvaraj V and Gopinathan M S 1984 *Phys. Rev. A* **29** 3007

[279] Born M and Heisenberg W 1924 *Z. Phys.* **23** 388

[280] Mayer J E and Mayer M G 1933 *Phys. Rev.* **43** 605

[281] Van Vleck J H and Whitelaw N G 1933 *Phys. Rev.* **44** 551

[282] Bates D R 1947 *Proc. R. Soc. London Ser. A* **188** 350

[283] Müller W, Flesch J and Meyer W 1984 *J. Chem. Phys.* **80** 3297

[284] Miculis K and Meyer W 2005 *J. Phys. B: At. Mol. Opt. Phys.* **38** 2097

[285] Weisheit J C 1972 *Phys. Rev. A* **5** 1621

[286] Norcross D W 1973 *Phys. Rev. A* **7** 606

[287] Aymar M 1978 *J. Phys. B: At. Mol. Phys.* **11** 1413

[288] Aymar M, Robaux O and Wane S 1984 *J. Phys. B: At. Mol. Phys.* **17** 993

[289] Bersuker I B 1957 *Optika i Spektroskopiya* **3** 97

[290] Hameed S, Herzenberg A and James M G 1968 *J. Phys. B: At. Mol. Phys.* **1** 822

[291] Clementi E 1965 *IBM J. Res. Develop.* **9** 2

[292] Hartree D R 1935 *Proc. R. Soc. London Ser. A* **151** 96

[293] Hartree D R 1934 *Proc. R. Soc. London Ser. A* **143** 506

[294] Yin Y Y and Elliott D S 1992 *Phys. Rev. A* **46** 1339

[295] Cook T B, Dunning F B, Foltz G W and Stebbings R F 1977 *Phys. Rev. A* **15** 1526

[296] Chang T N and Kim Y S 1982 *Phys. Rev. A* **26** 2728

[297] Sukhorukov V L, Lagutin B M, Petrov I D, Schmoranzer H, Ehresmann A and Schartner K H 1994 *J. Phys. B: At. Mol. Opt. Phys.* **27** 241

[298] Lagutin B M, Petrov I D, Sukhorukov V L, Whitfeld S B, Langer B, Viefhaus J, Wehlitz R, Berrah N, Mahler W and Becker U 1996 *J. Phys. B: At. Mol. Opt. Phys.* **29** 937

[299] Starace A F 1982 *Corpuscles and Radiation in Matter I* (*Encyclopedia of Physics* vol 31) ed W Mehlhorn (Berlin: Springer) pp 1–121

[300] Wright J D, Morgan T J, Li L, Gu Q, Knee J L, Petrov I D, Sukhorukov V L and Hotop H 2008 *Phys. Rev. A* **77** 062512

[301] Shore B W 1967 *Rev. Mod. Phys.* **39** 439

[302] Connerade J P 1998 *Highly Excited Atoms* (Cambridge: Cambridge University Press)

[303] Schmoranzer H, Ehresmann A, Vollweiler F, Sukhorukov V L, Lagutin B M, Petrov I D, Schartner K H and Möbus B 1993 *J. Phys. B: At. Mol. Opt. Phys.* **26** 2795

[304] Sobelman I I 1992 *Atomic Spectra and Radiative Transitions* (Berlin: Springer)

[305] Faust W L and McFarlane R A 1964 *J. Appl. Phys.* **35** 2010

[306] Fano U and Cooper J W 1968 *Rev. Mod. Phys.* **40** 441

[307] Sobelman I I 1972 *Introduction to the theory of atomic spectra* (Oxford: Pergamon Press)

[308] Jones R R and Gallagher T F 1988 *Phys. Rev. A* **38** 2846

[309] Moise A, Alagi M, Banchi L, Ferianis M, Prince K C and Richter R 2008 *Nucl. Instr. and Meth. in Phys. Res. A* **588** 502

[310] Li C, Wang T, Zhen J, Zhang Q and Chen Y 2009 *Sci. China Ser. B-Chem* **52** 161

[311] Lee Y Y 2010 private communication

[312] Lu C C, Carlson T A, Malik F B, Tucker T C and Nestor, Jr C W 1971 *Atomic Data* **3** 1

[313] Bates D R 1946 *Mon. Not. R. Astron. Soc.* **106** 432

[314] Seaton M J 1951 *Proc. R. Soc. London Ser. A* **208** 418

[315] Cooper J W 1962 *Phys. Rev.* **128** 681

[316] Cooper J W 1964 *Phys. Rev. Lett.* **13** 762

[317] Msezane A and Manson S T 1975 *Phys. Rev. Lett.* **35** 364

[318] Msezane A and Manson S T 1982 *Phys. Rev. Lett.* **48** 473

[319] Lahiri J and Manson S T 1982 *Phys. Rev. Lett.* **48** 614

[320] Avdonina N B and Amusia M Ya 1983 *J. Phys. B: At. Mol. Phys.* **16** L543

[321] Sandner W, Gallagher T F, Safinya K A and Gounand F 1981 *Phys. Rev. A* **23** 2732

[322] Suemitsu H and Samson J A R 1983 *Phys. Rev. A* **28** 2752

[323] Yin Y Y and Elliott D S 1992 *Phys. Rev. A* **54** 281

[324] Manson S T and Starace A F 1982 *Rev. Mod. Phys.* **54** 389

[325] Fink M G J and Johnson W R 1986 *Phys. Rev. A* **34** 3754

[326] Hyman H A 1977 *Appl. Phys. Lett.* **31** 14

[327] McCann K J and Flannery M R 1977 *Appl. Phys. Lett.* **31** 599

[328] Hazi A U and Rescigno T N 1977 *Phys. Rev. A* **16** 2376
[329] Hartquist T W 1978 *J. Phys. B: At. Mol. Phys.* **11** 2101
[330] Ranson P and Chapelle J 1979 *J. Phys. Colloques* **40** C7·25
[331] Pindzola M S 1981 *Phys. Rev. A* **23** 201
[332] Luke T M 1982 *J. Phys. B: At. Mol. Phys.* **15** 1217
[333] Chang T N 1982 *J. Phys. B: At. Mol. Phys.* **15** L81
[334] Petrov I, Sukhorukov V, Leber E and Hotop H 2000 *Eur. Phys. J. D* **10** 53
[335] Ganz J, Lewandowski B, Siegel A, Bussert W, Waibel H, Ruf M W and Hotop H 1982 *J. Phys. B: At. Mol. Phys.* **15** L485
[336] Leuchs G and Walther H 1984 *Multiphoton Ionization of Atoms*, eds S L Chin and P Lambropoulos (Toronto: Academic Press) pp 109–132
[337] Cowan R D 1967 *Phys. Rev.* **163** 54
[338] Klar H and Kleinpoppen H 1982 *J. Phys. B: At. Mol. Phys.* **15** 933
[339] Baier S, Grum-Grzhimailo A N and Kabachnik N M 1994 *J. Phys. B: At. Mol. Opt. Phys.* **27** 3363
[340] Pan C and Starace A F 1991 *Phys. Rev. A* **44** 324
[341] Trickl T, Vrakking M J J, Cromwell E, Lee Y T and Kung A H 1989 *Phys. Rev. A* **39** 2948
[342] Kopfermann H 1958 *Nuclear Moments* (New York: Academic Press)
[343] Witte S, Zinkstok R Th, Ubachs W, Hogervorst W and Eikema K S E 2005 *Science* **307** 400
[344] Zinkstok R Th, Witte S, Ubachs W, Hogervorst W and Eikema K S E 2006 *Phys. Rev. A* **73** 061801(R)
[345] Kandula D Z, Gohle Ch, Pinkert T J, Ubachs W and Eikema K S E 2010 *Phys. Rev. Lett.* **105** 063001
[346] Young L, Kanter E P, Krässig B, Li Y, March A M, Pratt S T, Santra R, Southworth S H, Rohringer N, DiMauro L F, Doumy G, Roedig C A, Berrah N, Fang L, Hoener M, Bucksbaum P H, Cryan J P, Ghimire S, Glownia J M, Reis D A, Bozek J D, Bostedt C and Messerschmidt M 2010 *Nature* **466** 56
[347] Fleischer A, Wörner H J, Arissian L, Liu L R, Meckel M, Rippert A, Dörner R, Villeneuve D M, Corkum P B and Staudte A 2011 *Phys. Rev. Lett.* **107** 113003
[348] Lépine F, Bordas Ch, Nicole C and Vrakking M J J 2004 *Phys. Rev. A* **70** 033417
[349] Vliegen E, Wörner H J, Softley T P and Merkt F 2004 *Phys. Rev. Lett.* **92** 033005
[350] Hogan S D, Motsch M and Merkt F 2011 *Phys. Chem. Chem. Phys.* **13** 18705
[351] Saloman E B and Sansonetti C J 2004 *J. Phys. Chem. Ref. Data* **33** 1113
[352] Mohr P J, Taylor B N and Newell D B 2008 *Rev. Mod. Phys.* **80** 633
[353] Chang E S, Schoenfeld W G, Biémont E, Quinet P and Palmeri P 1994 *Phys. Scr.* **49** 26
[354] Yamada C, Kanamori H and Hirota E 1985 *J. Chem. Phys.* **83** 552
[355] Velchev I, Hogervorst W and Ubachs W 1999 *J. Phys. B: At. Mol. Opt. Phys.* **32** L511
[356] Hollenstein U 2003 PhD thesis ETH Zürich
[357] Hollenstein U, Seiler R and Merkt F 2003 *J. Phys. B: At. Mol. Opt. Phys.* **36** 893
[358] Jackson D A 1979 *J. Opt. Soc. Am.* **69** 503
[359] Jackson D A 1980 *J. Opt. Soc. Am.* **70** 1139
[360] Cannon B D and Janik G R 1990 *Phys. Rev. A* **42** 397
[361] Keim M, Arnold E, Borchers W, Georg U, Klein A, Neugart R, Vermeeren L, Silverans R E and

Lievens P 1995 *Nucl. Phys. A* **586** 219
[362] Brandi F, Hogervorst W and Ubachs W 2002 *J. Phys. B: At. Mol. Opt. Phys.* **35** 1071
[363] Sommavilla M 2004 PhD thesis ETH Zürich
[364] Brandi F, Velchev I, Hogervorst W and Ubachs W 2001 *Phys. Rev. A* **64** 032505
[365] Sansonetti J E and Martin W C 2005 *J. Phys. Chem. Ref. Data* **34** 1559
[366] Ward, Jr R F, Sturrus W G and Lundeen S R 1996 *Phys. Rev. A* **53** 113
[367] Lee Y Y 2011 private communication
[368] Grosof G M, Buck P, Lichten W and Rabi I I 1958 *Phys. Rev. Lett.* **1** 214
[369] Faust W L and Chow Chiu L Y 1963 *Phys. Rev.* **129** 1214
[370] Faust W L and McDermott M N 1961 *Phys. Rev.* **123** 198
[371] Delsart C and Keller J C 1976 *Opt. Commun.* **16** 388
[372] Ducas T W, Feld M S, Ryan, Jr L W, Skribanowitz N and Javan A 1972 *Phys. Rev. A* **5** 1036
[373] Liberman S 1973 *Physica* **69** 598
[374] Husson X and Grandin J P 1977 *J. Phys. B: At. Mol. Phys.* **11** 1393
[375] Jackson D A 1977 *J. Opt. Soc. Am.* **67** 1638
[376] D'Amico G, Pesce G and Sasso A 1999 *Phys. Rev. A* **60** 4409
[377] Fraga S, Saxena K M S and Lo B W N 1971 *Atomic Data* **3** 323
[378] Barnes R G and Smith W V 1954 *Phys. Rev.* **93** 95

2344 ## Figures

Figure 1. Two-step $e^- + \lambda_i$ (a) and two-color $\lambda_e + \lambda_i$ (b) excitation schemes of the even-parity $np'[1/2, 3/2]_1$, $np'[3/2]_2$, and $nf'[5/2]_{2,3}$ ARS. Transitions to the nf' ARS, mediated by electron correlation effects, are indicated by dash-dotted arrows.

Figure 2. Two-photon resonance excitation scheme for accessing odd-parity ns', nd', and ng' ARS from metastable levels with $J_{ms} = 0$ $(\lambda_e + \lambda_i)$ and $J_{ms} = 2$ $(\lambda'_e + \lambda'_i)$ via the intermediate $mp^5(m+1)p$ $J = 1, 2, 3$ levels (the low-lying ground state is omitted; only two of the possible transitions from the metastable to the intermediate levels are shown). Transitions to the ng' ARS, mediated by electron correlation effects, are indicated by dash-dotted arrows.

Figure 3. Level diagram of Ne I [351]. The right panels present the levels of interest on enlarged scales (the quantum defects for the np' and nf' levels were taken from [62]). For the $2p^53p$ levels, the Paschen notation $2p_x$ $(x = 1 - 10)$ and $[K]_J$ quantum numbers in Racah coupling are given. The low-lying ground state is omitted. (Adapted from [74].)

Figure 4. Sketch of an experimental setup for photoionization spectroscopy of rare-gas atoms. (For details see text.)

Figure 5. Influence of the relativistic and many-electron effects on the 6s photoionization cross section of Cs. (a) Comparison between the cross sections computed without (HF [70]) and with (PF [70], DF [276]) inclusion of relativistic effects. The length gauge (L) is shown only for the PF approach. (b) Cross sections computed with inclusion of intershell correlations (CIPF [70]) and core polarization in addition (CIPFCP [72]); semiempirical calculation of Norcross (CP [286]) and experimental cross section (Exp. [295]); nonrelativistic RPAE calculation [267]. The velocity gauge (V) PF calculation from (a) is also shown in (b) for comparison.

Figure 6. Photoabsorption cross section of ground state Xe atoms between the $^2P_{3/2}$ and $^2P_{1/2}$ ionization thresholds measured with a bandwidth (FWHM) of 0.0074 Å (1 Å = 0.1 nm). (Adapted from [15] with permission.)

Figure 7. Comparison of the Rg $(ns'; J = 0)$ and Rg $(ns'; J = 1)$ autoionization resonances in the rare-gas atoms Rg = Ne–Xe, plotted on a common reduced energy scale $E_{\rm red} = (E - E_0) \cdot (n^*)^3$. In all cases, resonances with high q values were chosen. (Adapted from [40].)

Figure 8. Profiles of the Ne $(15d')$ line, consisting of a superposition of the $[3/2]_2$ and $[3/2]_1$ resonances, excited via the $2p_2$ level from the Ne $(3s, J = 2)$ metastable level with parallel linear laser polarizations. The smooth curves represent fitted Shore profiles. The residuals between the experimental data and the resulting fit sum (not shown) are displayed at the bottom of the figure (gray curve). The absolute cross-section scale (1 Gb = 10^{-19} m^2) is based on the results of CIPFCP calculations (see figure 8 in [74]). (Adapted from [74].)

Figure 9. Profiles of the Ne $(12d')$ lines, consisting of a superposition of the indicated resonances, excited via $2p_5$ and $2p_8$, respectively, from the Ne $(3s, J = 2)$ metastable level with parallel linear laser polarizations. The smooth curves represent fitted Shore profiles. The residuals between the experimental data and the resulting fit sum (not shown) are displayed at the bottom of the figures (gray curve). The absolute cross section scale is based on the results of CIPFCP calculations (see figure 3 and figure 8 in [74] for (a) and (b), respectively. Note that the cross section scale of (b) has to be multiplied by a factor of 1/6 with respect to that of (a). (Adapted from [74].)

Figure 10. Photoionization spectrum of argon atoms in the energy range of the $9g'[7/2]_4$ resonance, excited from the metastable Ar $(4s\ ^3P_2)$ level via the intermediate Ar $(4p[5/2]_3)$ level with parallel linear polarizations of the two anticollinear laser beams. The smooth curve represents a Beutler–Fano fit to the experimental data (open circles). (Adapted from [46].)

Figure 11. Comparison of the measured (a) and the calculated (b) autoionization spectrum in the region of the Ne $(13p'[1/2, 3/2]_1)$ resonances, excited from the metastable Ne $(2p^5\ 3s'\ ^3P_0)$ level. Both velocity and length gauges are shown for the computed spectra. The experimental cross section is normalized using theoretical results (length gauge) at the resonance maximum. (Adapted from [33].)

Figure 12. Comparison of the measured (a) and the calculated (b) autoionization spectrum in the region of the Ne $(13p',\ J = 1, 2)$ resonances, excited from the metastable Ne $(2p^5\ 3s\ ^3P_2)$ level. Both velocity and length gauges are shown for the computed spectra. The experimental cross section is normalized using theoretical results (length gauge) at the resonance maximum. (Adapted from [33].)

Figure 13. Photoionization spectra of neon following excitation from the $3s\ ^3P_1$ (a) and $3s'\ ^1P_1$ (b) intermediate levels. The spectra were obtained by monitoring the Ne^+ ion signal as a function of the frequency of the UV laser. The energy scale gives the spectral position with respect to the $^1S_0$ ground state of neon. Both spectra were obtained for a parallel arrangement of the polarization vectors of the VUV and UV beams. (Adapted from [62].)

Figure 14. Comparison between the measured (a) and the computed (b) resonance profiles of the Xe $(4f'[5/2]_2)$ ARS excited via the Xe $(5d[3/2]_1)$ intermediate state. The experimental cross section (bandwidth of ionizing laser 0.37 meV) is normalized using the theoretical results at the resonance maximum. Positions of the $4f'[K]_J$ resonances, which cannot be accessed via the $5d[3/2]_1$ intermediate level, are also shown. The energy scale is given with respect to the Xe^+ $(^2P_{1/2})$ ionization threshold. (Adapted from [58].)

Figure 15. Fano-profile fits (smooth curves) to the experimental data (gray curves; bandwidth of ionizing laser ≈ 0.2 cm^{-1}). (a) Xe $(4f'[7/2]_3)$ resonance excited from the Xe $(5d[5/2]_2)$ level. (b) Xe $(4f'[7/2]_4)$ resonance excited from the Xe $(5d[7/2]_3)$ level. (Adapted from [32] with permission.)

Figure 16. Comparison of the photoionization cross sections σ (in Mb $= 10^{-22}$ m^2) and PAD parameters β for ground state alkali-metal atoms, calculated within the CIPF (broken curves) and CIPFCP (solid curves) approximations (in velocity gauge), with previous results. Open symbols [a]–[d]: Experimental results from references [321], [322], [323] and [294], respectively. The dotted curves for the PAD parameters of Rb and Cs represent theoretical data from [323] and [294], calculated by the authors using results in [285] and [286], respectively. (Adapted from [72].)

Figure 17. Comparison of the partial photoionization cross sections σ (in Mb $= 10^{-22}$ m^2) and PAD parameters β, calculated within the CIPF and CIPFCP approximations (in velocity gauge), for the core-conserving transitions in the photoionization of metastable Rg $((m+1)s\,^3P_2)$ atoms (formation of $^2P_{3/2}$ ions). The experimental data (full circles with error bars) are from [69–71]. (Adapted from [72].)

Figure 18. Comparison of the partial photoionization cross sections σ (in Mb = $10^{-22}\,\mathrm{m}^2$) and PAD parameters β, calculated within the CIPF and CIPFCP approximations (in velocity gauge), for the core-conserving transitions in the photoionization of metastable Rg $((m+1)\mathrm{s}'\,^3\mathrm{P}_0)$ atoms (formation of $^2\mathrm{P}_{1/2}$ ions). The experimental data (full circles with error bars) are from [69–71]. (Adapted from [72].)

Figure 19. Comparison of the partial photoionization cross sections σ (in Mb = $10^{-22}\,\mathrm{m}^2$) and PAD parameters β, calculated within the CIPF and CIPFCP approximations (in velocity gauge), for the core-changing transitions in the photoionization of metastable Rg $((m+1)\mathrm{s}\,^3\mathrm{P}_2)$ atoms (formation of $^2\mathrm{P}_{1/2}$ ions). The experimental data (full circles with error bars) are from [69–71]. (Adapted from [72].)

Figure 20. Comparison of the partial photoionization cross sections σ (in Mb = $10^{-22}\,\mathrm{m}^2$) and PAD parameters β, calculated within the CIPF and CIPFCP approximations (in velocity gauge), for the core-changing transitions in the photoionization of metastable Rg $((m+1)\mathrm{s}'\,^3\mathrm{P}_0)$ atoms (formation of $^2\mathrm{P}_{3/2}$ ions). The experimental data (full circles with error bars) are from [69–71]. Note, that the cross section scales for Ar, Kr, and Xe have to be multiplied by factors of 4, 20, and 400, respectively. (Adapted from [72].)

Figure 21. Illustration of the energy structure of the four lowest excited levels of Rg = Ne–Xe associated with the configurations $m\mathrm{p}^5(J^+)(m+1)\mathrm{s}$ and $m\mathrm{p}^5(J^+)m\mathrm{d}$ (for Ne: $m\mathrm{p}^5(J^+)(m+1)\mathrm{d}$) as obtained neglecting the Coulomb interaction between the configurations (indicated by the CI matrix element). Very strong s–d mixing is present for Xe $(6\mathrm{s}'[1/2]_0)$ and Xe $(5\mathrm{d}'[1/2]_0)$. (Adapted from [71].)

Figure 22. Lineshapes of the autoionizing Rydberg states $3p^5(^2P_{1/2})$ 12s′, 10d′, and 10g′ of Ar, accessed from the isotropic $2p_{2-4}$ and $2p_{6-10}$ intermediate levels. Note that the cross-section scales of the right panels ($2p_3$, $2p_6$, $2p_8$, and $2p_9$) have to be multiplied by factors of 2, 1/2, 1/2, and 1/8 with reference to the respective left panels. (Adapted from [75].)

Figure 23. Lineshapes of selected ARS of Ar, Kr and Xe, excited from the $2p_1$ $(m+1)p'[1/2]_0$ level (upper panels) and $2p_5$ $(m+1)p[1/2]_0$ level (lower panels). Note that the cross-section scales of the lower panels for Kr and Xe have both to be multiplied by a factor of 1/12 with respect to the left panel (Ar). (Adapted from [75].)

Figure 24. Comparison between the computed ((a), (c)) and measured ((b), (d)) lineshapes of odd-parity ARS in Kr, excited from the $2p_3$ ((a), (b)) and $2p_4$ ((c), (d)) intermediate levels with total angular momentum $J = 1$. The theoretical spectra are convolutions with a Gaussian of FWHM 1.0 cm^{-1}. The lineshapes are displayed as a function of $-\mu$, i.e., a negative quantum defect, used as a common energy variable for different principal quantum numbers. (Adapted from [75].)

Figure 25. Comparison between the computed ((a), (c)) and measured ((b), (d)) lineshapes of odd-parity ARS in Kr, excited from the $2p_2$ ((a), (b)) and $2p_8$ ((c), (d)) intermediate levels with total angular momentum $J = 2$. The theoretical spectra are convolutions with a Gaussian of FWHM 1.0 cm^{-1}. The lineshapes are displayed as a function of $-\mu$, i.e., a negative quantum defect, used as a common energy variable for different principal quantum numbers. (Adapted from [75].)

Figure 26. Comparison between the computed ((a), (c)) and measured ((b), (d)) lineshapes of odd-parity ARS in Kr, accessed from the metastable $1s_5$ $5s[3/2]_2$ level via the $2p_9$ $5p[5/2]_3$ intermediate level. (a), (b): Data for perpendicular laser polarizations. (c), (d): Data for parallel laser polarizations. The uncertainty in the absolute scale of the experimental cross sections is estimated to be ±25% [201]. (Adapted from [75].)

Figure 27. Comparison between experimental (a) and computed (b) resonance profiles of the Xe $(nf'[5/2]_2)$ and Xe $(11p'[K]_J)$ ARS excited via the Xe $(6d[3/2]_1)$ intermediate level in a two-photon two-colour experiment. The experimental cross section is normalized to theoretical results at the maximum of the Xe $(7f'[5/2]_2)$ resonance. The energy scale is given with respect to the Xe^+ $(^2P_{1/2})$ ionization threshold. (Adapted from [58].)

Figure 28. Comparison between measured (right panels) and computed (left panels) photoionization cross sections for unpolarized (a) $4s'[1/2]_1$, (b) $5s[3/2]_1$ and (c) $5s'[1/2]_1$ levels of Ar. The experimental data for $5s'[1/2]_1$ are from [60]. The cross sections are displayed as a function of $-\mu$, i.e., a negative quantum defect, used as a common energy variable for different principal quantum numbers. (Adapted from [64].)

Figure 29. (a) Cross sections for the $4s'[1/2]_1 \rightarrow (n/\epsilon)p'[K]_{1,2}$ transitions (the full curves represent spline fits connecting the data points, computed at discrete bound energies and a grid of continuum energies). (b)–(e) n-dependence of the lineshapes for the $4s'[1/2]_1 \rightarrow np'$ transitions in the vicinity of the Seaton–Cooper minima. The lineshapes are displayed as a function of $-\mu$, i.e., a negative quantum defect, used as a common energy variable for different principal quantum numbers. (Adapted from [64].)

Figure 30. Influence of s–d mixing in Kr on the $6s[3/2]_1 \rightarrow 8f'[5/2]_2$ (left panels) and $4d[3/2]_1 \rightarrow 8f'[5/2]_2$ spectra (right panels). The upper panels show the experimental spectra shifted to the calculated resonance position; the resonance is broadened by the ionizing bandwidth 0.16 meV. The middle panels present the cross sections calculated with 'pure' $6s[3/2]_1$- and $4d[3/2]_1$-states. The bottom panels show the cross sections calculated with inclusion of the interaction between the $4p^5(^2P_{3/2})6s$- and $4p^5(^2P_{3/2})4d$-configurations. (Adapted from [34].)

Figure 31. Experimental ((a), (c)) and theoretical ((b), (d)) results for photoionization of Xe $(6s'\ ^3P_0)$ atoms in the range of the Xe $(7p',\ J = 1)$ ARS. (a) Photoion yield (open circles) compared with the sum of two independent Beutler–Fano profiles (smooth line) fitted to the experimental data. (c) Measured PAD parameters β; open circles with error bars indicate experiments for which the angular distribution was fully determined, closed circles indicate β values which were obtained from electron intensity measurements at the two angles $\theta = 0°$ and $\theta = 90°$, respectively. (b) Theoretical photoionization cross section. (d) Energy dependence of the PAD parameters β, calculated separately for the $7p'[3/2]_1$ resonance (dotted curve) and the $7p'[1/2]_1$ resonance (broken curve), and of the "composed" PAD parameter $\beta_c(E)$ (full curve) to be compared with the experimental values (for details see [31]). For easier comparison with the experimental data, the experimental energy scale has been adopted in (b) and (d) by using the experimental resonance energies. (Adapted from [31].)

Figure 32. Theoretical and experimental PAD parameters β_2 (open squares) and β_4 (open circles) for photoionization of the aligned (a) Ne $(3d'[3/2]_1)$ and (b) Ne $(3d[3/2]_1)$ states. The experimental values are extracted from the measured PADs, whereas the theoretical values (β_2: solid curves; β_4: broken curves) were obtained with a quantum defect treatment (see [186]). The polar plots illustrate the experimental angular distributions measured at photoelectron kinetic energies of 33 meV (a) and 45 meV (b). (Adapted from [186] with permission.)

Figure 33. Calculated relevant phase differences Δ_{ik} and ratios of reduced dipole matrix elements $\nu_{ik} \equiv d_{ik}/d_{12}$ between the five d-wave channels and the s-wave channel (d_{12}) for photoionization of Ar $(4p[5/2]_3)$ atoms to the Ar^+ $(^2P_{3/2})$ ion state over the electron energy range 0–2 eV. The calculations include the term dependence and important many-electron correlations as well as long-range core polarization effects. (Adapted from [184].)

Figure 34. Comparison of PADs $I(\theta;\alpha$ fixed) (left panels: $\alpha = 0°$; right panels: $\alpha = 90°$) for photoionization of laser-excited, polarized Ar $(4p[5/2]_3)$ atoms with three different theoretical predictions (θ is the angle between the momentum of the photoelectron and the electric-field vector of the ionizing light; α is the angle between the electric-field vectors of the exciting and ionizing linearly-polarized lasers). Open circles: experimental data; dotted curves: theory with dynamical parameters computed without inclusion of long-range core polarization; broken curves: theory with dynamical parameters computed with inclusion of long-range core polarization (see figure 33); full curves: theory with dynamical parameters based on those in figure 33, but with modified values of ν_{ik} (see text and [184]). (Adapted from [184].)

Figure 35. Schematic representation of spin–orbit and hyperfine autoionization processes for different xenon isotopes. The hyperfine levels of the $^2P_{3/2}$ and $^2P_{1/2}$ states of $^{131}Xe^+$ and $^{129}Xe^+$ are labeled with the quantum number F^+. Dark grey bars are closed channels representing series of discrete Rydberg states and light grey bars are open channels, i.e., the adjoining continua. Spin–orbit autoionization processes are indicated by full arrows, hyperfine autoionization processes by dashed arrows. The spin–orbit splitting (10 536.9 cm^{-1}) is $10^4 - 10^5$ times larger than the hyperfine splittings (e.g., 0.10985(1) cm^{-1} for $^{129}Xe^+$ $^2P_{3/2}$ [237] and 0.4071(9) cm^{-1} for $^{129}Xe^+$ $^2P_{1/2}$ [21]).

Figure 36. Comparison between experimental and calculated spectra of the 39d′ and 41s′ Rydberg states of (a) ^{132}Xe, (b) ^{131}Xe, and (c) ^{129}Xe excited from the $5p^6$ $^1S_0$ ground state. (Adapted from [21].)

Figure 37. Hyperfine structure of autoionizing Rydberg states of ^{83}Kr excited from the $4p^6$ $^1S_0$ ground state. Panels (a)–(c) show the hyperfine structure of nd′ and $(n + 2)$s′ Rydberg states for $n = 41$, 51, and 73, respectively. The double arrows indicate the magnitude of the hyperfine splitting of the $^2P_{1/2}$ state of $^{83}Kr^+$. (Adapted from [22].)

Figure 38. Stroboscopic resonances arising from the hyperfine structure in the ARS of ^{83}Kr (top), ^{131}Xe (middle), and ^{129}Xe (bottom) [21,22]. In each panel, the theoretical spectrum from MQDT calculations is presented above the experimental spectrum. The positions of the stroboscopic resonances k can be located from the rulers, which show the positions of the hypothetical unperturbed $n\mathrm{d}'[3/2]_1$ resonances converging to the lower (with n labels) and upper hyperfine levels of the $^2\mathrm{P}_{1/2}$ ionic state [calculated with the quantum defects $\mu_\mathrm{d}(\mathrm{Kr}) = 1.243$ and $\mu_\mathrm{d}(\mathrm{Xe}) = 2.333$].

Figure 39. Hyperfine structure of the $n\mathrm{s}[3/2]_{1,2}$ ($37 \leq n \leq 152$) Rydberg states of ^{83}Kr and of the $^2\mathrm{P}_{3/2}$ state of $^{83}\mathrm{Kr}^+$ as derived from the MQDT analysis of [236]. The $F = 11/2$ levels are highlighted by the solid black curves. For $n > 60$, avoided crossings resulting from interactions between ns and $(n-2)$d hyperfine levels can be observed. One of these avoided crossings, between the $F = 11/2$ hyperfine levels of the $n\mathrm{s}[3/2]_2$ and $(n-2)\mathrm{d}[3/2]_1$ states and marked with a box, has been studied at high resolution with millimetre wave spectroscopy; in the inset, the experimental values are indicated by circles, and lines connect the calculated level positions. For $n > 120$, the hyperfine levels mix with those of the next higher or lower n, indicated by the broad dashed lines representing the lowest $F = 11/2$ level of $(n-1)\mathrm{d}/(n+1)\mathrm{s}$ and the highest $F = 11/2$ level of $(n-3)\mathrm{d}/(n-1)\mathrm{s}$, respectively.

2345 ## Tables

Table 1. First and second ionization energies[a] $E_\mathrm{i}(^2\mathrm{P}_{3/2})$ and $E_\mathrm{i}(^2\mathrm{P}_{1/2})$ and spin-orbit splittings $A_\mathrm{so} = [E_\mathrm{i}(^2\mathrm{P}_{1/2}) - E_\mathrm{i}(^2\mathrm{P}_{3/2})]/hc$ of the rare-gas atoms Ne, Ar, Kr and Xe.

	$E_\mathrm{i}(^2\mathrm{P}_{3/2})/hc$ (cm^{-1})	$E_\mathrm{i}(^2\mathrm{P}_{1/2})/hc$ (cm^{-1})	A_so (cm^{-1})
Ne	173929.7726(6)[b]	174710.1966(11)[c]	780.4240(11)[d]
Ar	127109.842(4)[e]	128541.425(4)[c]	1431.5831(7)[d]
Kr	112914.434(16)[f]	118284.728(44)[g]	5370.294(44)[g]
Xe	97833.790(11)[h]	108370.714(16)[i]	10536.925(19)[i]

[a] Conversion factor 1 eV/hc = 8065.54465(20) cm^{-1} [352].

[b] From Chang *et al* [353].

[c] Calculated with the values of $E_\mathrm{i}(^2\mathrm{P}_{3/2})/hc$ and A_so.

[d] From Yamada *et al* [354].

[e] From Velchev *et al* [355]. The isotope shifts for ^{36}Ar and ^{38}Ar with respect to ^{40}Ar are −0.0939(22) cm^{-1} and −0.0463(25) cm^{-1}, respectively [356].

[f] Value for ^{84}Kr from Hollenstein *et al* [357], where the values for the other stable isotopes except ^{83}Kr are given as well. The isotope shift of ^{83}Kr has been reevaluated based on the isotope shifts of low-n levels above 100 000 cm^{-1} [118, 341, 358–363] and data of the $ns\,[3/2]_1$ Rydberg series with well-resolved hyperfine structure for $n \leq 40$ [235] (the $F = 11/2$ hyperfine level of the $ns\,[3/2]_1$ Rydberg series appears to be disturbed by the adjacent $ns\,[3/2]_2$ $F = 11/2$ hyperfine levels for $n > 40$, see figure 39); the obtained isotope shift of −0.0038(10) cm^{-1} with respect to the ^{84}Kr ionization limit is larger than that obtained by Wörner *et al* [235] (−0.0020(8) cm^{-1}).

[g] Value for ^{84}Kr from Paul *et al* [22], where the values for the other stable isotopes are also reported.

[h] Value for ^{132}Xe from Brandi *et al* [364], where the values for the other stable isotopes are also reported.

[i] Value for ^{132}Xe from Wörner *et al* [21], where the values for other isotopes are also reported.

Table 2. Characteristics of the metastable rare-gas atoms.

	State		E^a/hc (cm^{-1})	Radiative lifetime τ (s)
Ne	$2p^5\,3s'[1/2]_0$	$^3P_0$	134 818.6405	430.0^b
	$2p^5\,3s[3/2]_2$	$^3P_2$	134 041.8400	$24.4^b,\ 14.73 \pm 0.14^c$
Ar	$3p^5\,4s'[1/2]_0$	$^3P_0$	94 553.6705	44.9^b
	$3p^5\,4s[3/2]_2$	$^3P_2$	93 143.7653	$55.9^b,\ 38^{+8}_{-5}{}^d$
Kr	$4p^5\,5s'[1/2]_0$	$^3P_0$	85 191.6171	0.488^b
	$4p^5\,5s[3/2]_2$	$^3P_2$	79 971.7422	$85.1^b,\ 39^{+5}_{-4}{}^d,\ 28.3\pm1.8^e$
Xe	$5p^5\,6s'[1/2]_0$	$^3P_0$	76 196.767	$0.0782^b,\ 0.128^{+0.122}_{-0.042}{}^f$
	$5p^5\,6s[3/2]_2$	$^3P_2$	67 067.547	$149.5^b,\ 42.9 \pm 0.9^g$

[a] Level energy relative to the $mp^6\ ^1S_0$ ground state [365]. Conversion factor 1 eV/hc = 8065.54465(20) cm^{-1} [352].

[b] Calculated lifetime [129].

[c] Experimental lifetime [91].

[d] Experimental lifetime [79].

[e] Experimental lifetime [92].

[f] Experimental lifetime [93].

[g] Experimental lifetime [80].

Table 3. Two-photon transitions in rare gases and spectral ranges where the tunable VUV radiation can be produced by resonance-enhanced four-wave mixing $\tilde{\nu}_{\rm VUV} = 2\tilde{\nu}_1 \pm \tilde{\nu}_2$ [a]

	Transition	$2\tilde{\nu}_1$ (cm^{-1})	$2\tilde{\nu}_1 - \tilde{\nu}_2$ (cm^{-1})	$2\tilde{\nu}_1 + \tilde{\nu}_2$ (cm^{-1})
Xe	$5p^5 6p[1/2]_0 \leftarrow 5p^6\,(^1S_0)$	80 118.962(3)[b]	≤76 800	92 200–142 000
	$5p^5 6p'[1/2]_0 \leftarrow 5p^6\,(^1S_0)$	89 860.015(3)[b]		
Kr	$4p^5 5p[1/2]_0 \leftarrow 4p^6\,(^1S_0)$	94 092.8632(14)[c]	≤86 700	107 000–151 000
	$4p^5 5p'[1/2]_0 \leftarrow 4p^6\,(^1S_0)$	98 855.0703(14)[c]		
Ar	$3p^5 4p[1/2]_0 \leftarrow 3p^6\,(^1S_0)$	107 054.2773(30)[d,e]	55 000–96 000	121 500–161 000
	$3p^5 4p'[1/2]_0 \leftarrow 3p^6\,(^1S_0)$	108 722.6247(30)[d,e]		

[a] Tuning range of variable frequency laser $\tilde{\nu}_2$: 13 000 – 52 000 cm^{-1} (770 – 190 nm) .

[b] Value for the isotopic center of gravity of natural Xe [365].

[c] Value for the most abundant isotope ^{84}Kr [365].

[d] Value for the most abundant isotope ^{40}Ar [365].

[e] $\tilde{\nu}_1 + \tilde{\nu}_1'$ where $\tilde{\nu}_1' = 63\,439.322(40)$ cm^{-1} (157.6 nm F_2 excimer line) [111].

Table 4. (a) Reduced widths Γ_r (cm^{-1}) and quantum defects μ_ℓ for Ne.

$n\ell'$	$K' = \ell' - 1/2$				$K' = \ell' + 1/2$			
	$J = \ell' - 1$		$J = \ell'$		$J = \ell'$		$J = \ell' + 1$	
	Γ_r	μ_ℓ	Γ_r	μ_ℓ	Γ_r	μ_ℓ	Γ_r	μ_ℓ
20s′ [a]					*129*	*1.286*	*355*	*1.276*
14s′ [b]					158	1.3091	298	1.3008
ns′ [c]					**121(3)**	**1.3150**	**371(10)**	**1.3049**
					14 [d]	14 [d]	14–24 [d]	14 [e]
20p′ [a]	*3355*	*0.745*	*1804*	*0.816*	*168*	*0.816*	*191*	*0.810*
13p′ [b]	6431	0.7634	2620	0.8397	249	0.8394	264	0.8317
np′ [c]	**5334(130)**	**0.768(2)**	**2550(150)**	**0.8403(8)**	**280(25)**	**0.8381(6)**	**300(40)**	**0.8301(7)**
	13 [f]	13 [f]	13–15 [g]	13–15 [g]	13–15 [g]	13–15 [g]	13 [f,g]	13–15 [g,i]
20d′ [a]	*156*	*0.0039*	*313*	*0.0084*	*73*	*0.0084*	*66*	*0.0077*
12d′ [b]	186	0.0123	359	0.0165	87	0.0169	81	0.0164
nd′ [c]	**167(7)**	**0.0155(2)**	**350(7)**	**0.0200(4)**	**87(2)**	**0.0196** [j]	**73(3)**	**0.0192** [j]
	15 [e]	15 [e]	15 [e]	15 [e]	12 [e]	12 [e]	12 [e]	12 [e]
20f′ [a]	*23.2*	*0.0001*	*23.6*	*0.0001*	*9.64*	*0.0001*	*9.61*	*0.0001*
12f′ [b]	20.32	0.00156	20.61	0.00158	8.69	0.00161	8.74	0.00163
nf′ [c]		**0.0023(9)**		**0.0008(4)**				
		12 [h,i]		12 [f]				
20g′ [a]	*4.3*	5.5×10^{-4} [k]	*4.3*		*2.2*		*2.2*	
20h′ [a]	*1.1*	2.0×10^{-4} [k]	*1.1*		*0.65*		*0.65*	

[a] Pauli–Fock calculations for $20\ell'$ levels [76], in italics.

[b] Configuration interaction Pauli–Fock with core polarization (CIPFCP) calculations. Values for $\ell' = 1, 3$ from [34, 62], for $\ell' = 0, 2$ from [74].

[c] Recommended experimental data in bold font (in part averaged values from several experiments with estimated uncertainty are given). The numbers in the respective second line quote the (range of) principal quantum number n of the measured resonances.

[d–i] References: [d] [40], [e] [42], [f] [62], [g] [33], [h] [309], [i] Hollenstein, evaluation of spectra in [62].

[j] Value from MQDT analysis.

[k] Estimate using $\mu_{\ell,n} = \frac{2\left[3-\ell(\ell+1)/n^2\right]}{\ell(\ell+1)(2\ell-1)(2\ell+1)(2\ell+3)} \cdot \alpha_\mathrm{d}$ [209] with the dipole polarizability of the ion core in a.u. ($\alpha_\mathrm{d}\left(\mathrm{Ne}^+\right) = 1.3028(13)$ a.u.) [366].

Table 4. (b) Reduced widths $\Gamma_{\rm r}$ ($\rm cm^{-1}$) and quantum defects μ_ℓ for Ar.

$n\ell'$	$K'=\ell'-1/2$				$K'=\ell'+1/2$			
	$J=\ell'-1$		$J=\ell'$		$J=\ell'$		$J=\ell'+1$	
	$\Gamma_{\rm r}$	μ_ℓ	$\Gamma_{\rm r}$	μ_ℓ	$\Gamma_{\rm r}$	μ_ℓ	$\Gamma_{\rm r}$	μ_ℓ
20s′ [a]					*2344*	*2.089*	*1587*	*2.077*
12s′ [b]					1188	2.134	392	2.123
ns′ [c]					**820(50)** 11–25[d,e]	**2.148(2)** 11–25[e]	**510(20)** 11–25[d,e]	**2.137(1)** 11–25[e]
20p′ [a]	*2204*	*1.564*	*3678*	*1.635*	*385*	*1.635*	*386*	*1.627*
14p′ [b]	4507	1.599	4287	1.674	481	1.677	447	1.667
np′ [c]	**3980(400)** 11–15[f,g]	**1.615(1)** 11–16[g,h]	**3300(400)** 11–16[h,i,j]	**1.684(2)** 11–14[i,j]	**440(120)** 11–16[h,j]	**1.687(1)** 11–16[h,j]	**340(40)** 11,15[g,j]	**1.6765(1)** 11–16[g,j]
20d′ [a]	*13330*	*0.059*	*22760*	*0.205*	*4880*	*0.205*	*4601*	*0.168*
10d′ [b]	12916	0.194	30358	0.359	8045	0.364	9501	0.312
nd′ [c]	**28800(900)** 21–24[k]	**0.207(3)** 21–24[k]	**26000(1000)** 10,12,13[l,m]	**0.355(12)** 10,12,13[l,m]	**5000(100)** 10,14[l,m]	**0.350(9)** 10,14[l,m]	**7150(200)** 10,11[l,m]	**0.314(8)** 10,11[l,m]
20f′ [a]	*191.4*	*0.0005*	*205.8*	*0.0009*	*79.1*	*0.0009*	*77.9*	*0.0008*
9f′ [b]	181.8	0.00769	192.0	0.00792	80.9	0.00832	79.0	0.00824
nf′ [c]	**155(20)** 13,14[g]	**0.0111(1)** 13,14[g]	**162(5)** 9,10[n]	**0.0113(1)** 9,10[n]				**0.010(5)** 10–15[f]
20g′ [a]	*33.9*	2.3×10^{-3} [o]	*34.0*		*17.6*		*17.6*	
ng′ [c]	**26.9(6)** 11[p]	**0.004(3)** 11[p]	**27.7(14)** 9[q]	**0.00272(4)** 9[q]				
20h′ [a]	*7.8*	0.8×10^{-3} [o]	*7.8*		*5.6*		*5.6*	

[a] Pauli–Fock calculations for $20\ell'$ levels [76], in italics.

[b] Configuration interaction Pauli–Fock with core polarization (CIPFCP) calculations. Values for $\ell'=1,3$ from [34]; the values for $\ell'=0,2$ were obtained in [75], but not listed there (see also [77]).

[c] See footnote *c* in table 4(a) for Ne.

[d–n,p–q] References: [d] [40], [e] [43], [f] [55], [g] [64], [h] [60], [i] [33], [j] [300], [k] [20], [l] [132], [m] [45], [n] [34], [p] [41], [q] [46].

[o] Estimate using formula given in footnote *k* of table 4(a) for Ne and $\alpha_{\rm d}\left(\rm Ar^+\right)\approx\alpha_{\rm d}\left(\rm K^+\right)=$ 5.33 a.u. [285].

Table 4. (c) Reduced widths $\Gamma_{\rm r}$ ($\rm cm^{-1}$) and quantum defects μ_ℓ for Kr.

$n\ell'$	$K'=\ell'-1/2$				$K'=\ell'+1/2$			
	$J=\ell'-1$		$J=\ell'$		$J=\ell'$		$J=\ell'+1$	
	$\Gamma_{\rm r}$	μ_ℓ	$\Gamma_{\rm r}$	μ_ℓ	$\Gamma_{\rm r}$	μ_ℓ	$\Gamma_{\rm r}$	μ_ℓ
20s′ [a]					*3774*	*3.037*	*2752*	*3.024*
9s′ [b]					2510	3.091	805	3.081
ns′ [c]					**2245(100)**	**3.110(1)**	**1185(30)**	**3.099(1)**
					8^d	8^d	8^d	8^e
20p′ [a]	*1924*	*2.492*	*3960*	*2.565*	*691*	*2.565*	*671*	*2.557*
14p′ [b]	3838	2.547	3886	2.607	795	2.619	597	2.602
np′ [c]	**3800(400)**	**2.558(4)**	**2900(150)**	**2.613(3)**	**<1900**	**2.628(3)**	**600(150)**	**2.607(3)**
	8–$12^{f,g}$	8–10^f	12–14^h	12–14^h	12–14^h	12–14^h	12–$14^{g,h}$	12–14^h
20d′ [a]	*22860*	*1.074*	*20458*	*1.238*	*5092*	*1.238*	*5043*	*1.200*
7d′ [b]	18472	1.226	18257	1.346	5588	1.367	5955	1.322
nd′ [c]	**22460(220)**	**1.223(3)**	**13960(320)**	**1.341(2)**	**4030(60)**	**1.3515(15)**	**4630(160)**	**1.315(1)**
	$6^{i,j}$	$6^{i,j}$	6^j	6^j	6^j	6^j	6^j	6^j
20f′ [a]	*286*	*0.0012*	*329*	*0.0019*	*154*	*0.0019*	*150*	*0.0017*
11f′ [b]	251.8	0.0132	284.3	0.0138	151.2	0.0147	146.1	0.0144
nf′ [c]	**301(20)**	**0.015(3)**		**0.015(2)**				**0.012(4)**
	8^g	5–$14^{f,k}$		5–14^l				5–8^f
20g′ [a]	*39.7*	3.8×10^{-3} [m]	*39.5*		*46.8*		*46.8*	
5g′ [a]	*17.5*	2.9×10^{-3} [m]	*17.5*		*42.4*		*42.4*	
ng′ [c]	**< 36**	**0.003(2)**						
	5^n	5–16^n						
20h′ [a]	*6.05*	1.4×10^{-3} [m]	*6.05*		*18.3*		*18.3*	
6h′ [a]	*1.79*	1.0×10^{-3} [m]	*1.79*		*10.6*		*10.6*	

[a] Pauli–Fock calculations for $20\ell'$ levels or other $n\ell'$ levels as specified [76], in italics.

[b] Configuration interaction Pauli–Fock with core polarization (CIPFCP) calculations. Values for $\ell'=1,3$ from [34]; the values for $\ell'=0,2$ were obtained in [75], but not listed there.

[c] See footnote *c* in table 4(a) for Ne.

[d–l,n] References: [d] [40], [e] [15], [f] [55], [g] [34], [h] [33], [i] [14], [j] [47], [k] [367], [l] [310], [n] [53].

[m] Estimate using formula given in footnote *k* of table 4(a) for Ne and $\alpha_{\rm d}\left(\rm Kr^+\right)\approx\alpha_{\rm d}\left(\rm Rb^+\right)=$ 8.98 a.u. [285].

Table 4. (d) Reduced widths $\Gamma_{\rm r}$ ($\rm cm^{-1}$) and quantum defects μ_ℓ for Xe.

$n\ell'$	$K'=\ell'-1/2$				$K'=\ell'+1/2$			
	$J=\ell'-1$		$J=\ell'$		$J=\ell'$		$J=\ell'+1$	
	$\Gamma_{\rm r}$	μ_ℓ	$\Gamma_{\rm r}$	μ_ℓ	$\Gamma_{\rm r}$	μ_ℓ	$\Gamma_{\rm r}$	μ_ℓ
20s′ [a]					*2082*	*3.943*	*3116*	*3.929*
10s′ [b]					1148	4.006	676	3.997
ns′ [c]					**1105(25)** 9[d]	**4.031(2)** 9[e]	**848(15)** 9[d]	**4.021(2)** 9[e]
20p′ [a]	*1856*	*3.399*	*4030*	*3.476*	*1711*	*3.476*	*1663*	*3.468*
8p′ [b]	3197	3.504	3627	3.541	1424	3.571	1140	3.540
np′ [c]			**2955(25)** 7[f]	**3.5684(2)** 7[f]	**1163(12)** 7[f]	**3.6039(2)** 7[f]	**1090(80)** 7[g]	**3.5654(2)** 7[g]
	2900(200) 8[h]	**3.522** 8[h]	**2680(100)** 8[i,j]	**3.5522(7)** 8[i,j]	**1050(100)** 8[i,j]	**3.5910(8)** 8[i,j]	**950(80)** 8[h]	**3.551(2)** 8[h,k]
20d′ [a]	*51015*	*2.114*	*16277*	*2.335*	*4620*	*2.335*	*5473*	*2.291*
8d′ [b]	35398	2.316	9308	2.448	3068	2.474	3796	2.423
nd′ [c]	**35000(900)** 8–14[l]	**2.328(5)** 8–14[l]	**10400(1500)** 7–9[m]	**2.458(3)** 7–13[e,m]	**2250(150)** 7–9[m]	**2.474(2)** 7–13[e,m]	**2930(420)** 8–14[n]	**2.433(2)** 7–13[e,m]
20f′ [a]	*429*	*0.0034*	*593*	*0.0057*	*418*	*0.0057*	*399*	*0.0050*
4f′ [b]	216	0.0167	272	0.0176	375	0.0186	364	0.0183
nf′ [c]	**210(20)** 4[o]	**0.0240(6)** 4[o]	**300(60)** 4,5[i,j]	**0.027(2)** 4,5[i]	**250(30)** 4[g]	**0.025** 4[g]	**250(30)** 4[g]	**0.025** 4[g]
20g′ [a]	*49.7*	8.1×10^{-3} [p]	*48.6*		*116.0*		*115.9*	
5g′ [a]	*17.5*	6.1×10^{-3} [p]	*17.2*		*69.0*		*69.0*	
ng′ [c]	**71(14)** 5[n]	**0.006(3)** 5[n]						
20h′ [a]	*5.05*	2.9×10^{-3} [p]	*5.06*		*30.6*		*30.6*	
6h′ [a]	*1.154*	2.1×10^{-3} [p]	*1.155*		*10.44*		*10.44*	

[a] Pauli–Fock calculations for $20\ell'$ levels or other $n\ell'$ levels as specified [76], in italics.

[b] Configuration interaction Pauli–Fock with core polarization (CIPFCP) calculations. Values for $\ell'=1,3$ from [34]; the values for $\ell'=0,2$ were obtained in [75], but not listed there (see also [48]).

[c] See footnote *c* in table 4(a) for Ne.

[d–o] References: [d] [40], [e] [39], [f] [31], [g] [32], [h] [59], [i] [26], [j] [34], [k] [55], [l] [15], [m] [48], [n] [53], [o] [58].

[p] Estimate using formula given in footnote *k* of table 4(a) for Ne and $\alpha_{\rm d}\left(\rm Xe^+\right)\approx\alpha_{\rm d}\left(\rm Cs^+\right)=$ 19.1 a.u. [285].

Table 5. Experimentally determined hyperfine structures of the Rg* $mp^5(m{+}1)s$ and Rg^+ mp^5 states.

State		^{21}Ne ($I = 3/2$)	^{83}Kr ($I = 9/2$)	^{129}Xe ($I = 1/2$)	^{131}Xe ($I = 3/2$)
$ns[3/2]_2$	A (MHz)	$-267.68(3)^a$	$-243.9693(2)^b$	$-2384.5031(4)^c$	$706.4742(2)^c$
($1s_5$)	B (MHz)	$-111.55(10)^a$	$-452.1697(36)^b$	—	$252.5263(6)^c$
$ns[3/2]_1$	A (MHz)	$-460(4)^d$	$-160.4(6)^e$	$-959.1(7)^f$	$284.3(6)^f$
($1s_4$)	B (MHz)	$+33(8)^d$	$-105.8(30)^e$	—	$89.8(8)^f$
$ns'[1/2]_1$	A (MHz)	-658^g	$-739.6(5)^e$	$-5808(2)^f$	$1709.3(7)^f$
($1s_2$)	B (MHz)	^{g}	$-111.5(30)^e$	—	$30.3(8)^f$
$Rg^+\,{}^2P_{3/2}$	A (MHz)	^{h}	$-198.2(9)^i$	$-1646.66(16)^j$	$488.15(6)^j$
	B (MHz)	^{h}	$-462(21)^i$	—	$260.48(25)^j$
$Rg^+\,{}^2P_{1/2}$	A (MHz)	^{k}	$-1154(15)^l$	$-12\,205(27)^m$	$3615(9)^m$

[a] From Grosof *et al* [368].

[b] From Faust and Chow Chiu [369].

[c] From Faust and McDermott [370].

[d] From Delsart and Keller [371]; Ducas *et al* give $A = -452(7)$ MHz, $B = +44$ MHz [372]. Theoretical values: $A = -444$ MHz, $B = +44$ MHz [373]; $A = -460$ MHz [374].

[e] From Jackson [375].

[f] From D'Amico *et al* [376].

[g] Experimental value cited in [374]. Theoretical values: $A = -663$ MHz, $B = -100$ MHz [373]; $A = -659$ MHz [374].

[h] *Ab initio* values: $A = -280.5$ MHz, $B = 106$ MHz [377]. Values may be estimated from the hyperfine structure of the 3s states [341, 342]: $A(^2P_{3/2}) \approx 2[A(1s_2) + A(1s_4) - A(1s_5)]/[1 + A(^2P_{1/2})/A(^2P_{3/2})] \approx [A(1s_2) + A(1s_4) - A(1s_5)]/3 \approx -283$ MHz; $B(^2P_{3/2}) \approx B(1s_5) \approx -112$ MHz.

[i] From Schäfer and Merkt [236].

[j] From Schäfer *et al* [237].

[k] For a "p hole", $A(^2P_{1/2})/A(^2P_{3/2}) \approx 5F_r(\frac{1}{2}, Z_i)/F_r(\frac{3}{2}, Z_i) \approx 5 \cdot 1.005$ [341, 342] where $F_r(j, Z_i)$ are relativistic corrections and the effective atomic number $Z_i \approx Z - 2 = 8$ for a 2p electron [378].

[l] From Paul *et al* [22].

[m] From Wörner *et al* [21].

Photoionization dynamics of excited Ne, Ar, Kr, and Xe atoms near threshold

V L Sukhorukov *et al.*

Figures 1-39

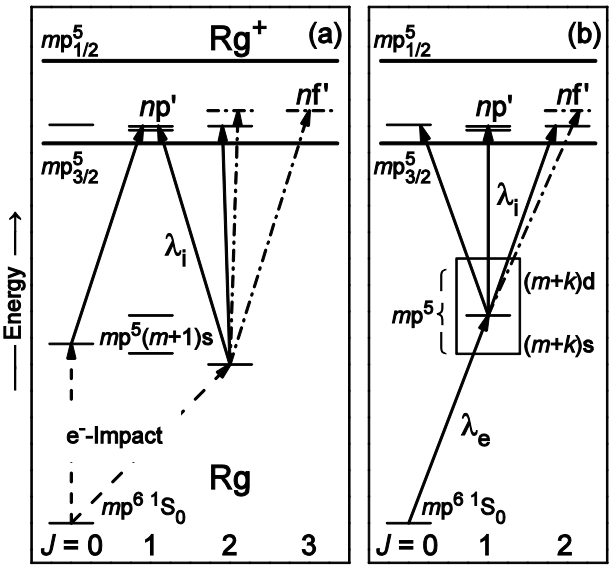

Figure 1.

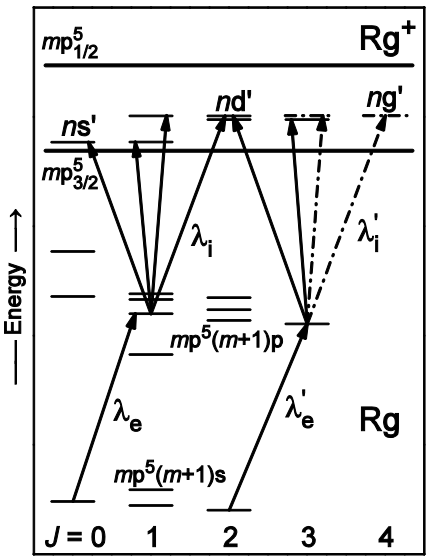

Figure 2.

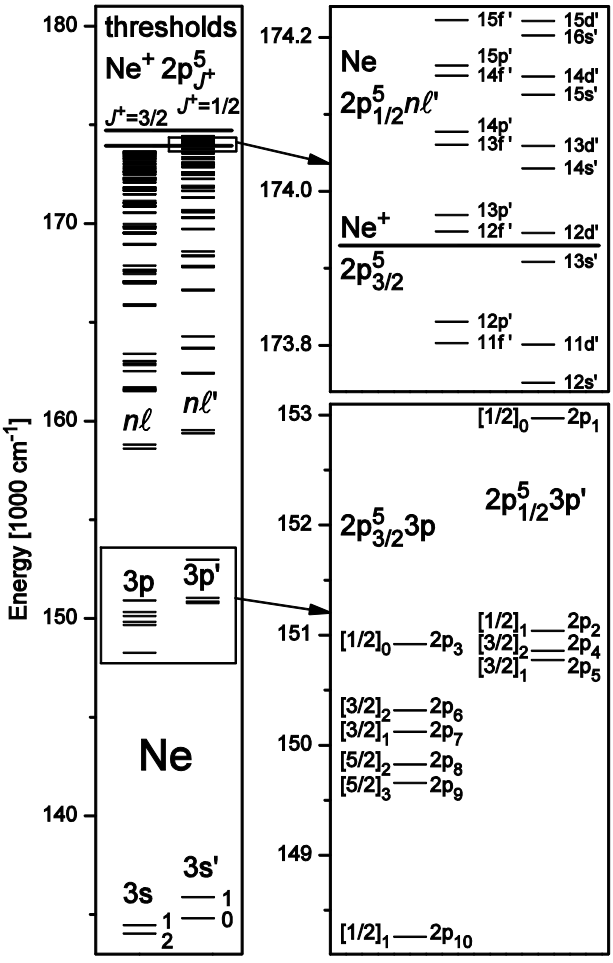

Figure 3.

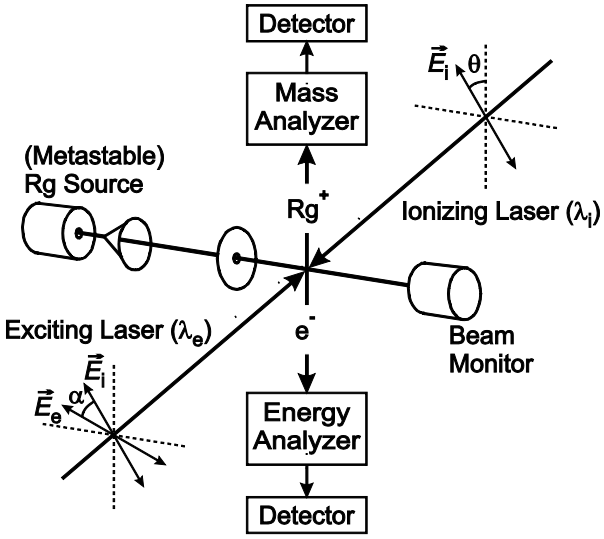

Figure 4.

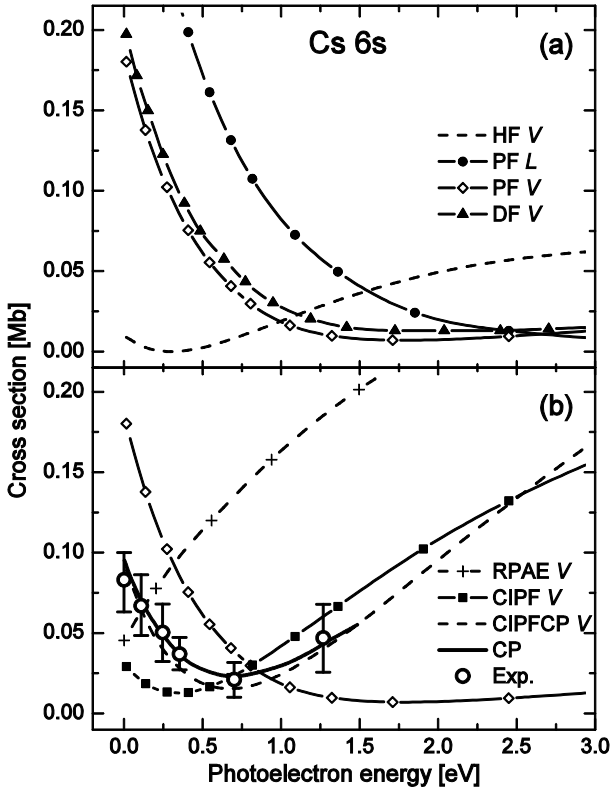

Figure 5.

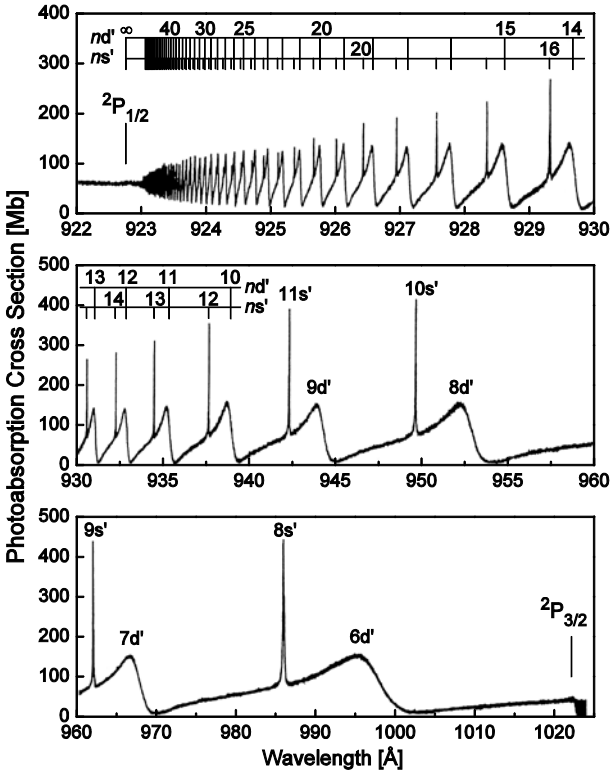

Figure 6.

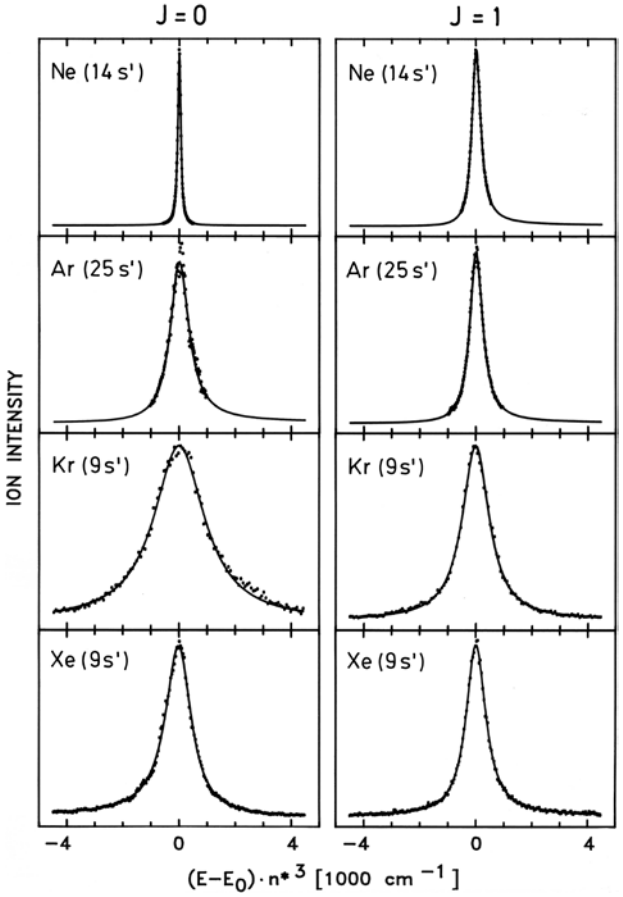

Figure 7.

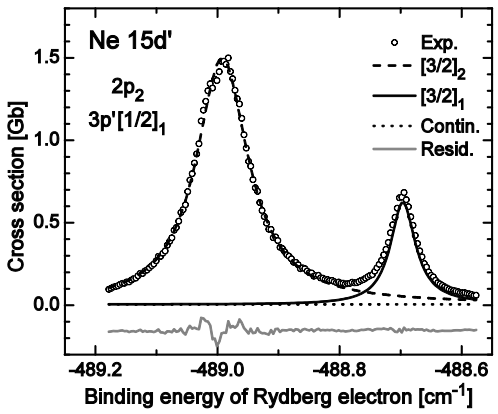

Figure 8.

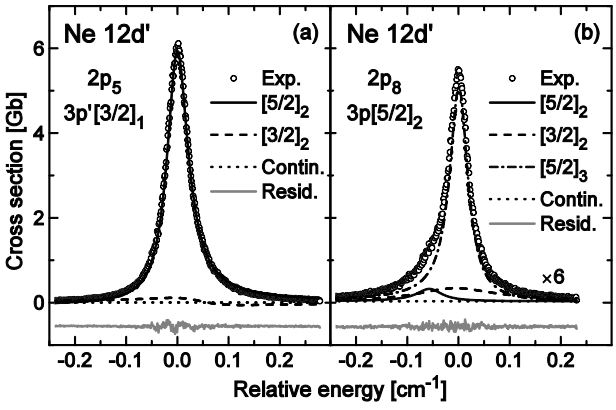

Figure 9.

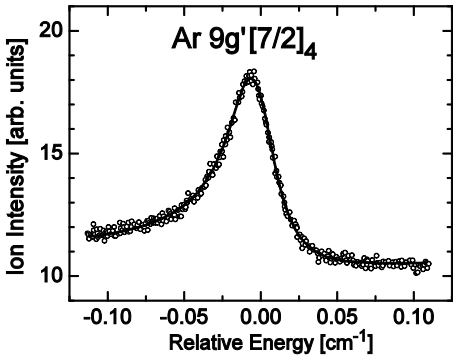

Figure 10.

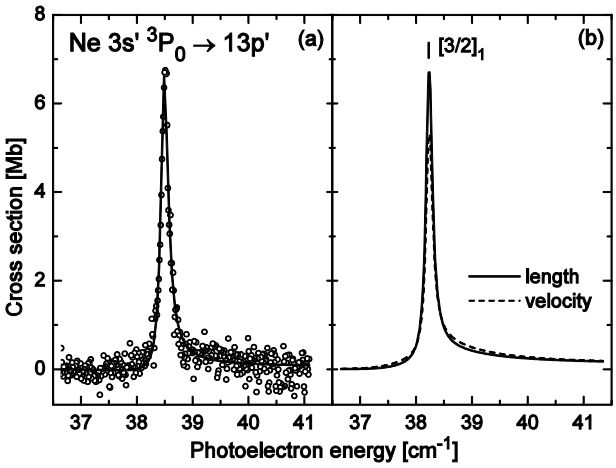

Figure 11.

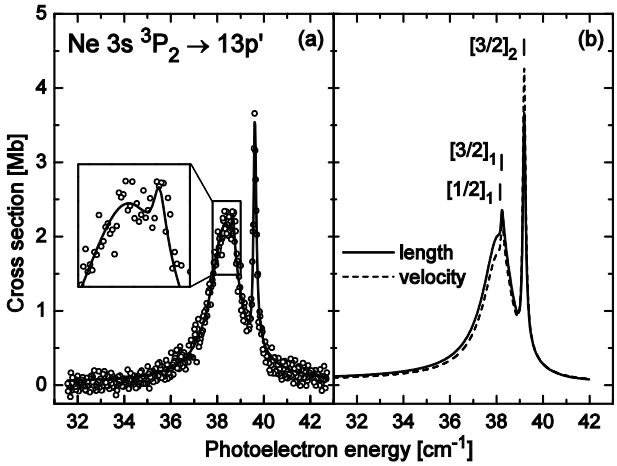

Figure 12.

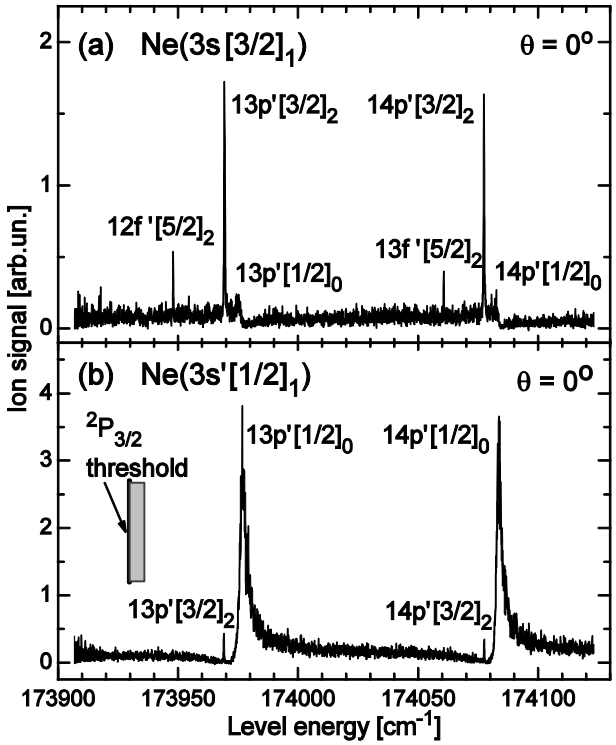

Figure 13.

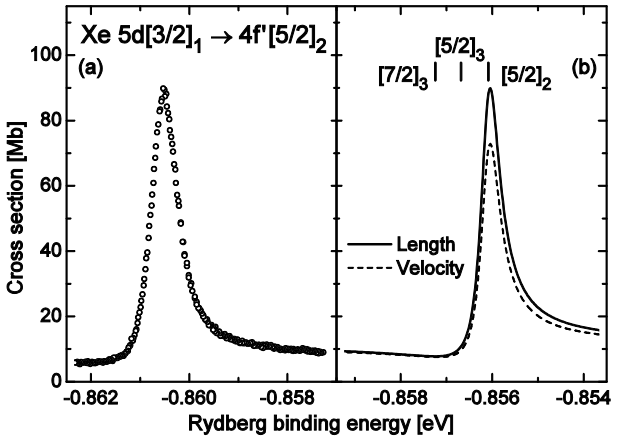

Figure 14.

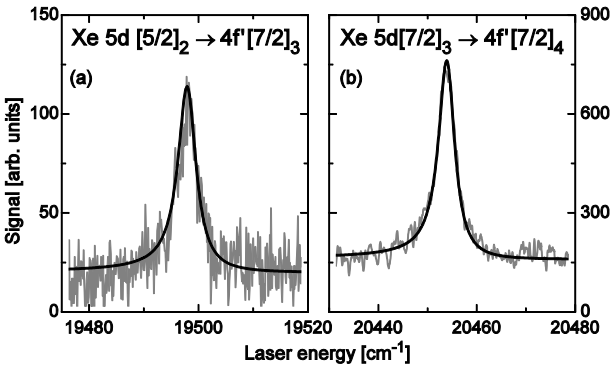

Figure 15.

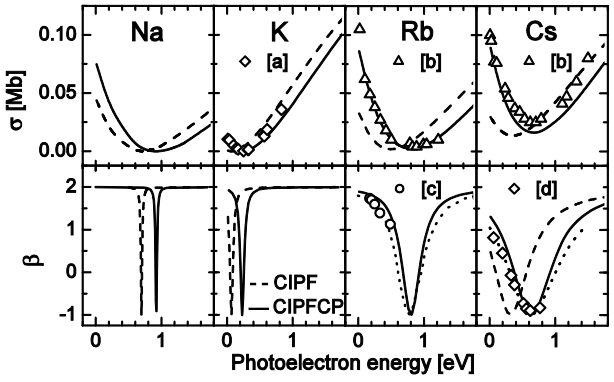

Figure 16.

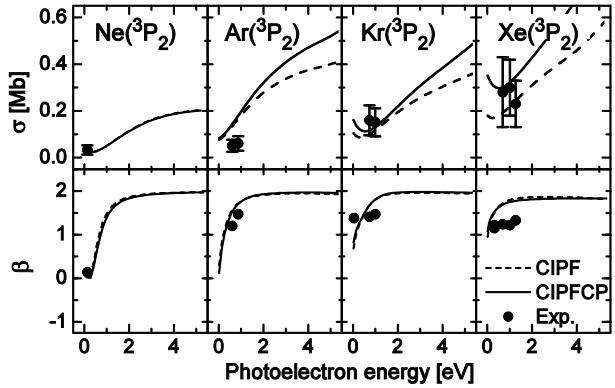

Figure 17.

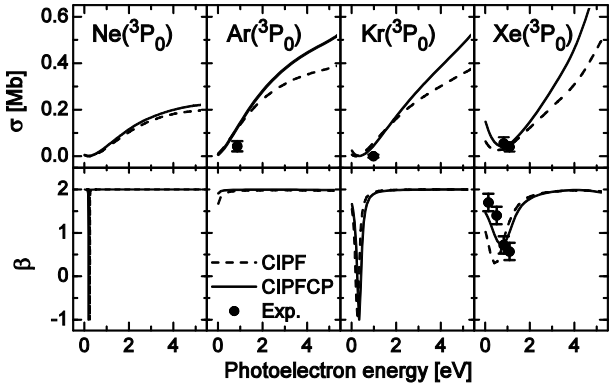

Figure 18.

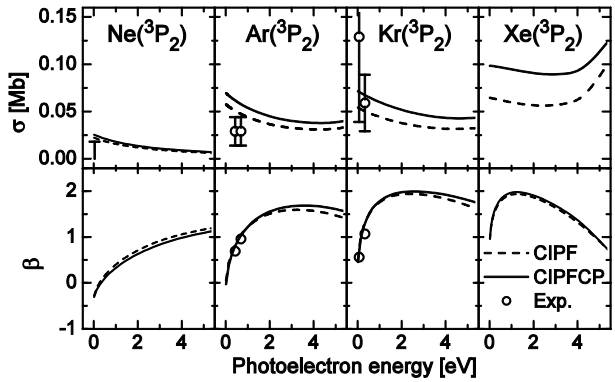

Figure 19.

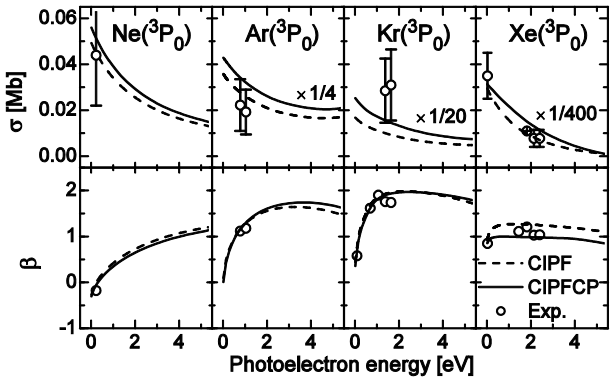

Figure 20.

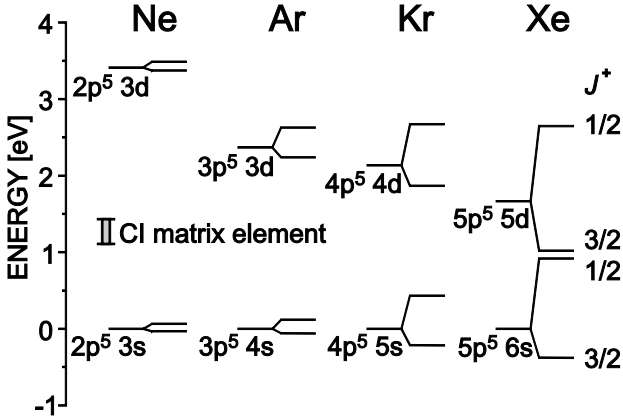

Figure 21.

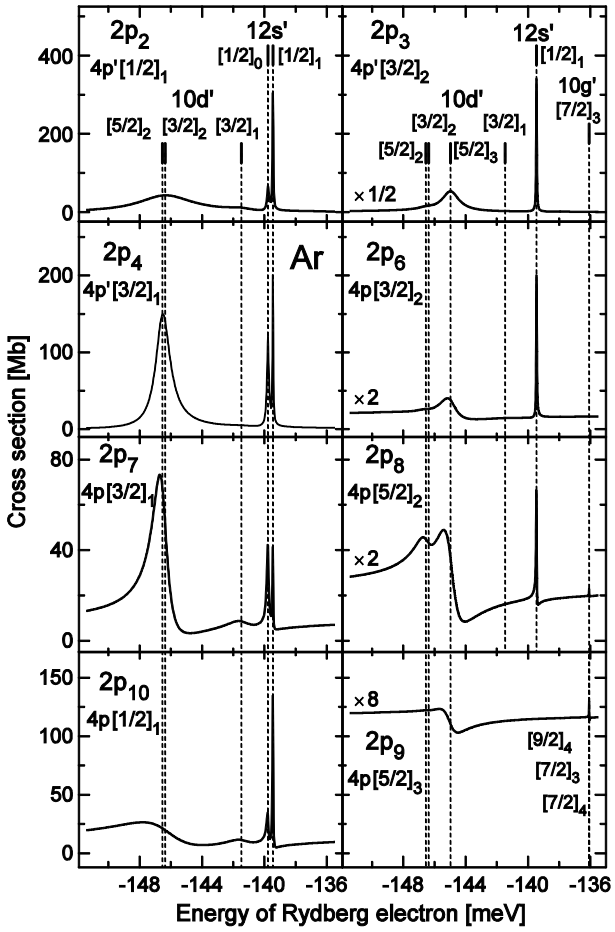

Figure 22.

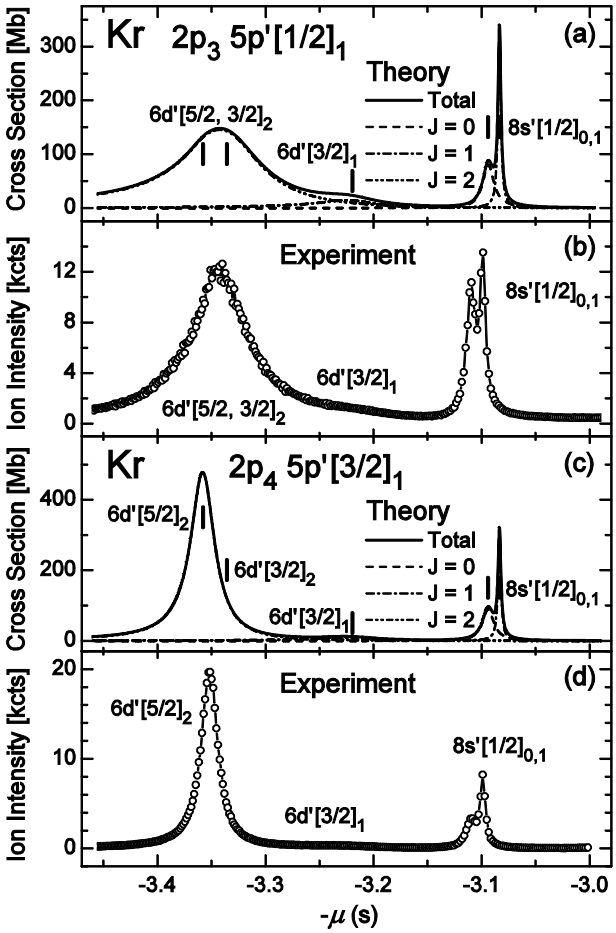

Figure 24.

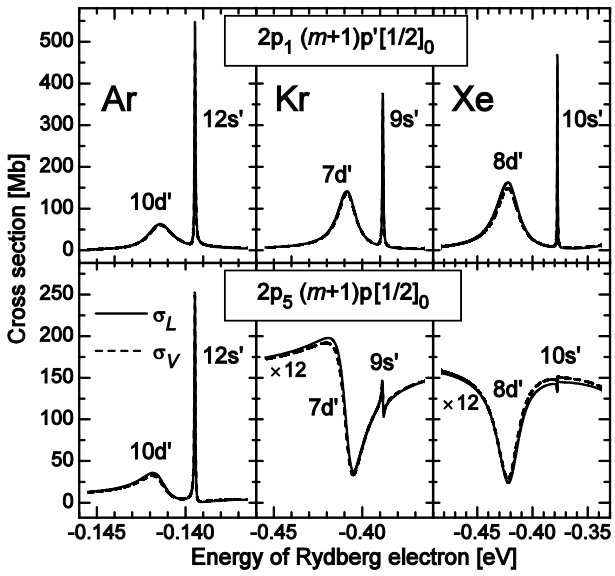

Figure 23.

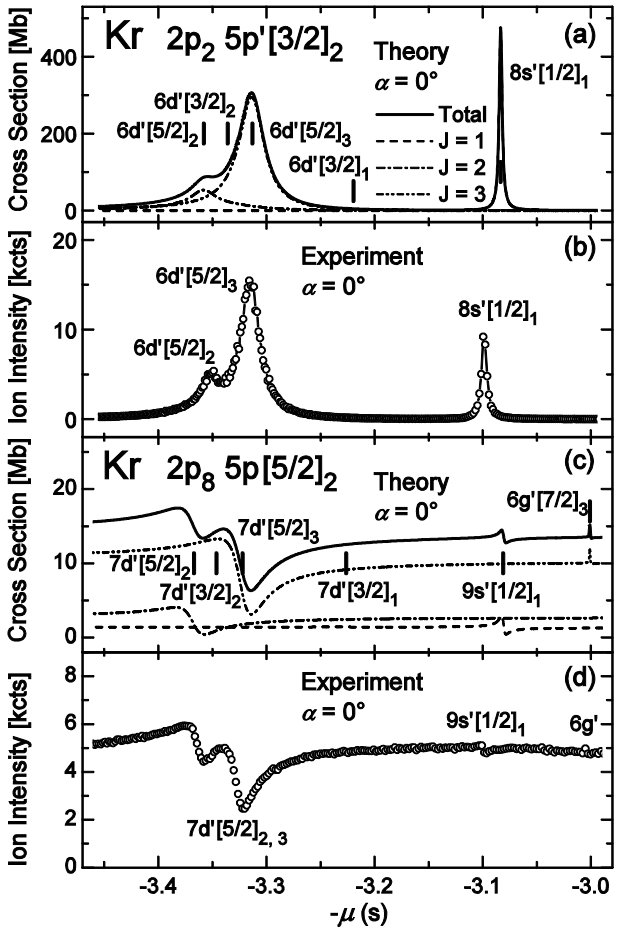

Figure 25.

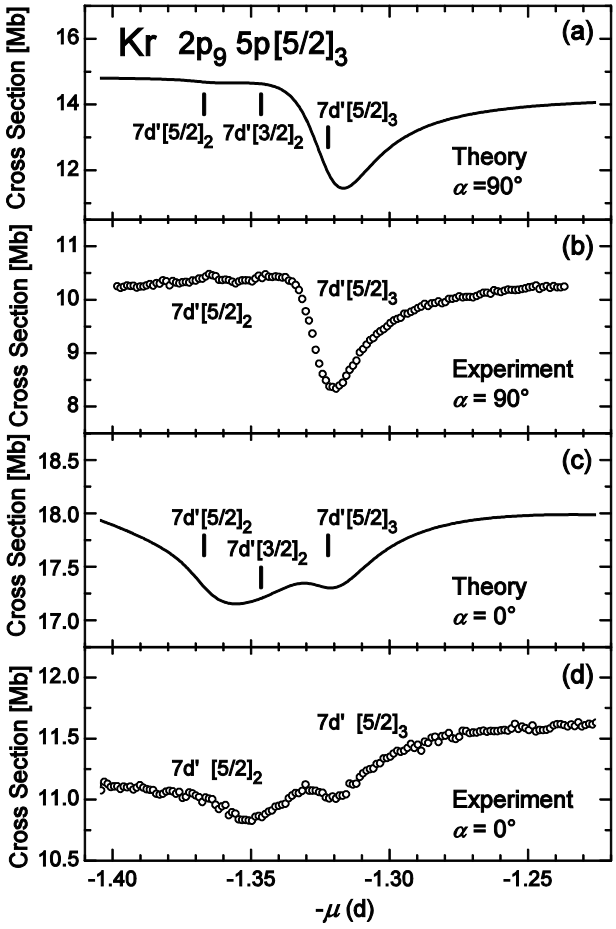

Figure 26.

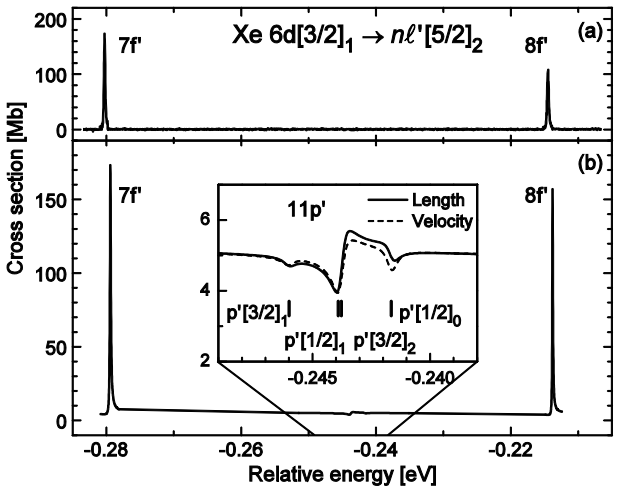

Figure 27.

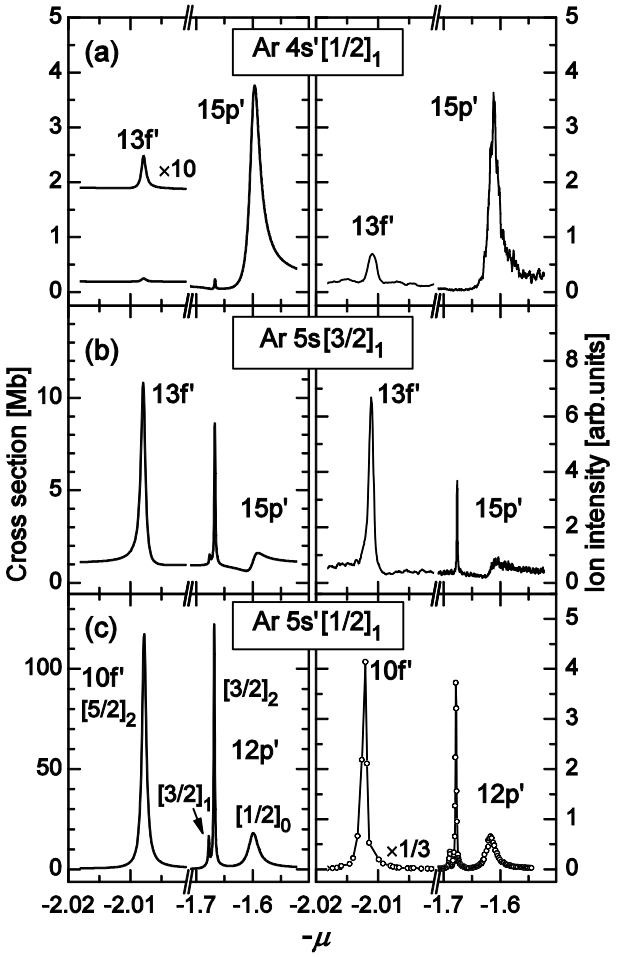

Figure 28.

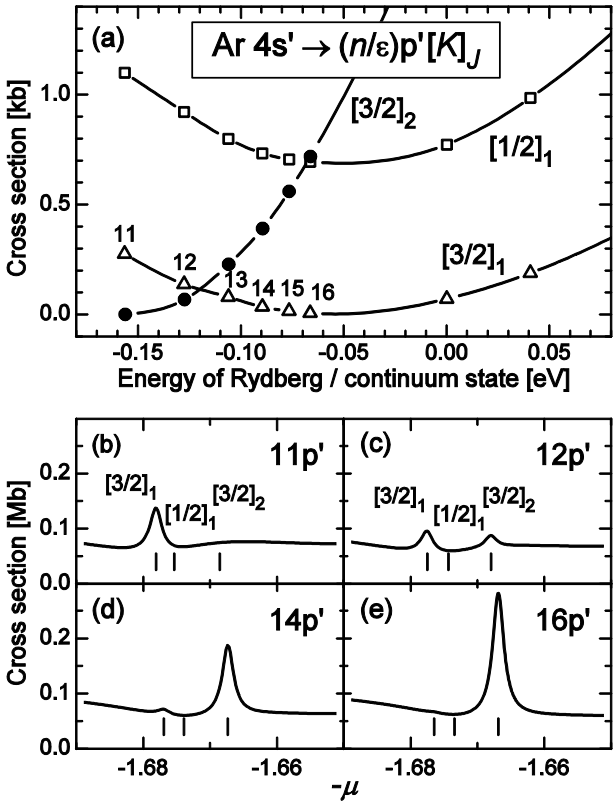

Figure 29.

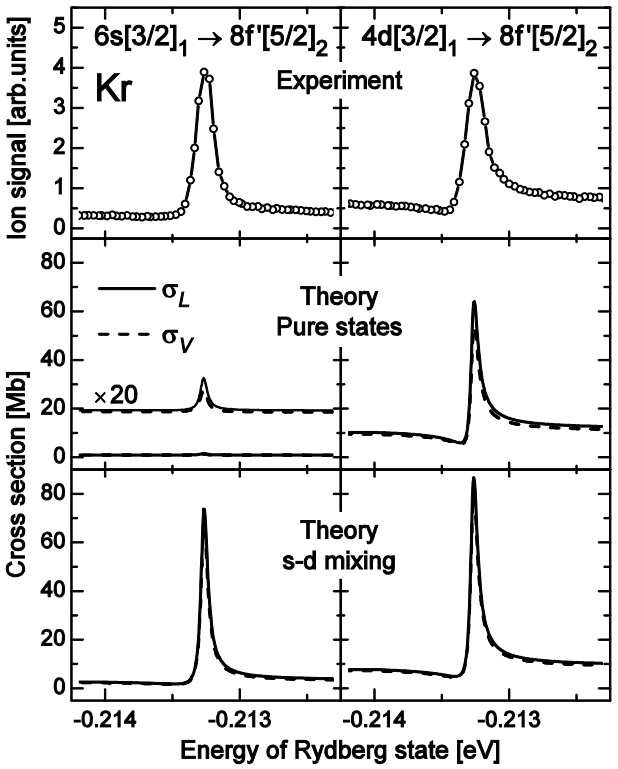

Figure 30.

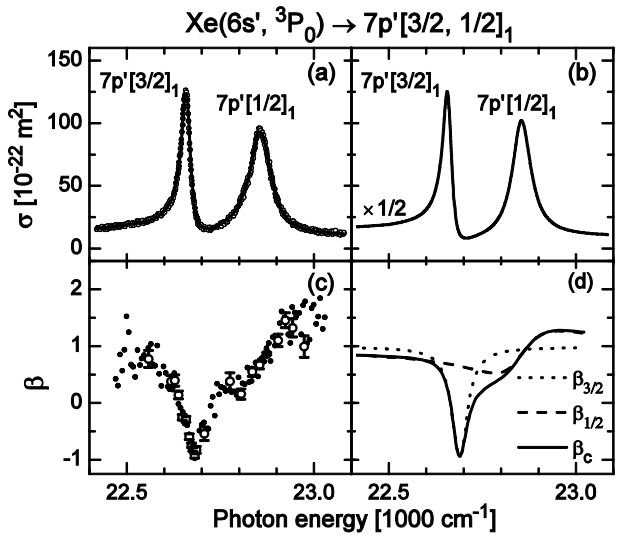

Figure 31.

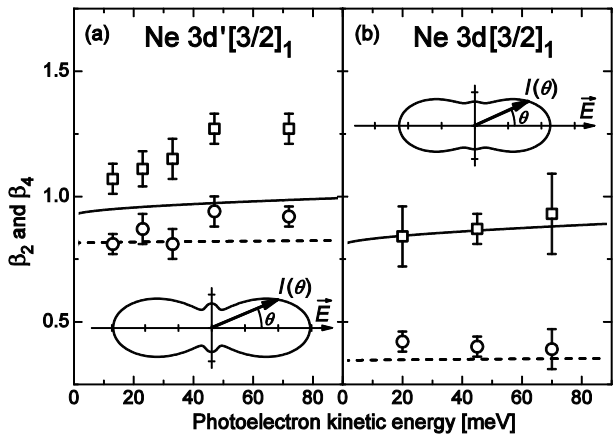

Figure 32.

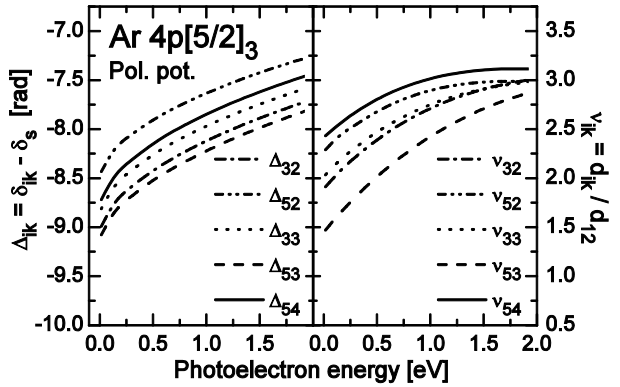

Figure 33.

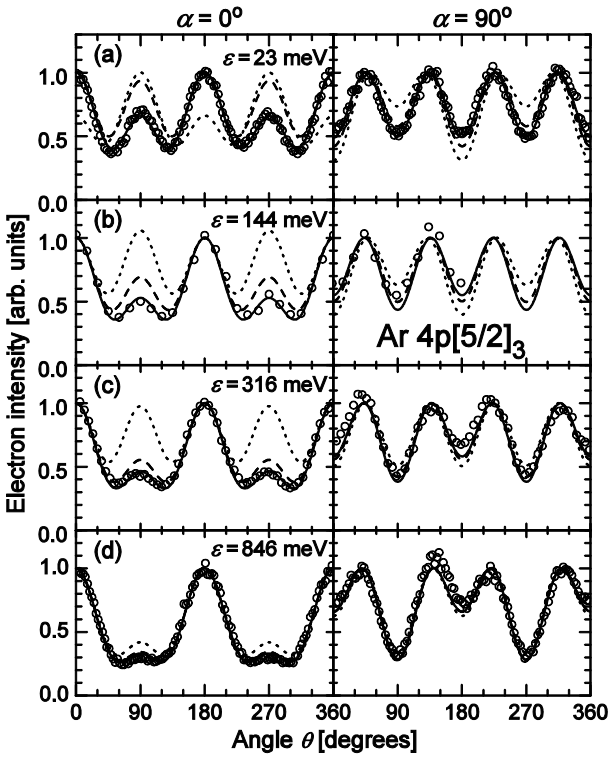

Figure 34.

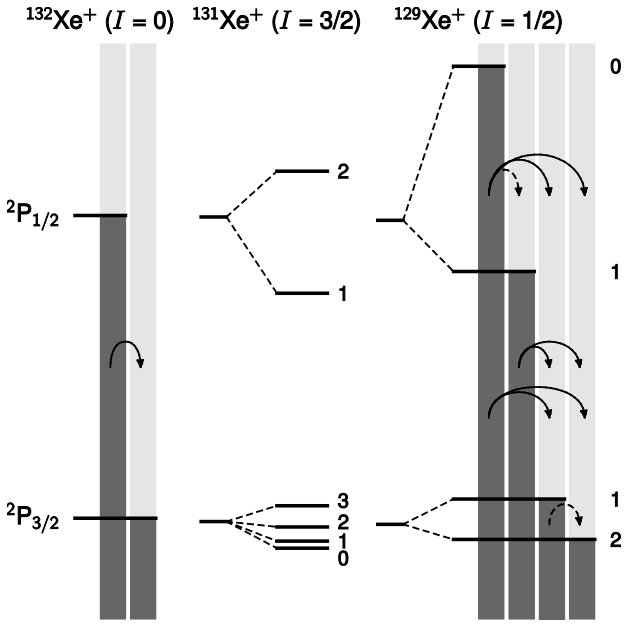

Figure 35.

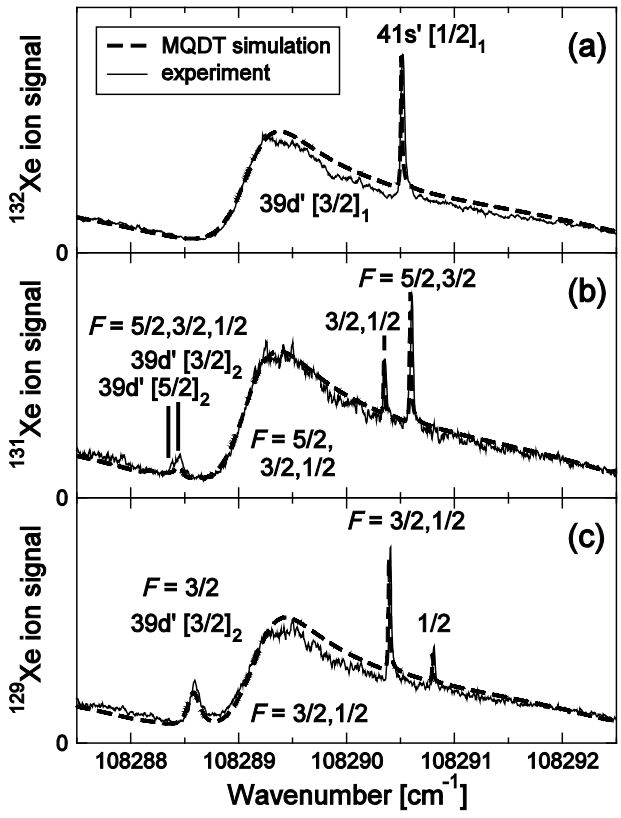

Figure 36.

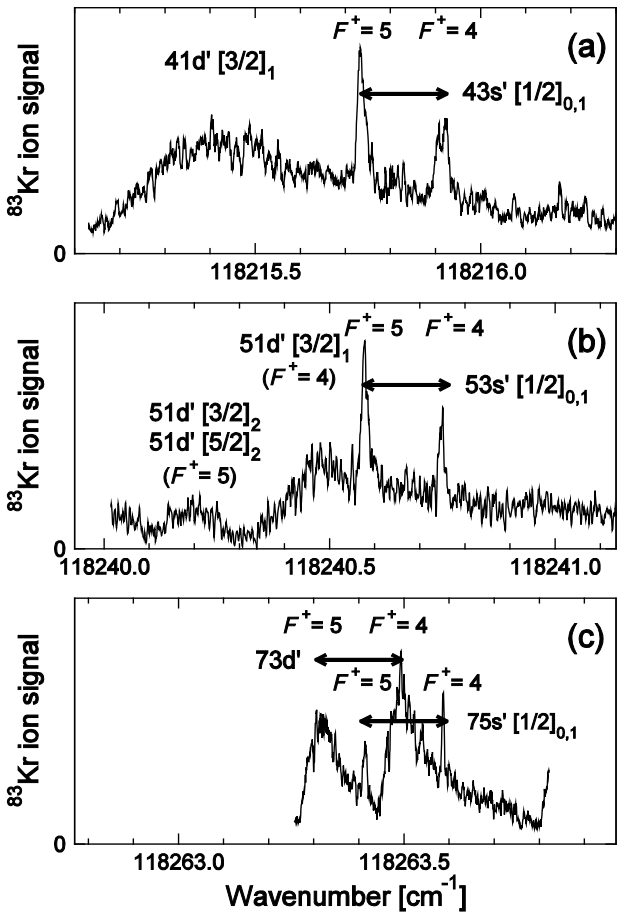

Figure 37.

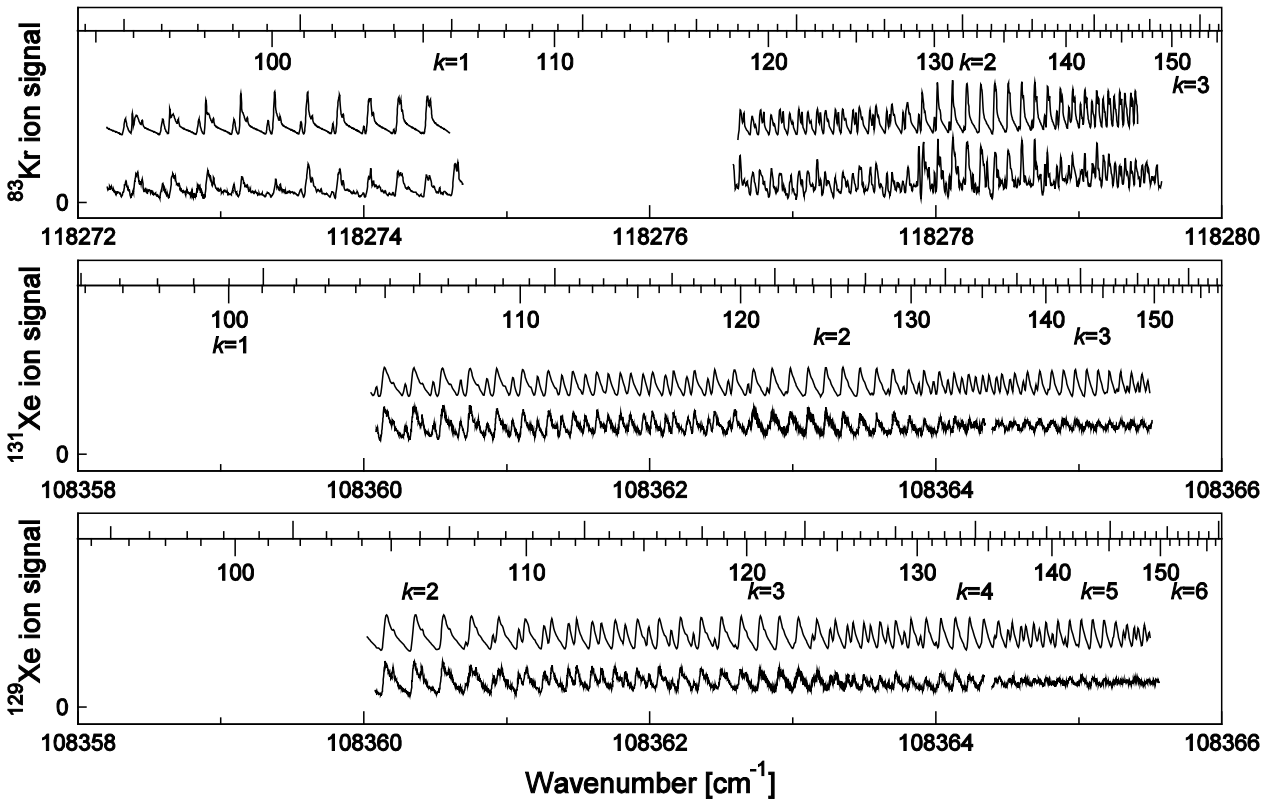

Figure 38.

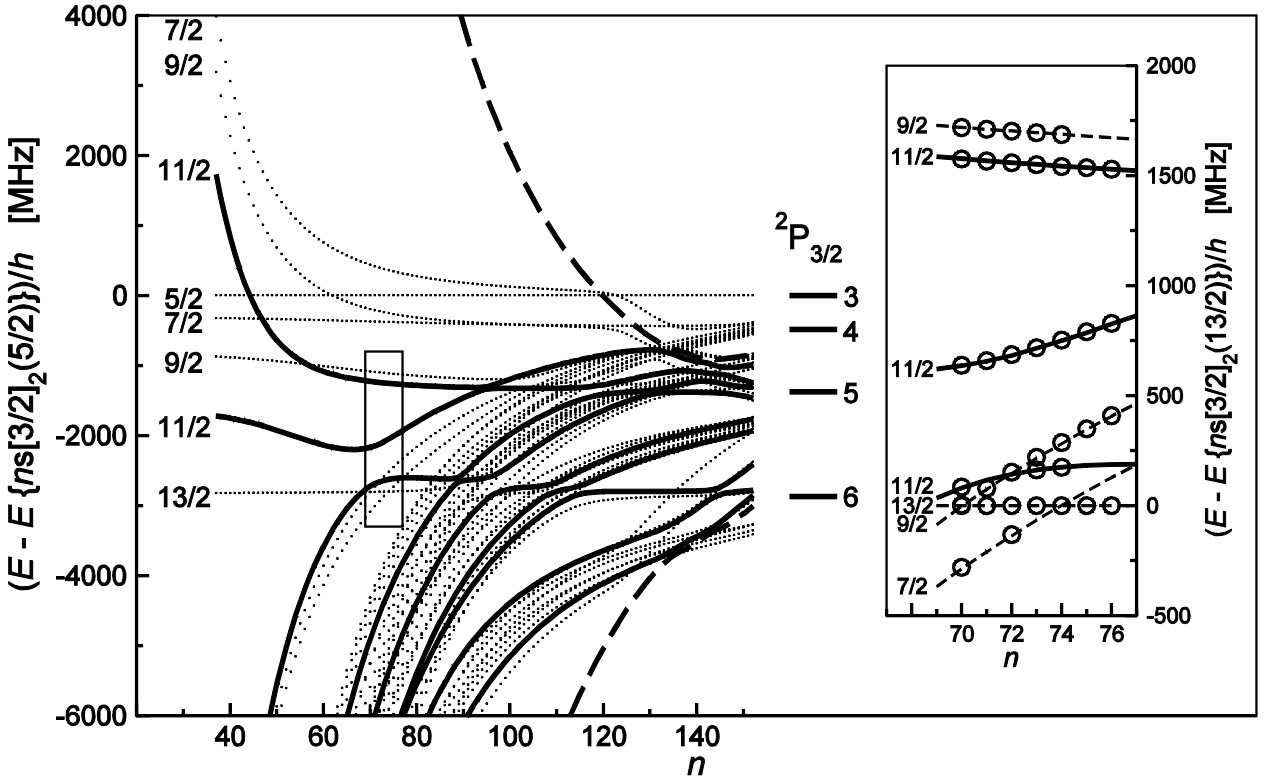

Figure 39.